


Summer 7-25-2017

EVALUATION AND ENHANCEMENT OF CLEAN ENERGY SYSTEMS: ANALYTICAL, COMPUTATIONAL AND EXPERIMENTAL STUDY OF SOLAR AND NUCLEAR CYCLES

NIMA FATHI

Follow this and additional works at: https://digitalrepository.unm.edu/me_etds

 Part of the [Computational Engineering Commons](#), [Energy Systems Commons](#), [Fluid Dynamics Commons](#), [Heat Transfer, Combustion Commons](#), [Nuclear Engineering Commons](#), and the [Numerical Analysis and Computation Commons](#)

Recommended Citation

FATHI, NIMA. "EVALUATION AND ENHANCEMENT OF CLEAN ENERGY SYSTEMS: ANALYTICAL, COMPUTATIONAL AND EXPERIMENTAL STUDY OF SOLAR AND NUCLEAR CYCLES." (2017).
https://digitalrepository.unm.edu/me_etds/137

This Dissertation is brought to you for free and open access by the Engineering ETDs at UNM Digital Repository. It has been accepted for inclusion in Mechanical Engineering ETDs by an authorized administrator of UNM Digital Repository. For more information, please contact disc@unm.edu.

Nima Fathi

Candidate

Mechanical Engineering

Department

This thesis is approved, and it is acceptable in quality and form for publication:

Approved by the Thesis Committee:

Dr. Peter Vorobieff

, Chairperson

Dr. Patrick McDaniel

Dr. C. Randall Truman

Dr. Jens Lorenz

**EVALUATION AND ENHANCEMENT OF
CLEAN ENERGY SYSTEMS:
ANALYTICAL, COMPUTATIONAL AND
EXPERIMENTAL STUDY OF
SOLAR AND NUCLEAR CYCLES**

by

NIMA FATHI

M.S., Mechanical Engineering, University of New Mexico, 2012
M.S., Nuclear Engineering, Univerisyt of New Mexico, 2016

DISSERTATION

Submitted in Partial Fulfillment of the
Requirements for the Degree of

**Doctor of Philosophy
Engineering**

The University of New Mexico
Albuquerque, New Mexico

July 2017

*To my parents, Roya and Hassan, and my grandparents,
Nasrin and Siavash, whom I miss them all!*

*To my spiritual father, Master Hossein Ghanbari
Ghaem (piremehr).*

*Also, I would like to dedicate this work to Master
Rahmani.*

EVALUATION AND ENHANCEMENT OF
CLEAN ENERGY SYSTEMS:
ANALYTICAL, COMPUTATIONAL AND EXPERIMENTAL STUDY OF
SOLAR AND NUCLEAR CYCLES

by

Nima Fathi

M.S., Mechanical Engineering, University of New Mexico, 2012

M.S., Nuclear Engineering, Univerisyt of New Mexico, 2016

Ph.D., Mechanical Engineering, University of New Mexico, 2017

ABSTRACT

Clean (and specifically renewable) energy is steadily improving its global share. However, finite availability of fossil fuels and the growing effects of climate change make it an urgent priority to convince the industry and governments to incentivize investment in the renewable energy field and to make it more attractive by decreasing the capital cost. Until recently, uncertainties in funding limited renewable energy development, especially in the US. That limitation has been one of the barriers to progress. Another limitation of many renewable energy systems is the variability in their output, which makes them unsuitable for baseline power production. Therefore, fossil fuels are still the dominant source of energy globally. The estimated US energy consumption in 2015 relied heavily on fossil fuels which generated about 82% of US primary energy. The share of solar energy in 2015 US energy consumption was just 0.43%. This is a disappointingly small share for a zero carbon source of energy. Nuclear energy as another clean energy source has a small share as 8% of the total US energy consumption. Although it is one of the most reliable/stable and low carbon sources of energy, the nuclear power industry is currently facing several challenges. First, nuclear generated electricity is not cost-competitive with other types of generation. Second, there is a diminished availability of cooling water to reject heat from large power plants. Third, the penetration of solar and wind generation systems into the electrical power market is producing significant fluctuations in the demand for nuclear generation. Open Air-Brayton systems are one of the solutions here since the ultimate heat sink for

nuclear supplied power is the atmosphere, so a more direct method of dumping this heat would be useful. An open Air-Brayton system can also provide a great deal of flexibility in adjusting power plant electrical output without significantly ramping reactor power output. This dissertation develops a common framework for understating and improving the solar and nuclear clean energy system components which are based on Brayton cycles. For this purpose, experimental and numerical studies of solar and nuclear systems are conducted.

The open air Brayton cycle of a solar chimney power plant is studied in this investigation in different cases as a solar power cycle. Additionally, the air Brayton cycle of a nuclear power plant is considered for several different cases, including a combined nuclear-solar cycle. Air flow is driven by buoyancy in the open air Brayton cycle of a solar chimney power plant system (SCCPS). In SCPPS, the energy of buoyant hot air is converted to electrical energy. SCPPS includes a collector at ground level, covered with a transparent roof that collects the solar radiation, which heats the air inside and the ground underneath. This dissertation proposes and studies new modifications and optimizations to increase the thermal efficiency of the SCCPS, as well as combining SCCPS cycles with other clean sustainable cycles. The nuclear-combined air Brayton cycles are studied with the focus on producing low-carbon energy and combining pressurized water reactor and small modular reactor cycles with another thermal cycle, leading to increased combined efficiency.

In this manuscript, chapters are organized with respect to the type of their thermal cycle. Part I, includes three chapters focusing on simple/single Brayton cycle. Part II contains two chapters regarding combined Brayton cycles. Each chapter in this investigation is based on at least one published or accepted/ready to publish article, and which have undergone peer review. The citation for each original source manuscript is included as a footnote on the bottom of the first page of each chapter. Therefore, each chapter is in the format of a journal article, including: an introduction, motivation and background, theory, numerical approach, experimental approach, results and dissections, future work and conclusion. The references and acknowledgments associated with each article are provided at the end of each chapter. All achievements of this work are listed in Appendix A.

Part I, chapter one describes non-deterministic computational fluid dynamics (CFD) and conjugate heat transfer (CHT) study of a solar chimney power plant. The

initial CFD analyses were validated against the data from the only available large-scale prototype (Manzanares solar tower). To evaluate our CFD analysis beside code verification, an analytical model was developed based on Navier-Stokes equations coupled with the equation of state and using the Boussinesq approximation. The second chapter of this research focuses on evaluating the patented idea of having a double-inlet collector in SCPPS. In this chapter, efforts are made to achieve quantitative accuracy assessment of the modeling and simulation of SCPPS for a conventional collector. The experimental exploration is based on particle image velocimetry (PIV) to provide experimental values for our finite volume based CFD/CHT results. The results of verification and validation of the CFD/CHT analysis are reported. The third chapter of this research addresses the second patented idea regarding applying inflatable towers on solar collectors. Mathematical and computational analyses were conducted. Also, an experimental apparatus was designed and fabricated in 2014 at the University of New Mexico for different testing and evaluation approaches. The results of this validation and the prototype are available in Appendix B.

As mentioned before, Part II focuses on combined air Brayton cycles. Chapter 4 reports the study and modeling of our third patented idea, applying surplus heat from a nuclear power plant to the SCPPS. In the proposed combined cycle, we replaced the power plant cooling tower with SCPPS. Therefore, SCCPS serves the function of a dry cooling tower, and also produces additional electrical power in this novel combined nuclear-solar cycle. By applying this idea, it is possible to increase the thermal efficiency of a typical 1000 MW nuclear power plant (35.5%) to 41.4%. The last chapter is focused on a combined nuclear air Brayton cycle to increase the output power of a 50 MW small modular liquid metal/molten salt reactor. Since the major cost of nuclear electricity is the capital cost of plant construction, the concept of small modular reactors has won favor as a method of improving cash flow and minimizing the time required to bring new generation on line, reducing interest expenses. Considerable power increases are predicted for nuclear air-Brayton systems by Co-Firing with hydrogen before the power turbine.

Acknowledgements

First and foremost, I am deeply grateful to Professor Peter Vorobieff, my advisor, mentor, and also my true friend and brother. Without his great and unique support, time, pieces of advice and infinite patience this work would not have been possible. I will never forget his key role in my life.

I would also like to offer my special thanks to Professor Patrick McDaniel, my mentor, and role model. He always offered generously his time, support and advice. I truly feel honored to be his student in my academic life.

I wish to express my warm and sincere appreciation to Professor Randy Truman and Professor Jens Lorenz, committee members, for their support, advice, and patience in these years.

Finally, I am indebted to colleagues, staff members, and fellow students, too numerous to mention, who made suggestions and gave much encouragement.

Contents

Abstract	ii
Acknowledgements	v
List of Figures	ix
List of Tables	xii
I Simple Power Cycles	1
1 Numerical-Analytical Analysis on Manzanares Solar Power Plant Prototype	2
1.1 Introduction	5
1.2 Analytical Study	7
1.2.1 Collector	7
1.2.2 Tower	11
1.2.3 Turbine	14
1.3 Numerical Analysis	16
1.4 Results and Discussion	17
1.5 Conclusion	22
2 Experimental-Computational Analysis of Multi-inlet and Conventional Collectors	29
2.1 Introduction	32
2.2 Conceptual Design	35
2.3 Modeling and Simulation Approach	35
2.4 Analytical Approach	37
2.4.1 Collector	38
2.4.2 Experimental Prodecure	42
2.5 Results and Discussion	43
2.6 Conclusion	53
3 Inflatable Free-Standing Solar Chimney Power Plants	59

3.1	Introduction	61
3.2	Conceptual design and theoretical considerations	64
3.3	Optimization strategy: prescribed deformation design	69
3.3.1	Formal problem set-up	69
	The force between two tori	70
	Equilibrium conditions	72
3.3.2	Analytic solution for tower shape	76
	Optimization procedure I	81
	Optimization procedure II	82
3.3.3	Control of tower deformation using adjustable air pressure	84
3.3.4	Deformations of bladders due to the supporting weight	86
3.4	Savings and other considerations	88
3.5	Modeling of the updraft flow	91
3.6	Conclusions	103

II Combined Power Cycles 110

4 Efficiency Enhancement of Solar Chimney Power Plant System by Use of Waste Heat from Nuclear Power Plant 111

4.1	Introduction	115
4.1.1	Motivation and Background	115
4.1.2	Previous Work	119
4.1.3	Utilization by Grid	122
4.2	Modeling and Simulation	124
4.2.1	CFD analysis	124
4.2.2	Thermal analysis	129
4.3	Results and Discussion	130
4.3.1	CFD/Thermal Results	130
4.3.2	Economic Considerations	137
4.3.3	Future Work	138
4.4	Conclusion	139
4.5	Acknowledgment	141

5 Power Cycle Assessment of Combined Clean Energy Systems 149

5.1	Introduction	151
5.1.1	Motivation and Background	151
5.1.2	Technical Approach	152
5.1.3	Modeling Approach	157
5.2	NACC Scenarios Analyzed	158
5.3	NACC with only Co-Firing	160
5.4	NACC with Co-Firing and Increased Steam Flow	161
5.5	NACCRIC with Co-Firing - Maximum Recuperator Temperature Limit	163
5.6	Limiting the Co-Firing temperature	165

5.7	NACCRIC with Co-Firing - Increased Steam Flow to Meet Recuperator Temperature Limit	168
5.8	NARC Scenarios Analyzed	171
5.9	Conclusion	176
5.10	Acknowledgment	177
A	List of Achievements of this Research	181
A.1	Publications	181
A.2	Patents	182
A.3	Presentations	183
B	Experimental Analysis of Inflatable Tower	184

List of Figures

1.1	Schematic of SCPPS with the applied variables and subscripts in the present analysis	6
1.2	Manzanares prototype turbine [4].	14
1.3	Computational domain and applied boundary conditions.	17
1.4	Analytical power results against measurement from Manzanares: updraft velocity and power output for a typical day.	19
1.5	Analytical power results against mass flow rate for a range of solar irradiation.	20
1.6	Analytical power results against mass flow rate for different values of collector efficiency.	21
1.7	Velocity contour plot (m/s) for different available solar heat flux at the ground of collector, (a):200, (b):400, (c):600, (d):800, (e)1000 W/m^2	23
1.8	Power vs solar irradiation.	24
2.1	Schematic of a solar chimney power plant	33
2.2	Schematic case description, traditional collector (Case A), double-inlet collector (Case B)	36
2.3	Case B model details	38
2.4	Computational domain of case B with the applied boundary conditions	39
2.5	PIV SCPPS apparatus	43
2.6	Collector and hot plate arrangement, two types of used collector in the experimental analysis	44
2.7	Location of probes for post processing	45
2.8	Velocity distribution along the collector for different heat flux values	46
2.9	Velocity profile at 20 m of tower	47
2.10	Density distribution along the collector	48
2.11	Pressure evolution along the collector	49
2.12	Temperature distribution along the collector	50
2.13	Velocity distribution at the turbine location	51
2.14	Output power for different cases	52
2.15	Experimental region of interest, blue Square (a) and averaged velocity vector/contour plot of the area of interest (b)	53
2.16	Cumulative probability of D and S, area metric validation representation	54

3.1	Schematic of a solar updraft tower facility with a chimney comprised of toroidal bladders.	67
3.2	Tori $k - 1$, k and $k + 1$ in contact. Top left: front (windward) view. The toroidal cross-section (area A_k) exposed to the wind is a combination of a rectangle and two half-circles. Bottom left: top view. The contact area S_k between two tori caused by the wind deformation is shown. Right: side view.	72
3.3	An illustration of torque balance on the flexible tower.	74
3.4	Left: solar tower computed from Eq. (3.17) with $V = 2000$. The radius of the bottom torus is roughly 200 m, top torus 10.5 m, the tower height is 800 m and the inner diameter of each torus is 10 m (leading to a rather severe constriction on top). Right: the same solar tower with the relative maximum deformation δR_k for each torus being 1% of the smaller radius $R_k = R$. Since the radius q_k of the tower is smaller at top, and $R_k = R = \text{const}$, the tilt ($\arctan(h_k/q_k)$) is correspondingly larger for the top tori.	82
3.5	Left: solar tower computed from Eq. (3.18) and (3.19) with $V = 2000$. The ratio of smaller to larger radii of all tori is assumed to be 0.1. The radius of the top torus is 50 m, the radius of the bottom torus is 88.4 m. Right: the same solar tower with the relative tilt for each torus being 1%	84
3.6	Computational domain, boundary conditions, and closeups of the grid for numerical modeling (proportional tower shape). For clarity, the most sparse grid is shown (50,000 nodes). The actual calculations used a finer grid with about 10 times more elements.	94
3.7	Results of numerical simulation of the air flow in solar updraft towers of different shapes (top row – velocity, bottom row – temperature, no ΔP_T pressure drop). Left –proportional shape with decreasing inner cross-section computed using Eqs. 3.18,3.19 with $V = 2000$. Center – fixed-height shape computed using Eq. 3.17 with same V value. Right – reference straight tower with the same vertical cross-sectional area as the proportional tower. The vertical extent of the images is 1 km.	95
3.8	Velocity maps for the flow with no inlet-to-outlet pressure drop.	102
4.1	Estimated US energy flows in 2015. Values are in quadrillion British units. Total energy input is 98.3 Quads.	117
4.2	Schematic of an SCPPS (left), Manzanares prototype (right).	118
4.3	Schematic diagram of a pressurized water reactor and the steam turbine that convert work into electrical energy with a cooling tower.	124
4.4	Block diagram of an open air-Brayton cycle of SCCPS (instead of cooling tower) combined with a pressurized water reactor.	125
4.5	Example process of producing a schedule given base load generators, solar chimney, and other distributed energy resources (DERs; such as photovoltaic arrays, wind farms, etc.).	126

4.6	Experimental and numerical comparative representation of the output turbine power of Manzanares prototype vs a range of available heat flux and the effect of applying heat waste to the solar cycle . . .	132
4.7	Thermal Power Plant efficiencies vs. Ambient Temperature.	134
4.8	Increase in efficiency vs. the output power of SCPPS.	136
4.9	MATLAB thermal simulation block diagram for steam power plant cycle. 1-5 are thermal probes to read the thermal properties. . . .	140
5.1	System description	152
5.2	Schematic presentation complete nuclear Air-Brayton combined cycle with recuperator and intercooler	154
5.3	Cycle Efficiencies for NACC, SCO ₂ , NACC&RIC and NARC	155
5.4	Compressor Pressure Ratios	157
5.5	Power increase due to Co-Firing at normal steam flow rates	161
5.6	Increase in steam flow to maintain pinch point for the NACC system	162
5.7	Power increase for NACC if the pinch point temperature difference is held constant.	163
5.8	Hydrogen burn efficiencies when the pinch point temperature difference is constant.	164
5.9	The maximum Co-Firing temperature allowed to reach the system normal TIT	165
5.10	Power increase allowed by Co-Firing at the maximum allowed temperature	166
5.11	The required fraction of rated power for the reactor when Co-Firing at maximum temperature	167
5.12	Hydrogen burn efficiency at the maximum Co-Firing temperature .	167
5.13	Increase in steam flow for the recuperator outlet temperature limit .	169
5.14	Percent power increase when the steam flow is increased to reach the maximum recuperator outlet temperature.	169
5.15	Required fraction of reactor rated power when Co-Firing with increased steam flow	170
5.16	Hydrogen burn efficiency when steam flow is increased to meet the maximum recuperator outlet temperature.	171
5.17	Comparison of required environmental heat removal by water for NACC&RIC and $NARC_w$ systems	172
5.18	Recommended peak burn temperatures for NARC systems	173
5.19	Hydrogen burn efficiency for NARC systems	173
5.20	Percent power augmentation for NARC systems using Co-Firing . .	174
5.21	Overall system efficiencies for the co-fired systems	175
5.22	Estimated system volumes for NACC and NARC systems	176

List of Tables

3.1	Results of numerical simulations for different tower geometries and different assumptions about turbine placement and corresponding pressure drops. Labels “Fixed” and “Prop.” refer to fixed-height and proportional designs as described in the text. Kinetic energy fluxes $\frac{1}{2}\rho\bar{u}^3 A_c$ are normalized by the value for the straight tower and maximum pressure drop. Turbine output, estimated as $\eta_{tt}\bar{u}A_c\Delta P_T$, is likewise normalized.	97
3.2	Boundary conditions used for modeling the Manzanares power plant.	101
3.3	Average exit velocities for different tower shapes and the cases of 10,000 Pa vs. zero inlet-outlet pressure difference. Pressure drop due to the turbine is not considered here.	102
4.1	Manzanares prototype dimensions.	127
4.2	Applied boundary conditions in CFD analysis	128
4.3	Comparison of nuclear only power plant with combined nuclear and SCPPS	135

Part I

Simple Power Cycles

Chapter 1

Numerical-Analytical Analysis on Manzanares Solar Power Plant Prototype¹

In this study an appropriate expression to estimate the output power of solar chimney power plant systems (SCPPS) was considered. Recently several mathematical models of SCPPS were derived, studied for a variety of boundary conditions, and compared against CFD calculations. An important concern for modeling SCPPS is the accuracy of the derived pressure drop and output power equation. To elucidate the matter, axisymmetric CFD analysis was performed to model the solar chimney power plant and calculate the output power for different available solar radiation.

¹Originally published as: Fathi, Nima, Seyed Sobhan Aleyasin, and Peter Vorobieff. "Numerical-analytical assessment on Manzanares prototype." *Applied Thermal Engineering* 102 (2016): 243-250.

Both analytical and numerical results were compared against the available experimental data from the historical Manzanares power plant. We also evaluated the fidelity of the assumptions underlying the derivation and present the output power characteristics of Manzanares prototype under a range of solar irradiation, mass flow rate and collector efficiency. This research provides an approach to estimate the output power with respect to available radiation to the collector .

Collector Chimney Pressure drop Modeling and simulation Analytical solution
Computational fluid dynamics

Nomenclature

Variables

A	cross-sectional area, m^2
A_r	cross-sectional area of the collector ground, m^2
g	acceleration due to gravity, m/s^2
h	height, m
\dot{m}	air mass flow rate, kg/s
p	pressure, N/m^2
\dot{W}	flow power, W
q	heat transfer per unit mass, J/kg
q''	heat flux, W/m^2
R	air specific gas constant, $J/kg.K$
T	temperature, K

ρ density, kg/m^3
 u velocity, m/s
 c_p specific heat capacity, $J/kg.K$

Subscripts

i inlet
 o outlet
 c collector
 t tower
 m mean
 ∞ ambient air
 $turb$ turbine
 atm atmospheric

Abbreviations

CFD computational Fluid Dynamics
EOS equation of state
SCPPS solar chimney power plant system
RHS right hand side
M&S modeling and simulation

1.1 Introduction

Although the idea of the SCPPS can be traced to the early 20th century, practical investigations of solar power plant systems started in the late 1970s, around the time of conception and construction of the first prototype in Manzanares, Spain. This solar power plant operated between 1982 and 1989 and the generated electric power was used in the local electric network [1–3].

The basic SCPPS concept (Fig. 1.1) demonstrated in that facility is fairly straightforward. Sunshine heats the air beneath a transparent roofed collector structure surrounding the central base of a tall chimney. The hot air produces an updraft flow in the chimney. The energy of this updraft flow is harvested with a turbine in the chimney, producing electricity. Experiments with the prototype proved the concept to be viable, and provided data used by a variety of later researchers. A major motivation for subsequent studies lays in the need for reliable modeling of the operation of a large-scale power plant. The Manzanares prototype had a 200 m tall chimney and a 40,000 m² collector area. With respect to the distinguished rise of R&D budget on renewable energy [5], study and evaluation the different aspects of SCPPS seem beneficial and vital. Proposals for economically competitive SCPPS facilities usually feature chimneys on the scale of 1 km and collectors with multiple square kilometer areas.

Padki and Sherif [6] used the results from the Manzanares prototype to extrapolate the data to large scale models for SCPPS. In 1991, Yan et al. [7] developed

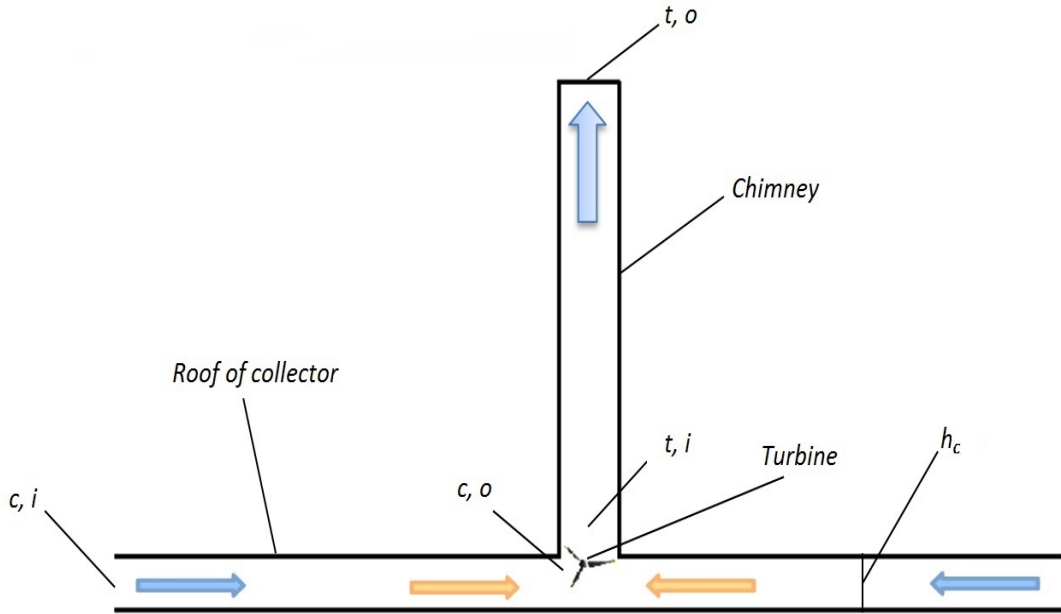


FIGURE 1.1: Schematic of SCPPS with the applied variables and subscripts in the present analysis

an SCPPS model using a practical correlation. They introduced equations including air velocity, air flow rate, output power, and thermofluid efficiency. Von Backström and Fluri conducted a numerical study to determine the optimum ratio of pressure drop of the turbine as a fraction of the available pressure difference required to achieve the maximum power [8]. They noted that this ratio might lead to overestimating the flow passage in the plant and also designing a turbine without a sufficient stall margin. In other recent works, the SCPPS concept involving an inflatable tower was examined, with all parts of the power plant modeled numerically [9–11].

To find the maximum power, different atmospheric pressure and temperature boundary conditions were applied for various tower heights and atmospheric lapse rates [12, 13]. Theoretical analysis to study the effect of pressure drop in the

SCPPS turbine was performed by Koonsrisuk et al. [14]. The optimal pressure drop ratio was found numerically and analytically by Xu et al., around 0.9 for the Manzanares prototype. This investigation can be applied as an initial estimation for various SCPPS turbines [15].

Earlier modeling efforts [9] showed a keen sensitivity of the predictions of SCPPS output to boundary conditions, in particular, pressure. Numerical simulations require careful validation and verification, and for that, analytical models are indispensable. A theoretical model was recently developed [16] to model the combined performance of the solar collector, chimney, and turbine. Here we will examine some of the assumptions and derivations in this model and present an alternative formulation for the energy equation. We will perform M&S of the Manzanares prototype and compare the computational results against the available experimental values and our analytical analysis data. This comparative study is carried out for different solar radiation based on available experimental data.

1.2 Analytical Study

1.2.1 Collector

Solar Chimney Power Plants provide a reliable and conceptually straightforward way of energy generation from the solar irradiation[14, 17]. A solar collector is the main and only component of this power plant to accumulate the available solar energy to heat up air in a greenhouse. The air escapes the collector through a

tall chimney which connects the warm air flow of the collector with the cooler air above the ground. The temperature difference induces the natural convection, and turbine at the outlet of collector harvests the energy of the air flow. To model the collector, the simplified one dimensional mathematical analysis was performed to clarify the details. The analytical correlation will be applied later to compare the CFD results against it. To derive the equations, we start from the collector. It is assumed that the flow through the collector is one-dimensional, steady-state, and compressible. Let us disregard the friction and assume the total heat from the solar irradiation is absorbed within the air filling the collector. For this thermal-fluid analysis, the mass conservation satisfies:

$$\frac{dA}{A} + \frac{d\rho}{\rho} + \frac{du}{u} = 0 \quad (\text{Continuity}) \quad (1.1)$$

Here A is the cross-sectional area of the collector that air goes through – $A = 2\pi r h_c$ and $dA = 2\pi r dh_c$.

Momentum equation is as follows:

$$dp + \rho u du = 0 \quad (\text{Momentum}) \quad (1.2)$$

Consider the energy balance equation and the equation of state as follows:

$$c_p dT - dq + u du = 0 \quad (\text{Energy}) \quad (1.3)$$

$$dp = d(\rho RT) \quad (\text{State}) \quad (1.4)$$

To find dp we can apply Eq. (1.2) and substitute du/u from the continuity equation, Eq. (1.1).

$$dp = \rho u^2 \left(\frac{d\rho}{\rho} + \frac{dA}{A} \right) \quad (1.5)$$

From the equation of state we can find $d\rho/\rho$ and substitute in Eq. (1.5),

$$\frac{d\rho}{\rho} = \frac{dp}{p} - \frac{dT}{T} \quad (1.6)$$

$$dp = \rho u^2 \left(\frac{dp}{p} - \frac{dT}{T} + \frac{dA}{A} \right) \quad (1.7)$$

We can rewrite Eq. (1.7) as a function of T, A, u, p, ρ and \dot{m} , where $\dot{m} = \rho Au$. Also by substitution dT from the energy equation on the base of dq, c_p and u , we obtain

$$dp = \frac{\dot{m}^2}{\rho} \left(\frac{dA}{A^3} - \frac{dq - udu}{A^2 T c_p} + \frac{dp}{A^2 p} \right) \quad (1.8)$$

For consistency with previous analyses, let us rewrite dq on the basis of heat flux, available solar insolation to the air, per mass flow rate— $dq = q'' dA_r / \dot{m}$ where q has the units of J/kg . Here $A_r = \pi r^2$, therefore $dA_r = 2\pi r dr$ [14, 18]. Note that

$A = 2\pi r h_c$, where h_c is the collector height (roof height) that was assumed to be constant. By substituting A_r , dq and A in the second term on the RHS, we obtain

$$dp = \frac{\dot{m}^2}{\rho} \left(\frac{dA}{A^3} - \frac{q''(2\pi r)dr}{\dot{m}(2\pi r h_c)^2 T c_p} + \frac{udu}{A^2 c_p T} + \frac{dp}{A^2 p} \right) \quad (1.9)$$

We can rewrite equation (1.9) and substitute udu of the third term on the RHS by applying momentum equation (1.2), $udu = -dp/\rho$ and $p = \rho RT$.

$$dp = \frac{\dot{m}^2}{\rho} \left[\frac{dA}{A^3} - \frac{q'' dr}{2\pi \dot{m} r h_c^2 c_p T} \right] \left[1 - \frac{u^2}{T} \left(\frac{1}{R} - \frac{1}{c_p} \right) \right]^{-1} \quad (1.10)$$

Equation (1.10) is the exact solutions for dp for the one-dimensional frictionless analysis of the collector. Since our fluid is air we can estimate c_p and rewrite Eq. (1.10).

$$dp \simeq \frac{\dot{m}^2}{\rho} \left(\frac{dA}{A^3} - \frac{q'' dr}{2\pi \dot{m} r h_c^2 c_p T} \right) \left(1 - \frac{2.494u^2}{T} \right)^{-1} \quad (1.11)$$

c_p , q'' and T are considered approximately constant as well. The last term on the RHS of (1.11) is close to unity within the range of velocities and temperatures under consideration. Therefore by integrating between the inlet and outlet of the collector without the last term of the RHS, pressure difference can be derived.

$$\int_{c,i}^{c,o} dp \simeq \int_{c,i}^{c,o} \left(\frac{\dot{m}^2 dA}{\rho A^3} - \frac{\dot{m} q'' dr}{2\pi r h_c^2 \rho c_p T} \right) \quad (1.12)$$

$$p_{c,o} - p_{c,i} \simeq \left[\frac{\dot{m}^2}{2\rho_{m,c}} \left(\frac{1}{A_{c,i}^2} - \frac{1}{A_{c,o}^2} \right) + \frac{q'' \dot{m}}{2\pi h_c^2 c_p \rho_{m,c} T_{m,c}} \ln \frac{r_{c,i}}{r_{c,o}} \right] \quad (1.13)$$

Equation (1.13) represents the pressure difference along the collector due to change in the flow area (first term) and as a result of the solar radiation (second term). $T_{m,c}$ and $\rho_{m,c}$ are considered as the average values of the inlet and outlet of the collector. To consider the change of density due to temperature change, we consider the Boussinesq approximation as follows,

$$\rho_{c,i} - \rho_{c,o} = \frac{\rho_{c,i}(T_{c,o} - T_{c,i})}{T_{c,i}} \quad (1.14)$$

In the collector, air temperature rises due to the available radiation and therefore density decreases proportionally with respect to the temperature that can be calculated by (1.14). The nominal value of the temperature rise in Manzanares SCPPS was 20K. Note that q'' is the available solar insolation to the air, means due to the ground radiative factors and also heat losses from the collector q'' is less than the ideal irradiance. We present our performance study due to the collector efficiency to cover all these factors in the result and discussion section.

1.2.2 Tower

The air flow in the chimney is considered as an adiabatic frictionless flow. The conservation equations for the one-dimensional steady state flow in variable-area

tower are similar to collector except having the gravity term in momentum and energy equations.

By following the same trend to find dp we get

$$dp = \left[-\rho g dz + \frac{\dot{m}^2 dA}{\rho A^3} + \rho u^2 \left(\frac{dp}{p} - \frac{dT}{T} \right) \right] \quad (1.15)$$

By applying the energy equation, substitution $dT = (-gdz - udu)/c_p$ and $dp = -\rho(udu + gdz)$, we can rewrite the above equation as

$$dp = \left[-\rho g dz + \frac{\dot{m}^2 dA}{\rho A^3} + \rho u^2 \left(\frac{dp}{p} - \frac{dp}{\rho c_p T} \right) \right] \quad (1.16)$$

Also by considering the material properties of air the same way we did for the collector part,

$$dp \simeq \left[-\rho g dz + \frac{\dot{m}^2 dA}{\rho A^3} \right] \left[1 - \frac{2.494u^2}{T} \right]^{-1} \quad (1.17)$$

The above equation is the exact closed form solution for dp at any point as the function of variables ρ , T . The last term on the RHS can be assumed to equal unity as we mentioned in the collector part. Let integrate between the inlet and outlet tower area to find the pressure difference of the chimney as,

$$\int_{t,i}^{t,o} dp \simeq \int_{t,i}^{t,o} \left(-\rho g dz + \frac{\dot{m}^2 dA}{\rho A^3} \right) \quad (1.18)$$

$$p_{t,o} - p_{t,i} \simeq -\rho_{m,t}gh_t - \frac{\dot{m}^2}{2\rho_{m,t}} \left(\frac{1}{A_{t,o}^2} - \frac{1}{A_{t,i}^2} \right) \quad (1.19)$$

Where $\rho_{m,t} = (\rho_{t,i} + \rho_{t,o})/2$ and we can correlate the outlet tower pressure to the atmospheric density and the inlet collector pressure for an adiabatic tower, $p_{c,i} = p_{t,o} + \rho_{\infty}gh_t$. The air density change can be calculated by lapse rate temperature change due to the height change $T_{t,o} = T_{\infty} - gh_t/c_p$. Therefore by applying equation (1.14) in the polytropic EOS we obtain,

$$p_{t,o} = p_{\infty} \left(1 - \frac{gh_t}{c_p T_{\infty}} \right)^{\left(\frac{c_p}{R} \right)} \quad (1.20)$$

We calculate the density at the tower outlet by having the tower outlet pressure from EOS. For an adiabatic tower-collector connection, if we do not consider a turbine (pressure change) in our model, we can assume $\rho_{t,i} = \rho_{c,o}$.

Also $T_{\infty} = T_{c,i}$ and we can rewrite equation (1.14) as follows,

$$\rho_{t,i} = \rho_{c,o} = \rho_{\infty} \left(1 + \frac{T_{\infty} - T_{c,o}}{T_{\infty}} \right) \quad (1.21)$$

In Manzanares prototype the circular cross sectional area of the tower does not change, therefore for the pressure difference at the tower we obtain,

$$p_{t,o} - p_{t,i} \simeq -\rho_{m,t}gh_t \quad (1.22)$$

1.2.3 Turbine

The Manzanares SCPPS turbine was mounted freely from the collector on a steel framework 9 m above ground level (see Fig 1.2). Four turbine blades are adjustable according to the face velocity of the air in order to achieve an optimal pressure drop across the turbine blades [1]. To calculate the output power, we can define the power on the basis of the pressure difference at the turbine – where it is normally utilized at the outlet of the collector and inlet of the tower. Change of the static pressure converts into rotational mechanical work. The ideal available power from the pressure difference is proportional to the mass flow rate and the pressure drop at the turbine location.



FIGURE 1.2: Manzanares prototype turbine [4].

$$\dot{W} \simeq \frac{\dot{m}(p_{c,o} - p_{t,i})}{\rho_{turb}} \quad (1.23)$$

For area the following equations is used, where b is an arbitrary positive real constant.

$$A_{c,i}^2 = bA_{c,o}^2, \quad (1.24)$$

Let $\rho_{turb} = (\rho_{c,o} + \rho_{t,i})/2$ and substitute equations $p_{c,o}$ and $p_{t,i}$ from (1.13) and (1.22). Hence for the flow power by assuming $p_{c,i} = p_{t,o} + \rho_{\infty}gh_t$, we have

$$\dot{W} \simeq \frac{\dot{m}}{(\rho_{c,o} + \rho_{t,i})/2} \left[\frac{-\dot{m}^2}{2\rho_{m,c}} \left(\frac{b-1}{bA_{c,o}^2} \right) + \frac{q'' \dot{m}}{2\pi h_c^2 c_p \rho_{m,c} T_{m,c}} \ln \frac{r_{c,i}}{r_{c,o}} + (\rho_{\infty} - \rho_{m,t})gh_t \right] \quad (1.25)$$

The first term on RHS of equation (1.25) presents the effect of the flow area change and it reduces the available pressure difference with respect to the typical shape of SCCPS. The second term represents the effect of the available solar radiation to the collector and the third term calculates the stack effect with respect to the available mean density difference along the tower and before the turbine. To calculate the output power from the available pressure difference in a realistic form, we consider,

$$P_t = \eta_c \dot{W} \quad (1.26)$$

Where η_c is the collector efficiency factor. Based on the 1982 experiments [1], the reported value, 0.32, for the Manzanares prototype collector efficiency would be considered in this analysis.

1.3 Numerical Analysis

To perform CFD analysis, the finite volume method was employed via ANSYS/FLUENT M&S package. The air flow as an ideal gas under Boussinesq effect by solar irradiation was simulated. In the present CFD analysis the mass flow rate, obtained from the CFD results, along with other parameters were used to evaluate the maximum mechanical power for each case. The flow of air in SCPPS was assumed steady (in the average flow sense) and axisymmetric with respect to the chimney centerline. The meshed SCPPS axisymmetric model is shown in Fig. 1.3 with the details of applied boundary condition. ANSYS ICEM (Integrated Computer Engineering and Manufacturing) CFD was employed to generate a quadrilateral cell mesh. To perform the CFD simulation, the standard $k - \epsilon$, which is classified as a two-equation turbulence model, was applied. In this model, with respect to the sensitivity of the pressure solver to the density change, the density of air is calculated from the ideal gas equation. Stated differently, EOS was applied to calculate the air density with respect to the updated values of the pressure and temperature from the Navier Stokes equation results. The pressure boundary conditions at the entrance of the collector and the outlet of the chimney were assumed as atmospheric pressure and identical. The discretization accuracy of the

CFD solver is second order upwind for the density and momentum equation. Semi-implicit method for pressure-linked equations (SIMPLE) algorithm was applied as the pressure-velocity coupling to solve the pressure field. The chimney wall and the collector roof were considered adiabatic and the solar radiation was introduced to the ground as a constant heat flux. The residual criteria for all equations were set to be calculated and iterated not to exceed 10^{-6} . The calculations were done by using a 16-core, 32 GB RAM computer.

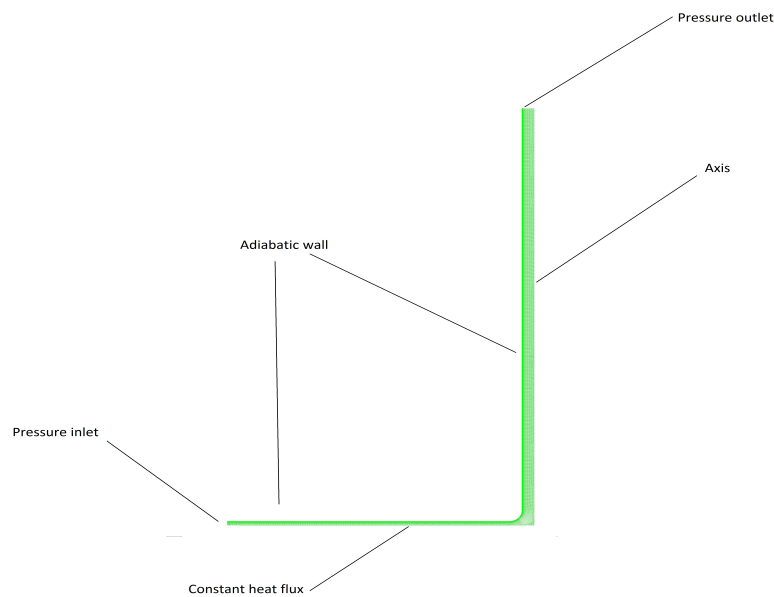


FIGURE 1.3: Computational domain and applied boundary conditions.

1.4 Results and Discussion

To evaluate the derived analytical solution for the output power of SCPPS, the available experimental data from Manzanares prototype was applied and extracted. The measured updraft velocity of Manzanares power plant for 24 hours operation

is substituted into the analytical solution (equation (1.26)) and compared against the experimental output power from the turbine (Fig. 1.4). Figure 1.4 presents the sixth order polynomial trend of data. Considering a constant collector efficiency (η_c) as 0.32 for the whole 24-hour analysis, the total output power would be closer against the experimental data for higher solar radiation. The initial difference between the analytical and experimental values—light orange area (Fig. 1.4)—is due to the minimum stack effect (chimney effect) by considering the minimum reported measured velocity— 2 m/s during 12-1 am —flowing up to the chimney by the height of 194.6 m. However, it was obtained from the experimental analyses that the turbine has a minimum start up updraft velocity as 2.5 m/s and would not rotate for low velocities. Based on reported values from the Manzanares prototype [1] the maximum measured output power for 9m/s updraft velocity was 50kW—without any decimal precision. By imposing the same updraft velocity (9 m/s) at the turbine location, and applying the same collector efficiency (32%) and loss factor (0.9) the analytical output power would be 51.26 kW.

To have the characteristics of the Manzanares prototype we study the sensitivity of the analytical output power correlation to the mass flow rates. Therefore, the effect of mass flow rate on each terms of the total pressure change, including, inter alia, air flow geometry, solar radiation and stack effect would be observed. We performed this sensitivity analysis for a range of solar irradiation versus mass flow rate. It is observed that by increasing the mass flow rate the output power increases as long as the stack effect dominated the negative pressure difference due to the change of flow area. The dominant terms in the total pressure difference

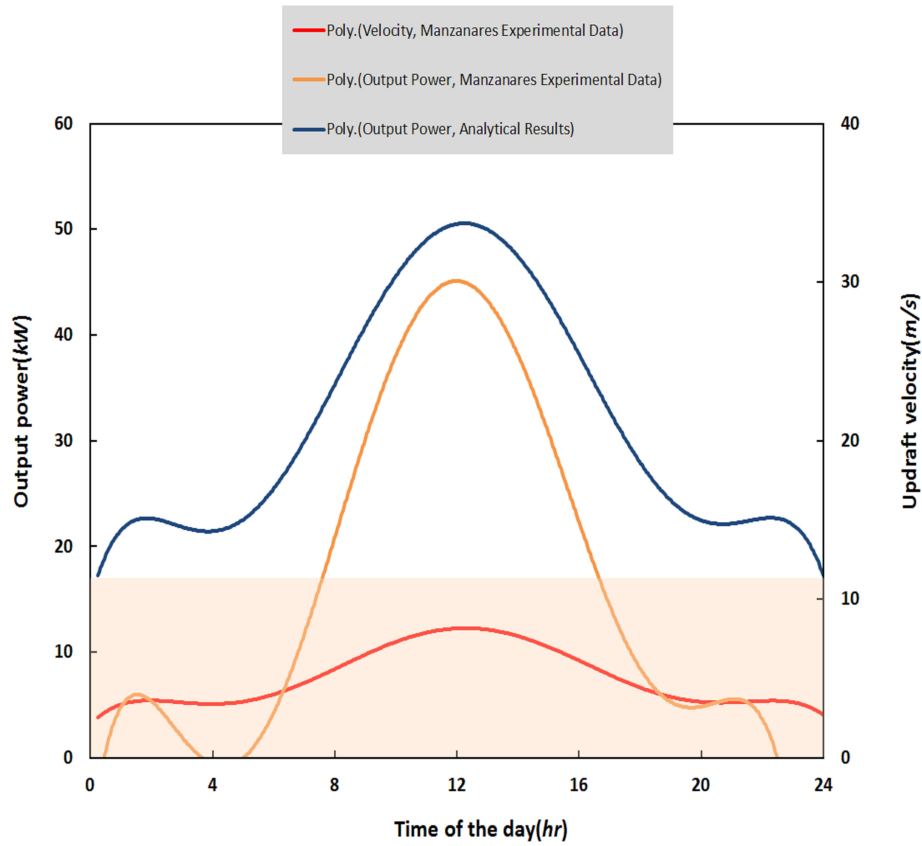


FIGURE 1.4: Analytical power results against measurement from Manzanares: updraft velocity and power output for a typical day.

are the flow area change and the stack effect terms. Since the flow is well within subsonic range, the inlet and outlet flow areas of the collector play the same role as nozzles and the pressure change of the nozzle flow is negative. By increasing the flow rate we reach to the theoretical maximum output power for each amount of solar irradiation. However, after the maximum power the dominant term is the negative pressure change due to the air flow area. Stated differently, after reaching to the the maximum theoretical output power, the positive-pressure change which rotates the turbine blade decreases by growing the pressure drop term due to the nozzle effect (Fig. 1.5). As it was mentioned before and shown in figure 1.5, the maximum power for the experimental velocity (9 m/s) is 51.2 kW . However, the maximum theoretical power from the characteristics of Manzanares SCPPS for

1000 (W/m^2) solar irradiation is 51.8 kW. The output power characteristics with respect to mass flow rate can be useful for design or rating step of SCCPS.

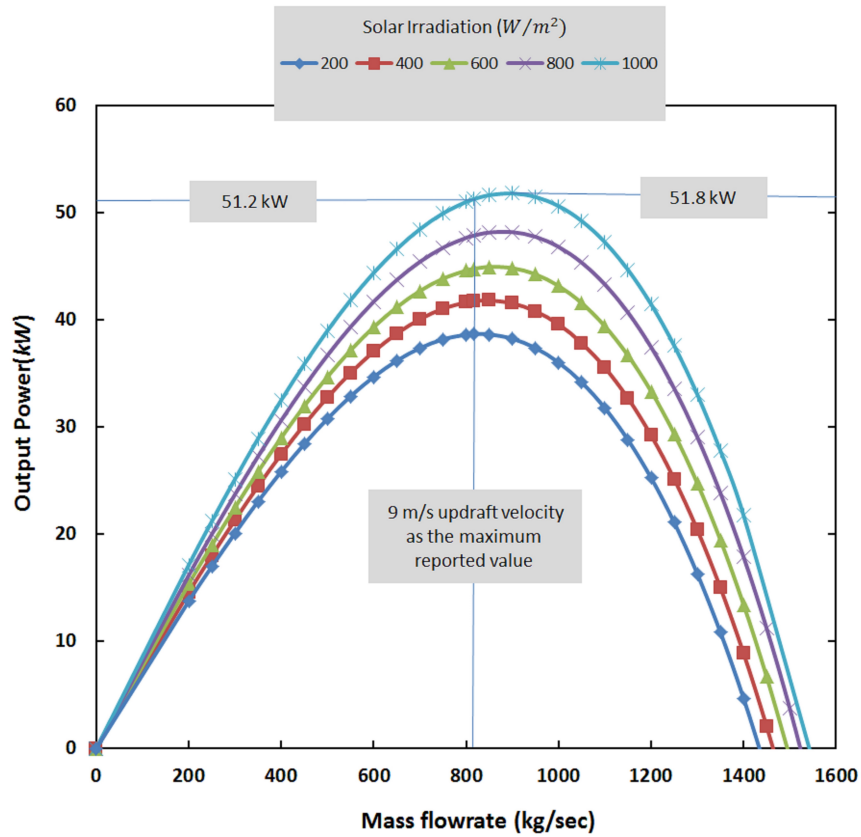


FIGURE 1.5: Analytical power results against mass flow rate for a range of solar irradiation.

To study the role of collector efficiency factor, we calculate the analytical output power for the maximum reported solar irradiation as the operating reported case for the output power of 50kW. Figure 1.6 depicts the logarithmic scale variation of output power with respect to a range of mass flow rate for different collector efficiency factors. Collector efficiency factor varies from 0.1 to 1 and can be considered as the overall adjusted efficiency factor. The ideal ($\eta_c = 1$) maximum output power for 1000 (W/m^2) solar irradiation is 161.7 kW from the analytical solution (Fig 1.6).

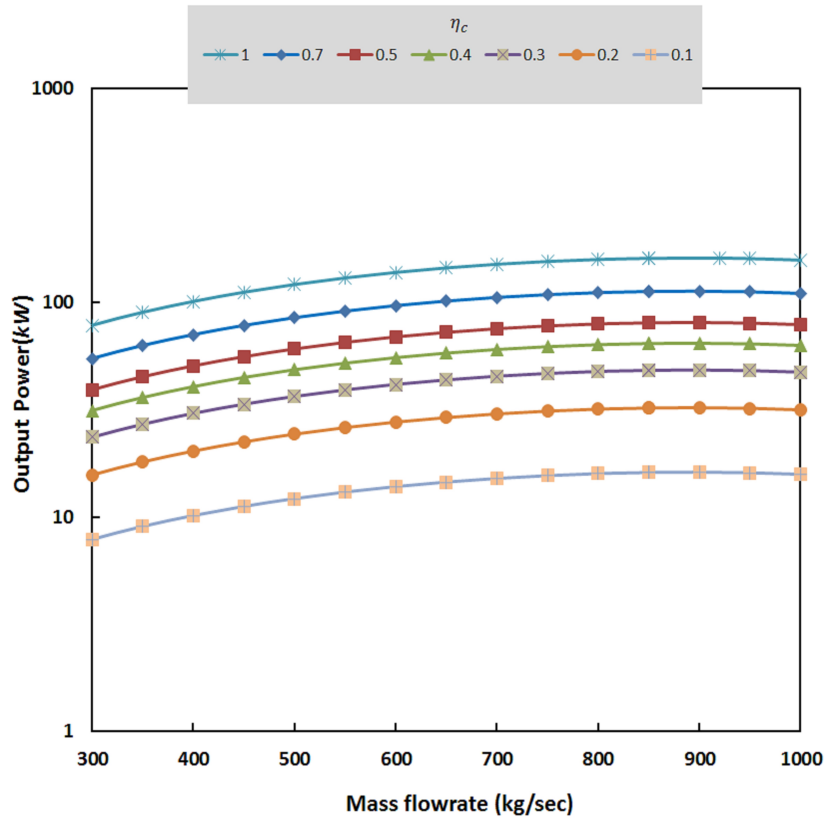


FIGURE 1.6: Analytical power results against mass flow rate for different values of collector efficiency.

To obtain the available power to rotate the turbine, the kinetic energy of the air flow at the outlet of the collector was calculated. For each CFD analysis (Fig. 1.7), the mass flow rate and the average density at the turbine location are gained from the numerical simulation result and used to calculate the available kinetic energy per time. The calculated available power for different solar irradiation are compared against the experimental data and the analytical solution in two cases. Analytic-EXP shows the power where the average velocity were obtained from the available experimental data at the same amount of reported radiation. It is needless to say that details of available experimental data are not clear enough to report the data with all sources of uncertainty(Fig. 1.8). The reliability of experimental data is suggested to measure for future works. CFD results were

performed under the ideal assumption of having no heat loss from the tower or collector. Also we imposed the available heat flux as a boundary condition. Stated differently, in the CFD analysis we introduced the flow domain e.g. 1000 W/m^2 where in the experiment the amount of reported velocity at 1000 W/m^2 solar radiation is lower because of the absorptivity factor of the collector ground. The available power at the turbine location, CFD in Fig. 1.7, by using the CFD values for density and velocity were calculated based on the rate of kinetic energy, $0.5\dot{m}u^2$. Two different ratios of the available kinetic energy at the turbine location are used for SCCPS analysis. One is referred as Betz criterion or Betz limit which is $16/23$ and was formulated in 1919. Betz criterion is the theoretical power fraction that can be extracted from an ideal wind stream. The other one is $2/3$ and were used in several investigations. The CFD results that have been calculated by Betz criterion and $2/3$ are shown as CFD-Betz and CFD- $2/3$ respectively (Fig. 1.8). It is shown as CFD-Betz The difference between the available power from simulation results (CFD) and the experimental turbine power is due foremost to the turbine efficiency and then having no heat loss in the CFD model.

1.5 Conclusion

We presented a combined numerical-analytical analysis for solar chimney power plant, based on the Manzanares prototype. The harvestable power of Manzanares power plant was investigated as the function of available solar irradiation and mass flow rate. The CFD M&S was carried out. Also the one-dimensional analytical analysis was done with attention to underlying assumptions and simplifications.

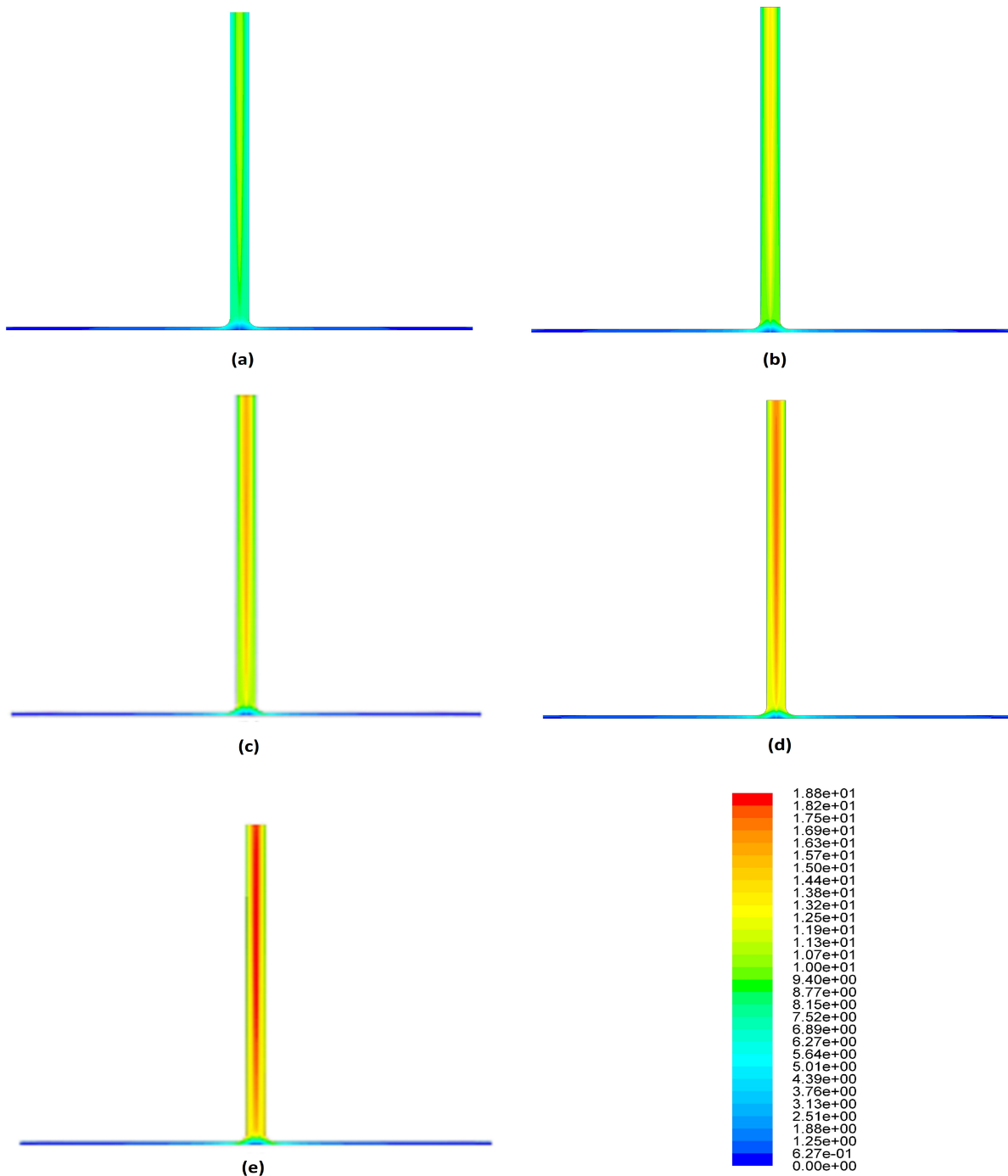


FIGURE 1.7: Velocity contour plot (m/s) for different available solar heat flux at the ground of collector, (a):200, (b):400, (c):600, (d):800, (e)1000 W/m^2 .

We compared the numerical results against the available limited raw experimental data from the prototype and also showed the range of reliability of the analytical solution. Where the inlet velocity values for analytical correlation were obtained

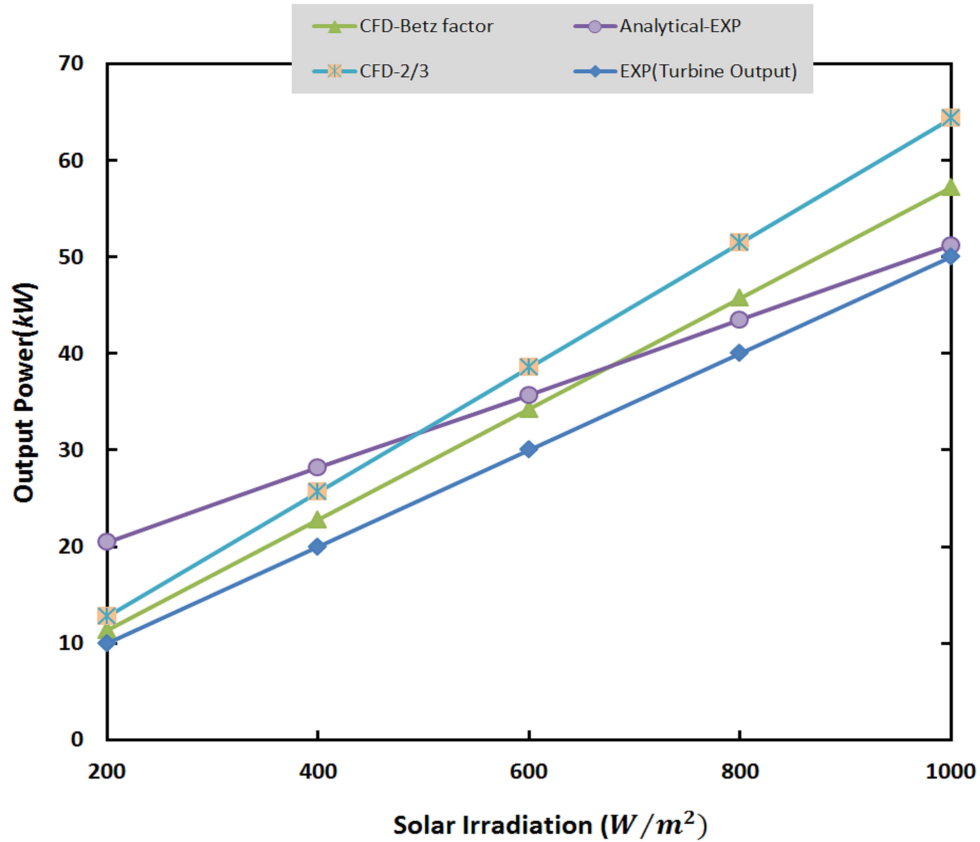


FIGURE 1.8: Power vs solar irradiation.

from the experimental velocities we got higher available power than the output turbine power. This difference increases for lower solar irradiation and mass flow rate values due to the stack effect term in the analytical solution. That has several reasons as, (a) The one dimensional analytical solution has several simplifications, including treatment of average density and the heat flux term., (b) It is very important to pick the right source to impose the values to the analytical correlation., (c) Available experimental data are not just limited, but also not extensively characterized in terms of uncertainty and repeatability, making it difficult to produce error bars on experimental values for a prescribed level of confidence. To present the volatility of the analytical correlation, we selected two

different approaches to input values in this one-dimensional equation; I- Imposing the experimental velocities and calculation densities with respect to average temperature., II- Applying a range of mass flow rates to obtain the characteristics of Manzanares prototype analytically. During the verification and validation process, the modeler must ask two questions: *Am I modeling the physics correctly?* and *Am I modeling the correct physics?* Comparison with analytical models is important for answering both of these questions, and the only way to have them well-posed is to have correct physics in the analytics.

Bibliography

References

- [1] Haaf, W., K. Friedrich, G. Mayr, and J. Schlaich. "Solar chimneys part I: principle and construction of the pilot plant in Manzanares." *International Journal of Solar Energy* 2, no. 1 (1983): 3-20.
- [2] Haaf, W. "Solar chimneys: part ii: preliminary test results from the Manzanares pilot plant." *International Journal of Sustainable Energy* 2, no. 2 (1984): 141-161.
- [3] Schlaich, Jörg, Michael Robinson, and Frederick W. Schubert. *The solar chimney: electricity from the sun*. Geislingen, Germany: Axel Menges, (1995).
- [4] Schlaich, Jorg, Rudolf Bergermann, Wolfgang Schiel, and Gerhard Weinrebe. "Design of commercial solar updraft tower systems—utilization of solar induced convective flows for power generation." *Journal of Solar Energy Engineering* 127, no. 1 (2005): 117-124.
- [5] Zohuri, Bahman, and Nima Fathi. "Thermal-hydraulic analysis of nuclear reactors." New York: Springer, 2015.

- [6] Padki, M. M., and S. A. Sherif. "Solar chimney for medium-to-large scale power generation." In Proceedings of the manila international symposium on the development and management of energy resources, vol. 1, pp. 432-437. 1989.
- [7] Yan, M. Q., S. A. Sherif, G. T. Kridli, S. S. Lee, and M. M. Padki. "Thermo-fluid analysis of solar chimneys." In Industrial Applications of Fluid Mechanics-1991. Proceedings of the 112th ASME winter annual meeting, Atlanta, GA, pp. 125-130. 1991.
- [8] Von Backström, Theodor W., and Thomas P. Fluri. "Maximum fluid power condition in solar chimney power plants—an analytical approach." *Solar Energy* 80, no. 11 (2006): 1417-1423.
- [9] Putkaradze, Vakhtang, Peter Vorobieff, Andrea Mammoli, and Nima Fathi. "Inflatable free-standing flexible solar towers." *Solar Energy* 98 (2013): 85-98.
- [10] Fluri, T. P., and T. W. Von Backström. "Performance analysis of the power conversion unit of a solar chimney power plant." *Solar Energy* 82, no. 11 (2008): 999-1008.
- [11] Peter Vorobieff, Andrea Mammoli, Nima Fathi, and Vakhtang Putkaradze. "Free-standing inflatable solar chimney: experiment and theory." *Bulletin of the American Physical Society* 59 (2014).
- [12] Nima Fathi, Peter Vorobief, Seyed Sobhan Aleyasin. "V&V Exercise for a Solar Tower Power Plant." *ASME Verification and Validation Symposium* (2014).

<https://cstools.asme.org/csconnect/FileUpload.cfm?View=yes&ID=44167>

- [13] Zhou, Xinping, Jiakuan Yang, Bo Xiao, Guoxiang Hou, and Fang Xing. "Analysis of chimney height for solar chimney power plant." *Applied Thermal Engineering* 29, no. 1 (2009): 178-185.
- [14] Koonsrisuk, Atit, and Tawit Chitsomboon. "Theoretical turbine power yield in solar chimney power plants." In *Thermal Issues in Emerging Technologies Theory and Applications (ThETA)*, 2010 3rd International Conference on, pp. 339-346. IEEE, 2010.
- [15] Xu, Guoliang, Tingzhen Ming, Yuan Pan, Fanlong Meng, and Cheng Zhou. "Numerical analysis on the performance of solar chimney power plant system." *Energy Conversion and Management* 52, no. 2 (2011): 876-883.
- [16] Koonsrisuk, Atit, and Tawit Chitsomboon. "Mathematical modeling of solar chimney power plants." *Energy* 51 (2013): 314-322.
- [17] Zhou, Xinping, Fang Wang, and Reccab M. Ochieng. "A review of solar chimney power technology." *Renewable and Sustainable Energy Reviews* 14, no. 8 (2010): 2315-2338.
- [18] Koonsrisuk, Atit, and Tawit Chitsomboon. "Effects of flow area changes on the potential of solar chimney power plants." *Energy* 51 (2013): 400-406.

Chapter 2

Experimental-Computational Analysis of Multi-inlet and Conventional Collectors¹

Solar chimney power plant systems (SCPPS) offer a simple and reliable way to generate electricity using solar radiation to drive a flow of buoyant air. A typical SCPP setup includes a collector, a tower, and a turbine or several turbines. Current SCPP designs have low thermal efficiency: only between 0.5% and 5% of the incident solar energy is converted into electricity. Inefficiencies result partially from limited mass flow rates through the tower. It is therefore desirable to provide a new design for the collector to increase the inlet air mass flow rate. In this paper, we present a double-inlet collector concept and results of numerical

¹Originally to be published as: Fathi, Nima, Seyed Sobhan Aleyasin, Patrick Wayne, and Peter Vorobieff. "Computational Assessment of Double-Inlet Collector in Solar Chimney Power Plant Systems", ASME Fluids Engineering Division Summer Meeting (FEDSM) Transaction, 2017.

analysis to evaluate this design in terms of flow rate improvement. Computational fluid dynamics (CFD) was utilized to perform the numerical modeling and simulation (MS) by using a finite volume method package. The Manzanares prototype (the only operational solar tower power plant with available published reports) is selected to implement the double-inlet collector design and study its effect on the power plant. Beside this case, we fabricated a 1/1000 scale model of the Manzanares prototype which enables us to measure the field variables experimentally. Validation analysis was performed to quantify the reliability of our numerical model with respect to the available experimental data. We obtained a significant increase (14%) in the available output power by using the double-inlet collector.

Nomenclature

Variables

A	cross-sectional area, m^2
A_r	cross-sectional area of the collector ground, m^2
g	acceleration due to gravity, m/s^2
h	height, m
\dot{m}	air mass flow rate, kg/s
p	pressure, N/m^2
\dot{W}	flow power, W
q	heat transfer per unit mass, J/kg
q''	heat flux, W/m^2

R	air specific gas constant, $J/kg.K$
T	temperature, K
ρ	density, kg/m^3
u	velocity, m/s
c_p	specific heat capacity, $J/kg.K$
D	experimental data
S	simulation result

Subscripts

i	inlet
o	outlet
c	collector
t	tower
m	mean
∞	ambient air
$turb$	turbine
atm	atmospheric

Abbreviations

CFD	computational fluid dynamics
EOS	equation of state
IGV	inlet guide vanes
$M\&S$	modeling and simulation

- PIV* particle image velocimetry
- RHS* right hand side
- SCPPS* solar chimney power plant system

2.1 Introduction

Solar energy is one of the promising renewable energy sources, as the annual amount of energy sufficient for the needs of our civilization is delivered to Earth by the Sun in only one hour [1]. Therefore, developing new technologies which can harvest solar energy efficiently is a prime importance. One of these technologies is solar chimney power plants (SCPP) which not only provide electricity on a large scale but also increase the chance of precipitation, even in low-humidity desert regions, and support the agriculture around the SCPP. In a solar chimney plant, the energy of buoyant hot air is converted to electrical energy. The plant consists of a collector at the base covered with a transparent roof that collects the solar radiation, heating the air inside and the ground underneath. In the center of the collector, there is a tower, and a turbine is located at its base. The hot air flows up the tower as a result of its buoyancy, and its energy is extracted and converted to electricity with the turbine. A typical solar chimney is shown in Fig. 2.1 .

Since the efficiency of SCPP as sketched is relatively low, for commercial SCPP the chimney and collector need to be built on a very large scale which results in

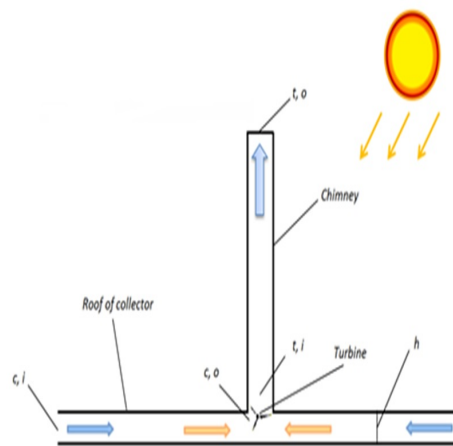


FIGURE 2.1: Schematic of a solar chimney power plant

high capital cost. Therefore any improvement in efficiency that leads to fabrication of smaller and less expensive SCPP can make the output electricity more competitive. Toward this end, since the successful construction and operation of Manzanares prototype in 1982 [2], considerable research efforts have been undertaken to improve the efficiency of SCPP and advance our knowledge in this area. An analytical and numerical study describes the influence of the chimney height, collector area, and pressure drop factor at the turbine on the output power of SCPP [3]. The output power was found to be proportional to the volume included within the chimney height and the collector area. In an effort to improve the efficiency of the collector and reduce its fabrication cost, Bonnelle [4] proposed a collector with ribs containing their branching. This concept provides larger entrance area, smaller air velocity, and lower friction under a lower roof compared with the conventional collector for the same flow rate. Bernardes et al. [5] analyzed the horizontal to vertical flow passage from the collector to the chimney for various designs including straight, curved, slanted junctions, and a conic chimney.

It was observed that the conic chimney had a higher mass flow rate and temperature at the outlet while the straight junction gave the smallest flow rate due to the occurrence of recirculation. During night time, as there is no solar energy to heat up the air, the only source of energy is the heated soil under the collector, which may not be sufficient for effective operation of SCPP. To address this issue various solutions such as inclusion of closed water-filled thermal storage system on the collector ground [6], usage of waste heat from nuclear power plants [7], and inclusion of an intermediate secondary roof under the first collector roof [8] have been suggested. In the latter design, the collector is divided into a top and bottom section. In the top section the air flows constantly, while in the bottom section the air flow can be regulated to store the energy during the day and release it at night [8]. It is widely known that, based on Betz's law [9], the maximum possible power that can be extracted by a free-standing wind turbine is limited to 59% of the kinetic energy of the wind. For a ducted turbine (as in the SCPP), 75% to 85% of the flow energy can be extracted, taking into account losses associated with conversion from mechanical to electrical energy [10]. In other recent works, the SCPPS design involving an inflatable tower was evaluated experimentally and numerically and validation assessment was performed for a small prototype [11, 12]. Various turbine configurations have been proposed to replace the conventional single vertical axis turbine. The multiple vertical axis and the multiple horizontal axis turbine configurations are among them [13, 14]. Fluri and von Backström [14] found that the single vertical axis turbine had a slightly higher efficiency and energy yield compared to the layouts with multiple axis turbines, as certain loss mechanisms were not present in the former. However, studies revealed that the peak output

torques were considerably lower in the configurations with multiple turbines which may reduce the cost, particularly for the generators. In addition, the effects of inlet guide vanes (IGV) and counter-rotating rotors on the performance of the turbines have been studied [15, 16]. It was found that the counter-rotating turbines without IGV had lower design efficiency but higher off-design performance over a single-rotor turbine [15]. In this investigation, we propose a new conceptual design of a double-inlet collector for SCPPS. We study the change of output power of the power plant due to implementation of this design, and compare its performance with that of a traditional collector.

2.2 Conceptual Design

Our idea is to consider more than one inlet for the SCPPS collector. This novel design is a part of a pending patent [17]. Until now, none of the SCPPS collectors have been built with more than one inlet. Having the secondary inlet can increase the total inlet air mass flow rate which leads to a higher harvestable kinetic energy for the turbine to produce electricity. Fig. 2.2 presents the traditional (case A) and proposed double-inlet collector (case B) schematically.

2.3 Modeling and Simulation Approach

To evaluate the effect of having an extra inlet in the collector on the overall power plant performance, we modeled case B using ANSYS modeling package based on

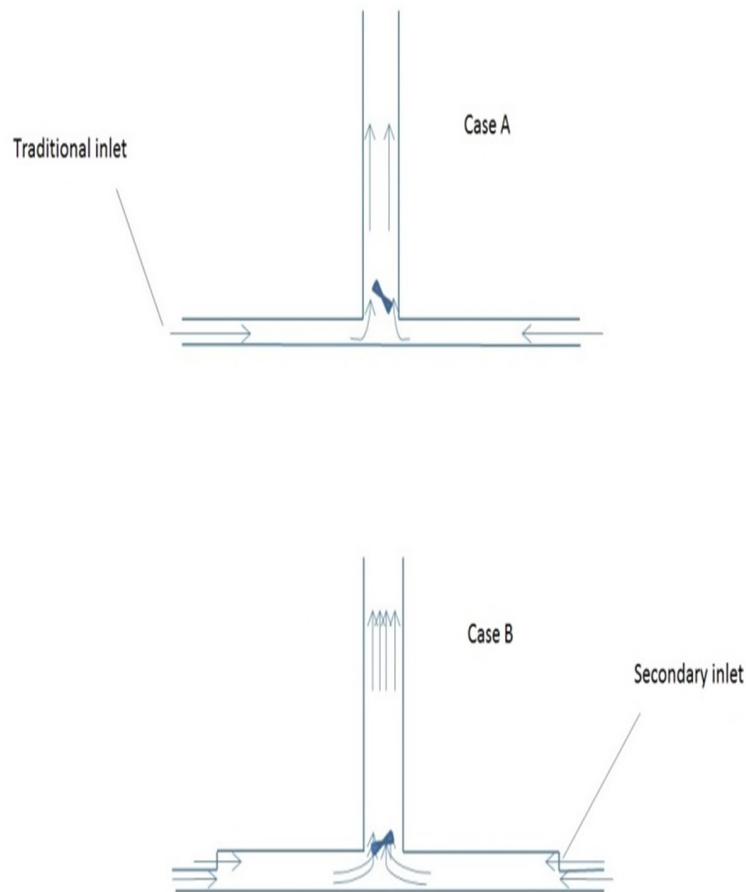


FIGURE 2.2: Schematic case description, traditional collector (Case A), double-inlet collector (Case B)

Manzanares prototype (Fig. 2.3). Numerical analysis was performed for both cases A and B to compare the traditional collector with the double-inlet collector for a range of solar radiation values, which is the available heat flux from the collector ground to air in our model.

To model and simulate the turbulent air flow, $k - \epsilon$ model in the commercial flow solver, ANSYS/FLUENT 17.1, was selected. Steady state axisymmetric computational domain was created (Fig. 2.4). The grid generation tool in ANSYS/Workbench was used to create the mesh in the fluid domain. An unstructured mesh consisting of quadrilaterals cells was generated for the entire domain. With

respect to the sensitivity of pressure value to the air density and buoyancy effect in this model, density was calculated by applying equations of state (EOS).

Computational studies were performed on a 16-core AMD Opteron, 32 Gb Ram workstation. The applied boundary conditions for this axisymmetric model are shown in Fig. 4 as well. CFD calculations were performed with second order formal accuracy for all field variables. The residual convergence tolerance was set not to exceed 10^{-7} . Residuals were observed decreasing gradually with each iteration. The iteration error was calculated for the mass flow rate. In Eq. (2.1) index i represent the i th iteration in the CFD steady state calculation.

$$e_{\dot{m}_i} \equiv \left| \frac{\dot{m}_{converged} - \dot{m}_i}{\dot{m}_{converged}} \right| (2.1)$$

2.4 Analytical Approach

Recently comparative analytical modeling of a traditional collector of SCPP with available experimental values was performed [18]. To calculate the pressure difference generated at the collector and tower, we used the modified version of the above-mentioned analytical model. This analytical correlation uses a one-dimensional approach to mass, momentum and energy conservation equations. Air density was assumed to be related to pressure and temperature via EOS.

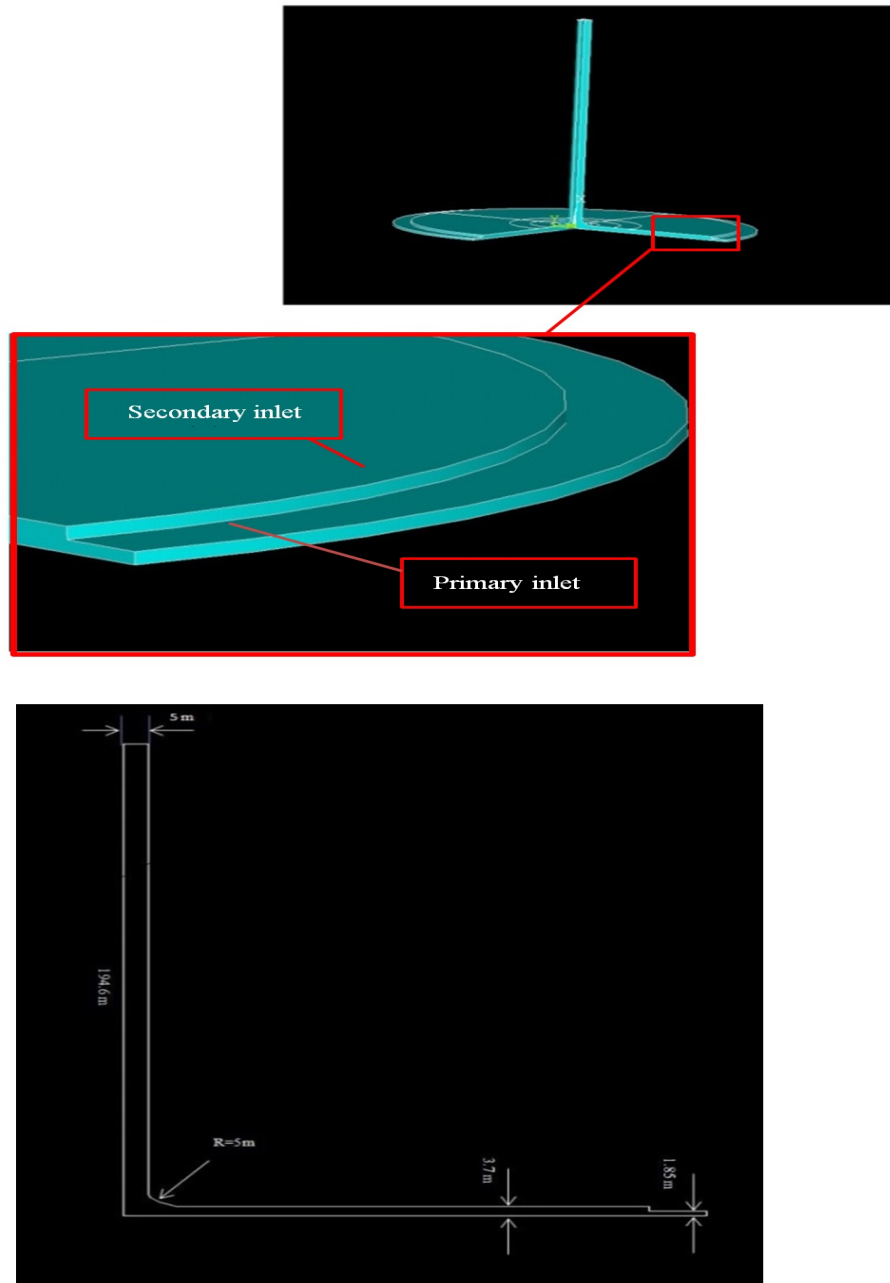


FIGURE 2.3: Case B model details

2.4.1 Collector

Solar Chimney Power Plants provide a reliable and conceptually straightforward way of energy generation from the solar irradiation[14, 17]. A solar collector is the main and only component of this power plant to accumulate the available solar

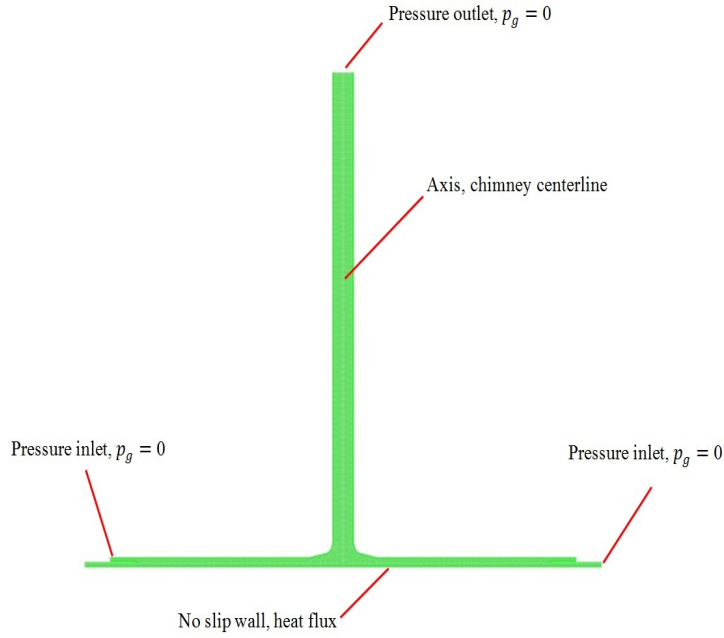


FIGURE 2.4: Computational domain of case B with the applied boundary conditions

energy to heat up air in a greenhouse. The air escapes the collector through a tall chimney which connects the warm air flow of the collector with the cooler air above the ground. The temperature difference induces the natural convection, and turbine at the outlet of collector harvests the energy of the air flow. To model the collector, the simplified one dimensional mathematical analysis was performed to clarify the details. The analytical correlation will be applied later to compare the CFD results against it. To derive the equations, we start from the collector. It is assumed that the flow through the collector is one-dimensional, steady-state, and compressible. Let us disregard the friction and assume the total heat from the solar irradiation is absorbed within the air filling the collector. For this thermal-fluid analysis, the mass conservation satisfies:

$$\frac{dA}{A} + \frac{d\rho}{\rho} + \frac{du}{u} = 0 \quad (\text{Continuity}) \quad (2.2)$$

$$dp + \rho u du = 0 \quad (\text{Momentum}) \quad (2.3)$$

$$c_p dT - dq + u du = 0 \quad (\text{Energy}) \quad (2.4)$$

$$dp = d(\rho RT) \quad (\text{EOS}) \quad (2.5)$$

Let \dot{m} be the total mass flow rate combined from the first (\dot{m}_{i_1}) and secondary inlet (\dot{m}_{i_2}). The mass flow rate of the second inlet, \dot{m}_{i_2} , can be a function of the atmospheric velocity boundary layer which is defined as,

$$\dot{m}_{i_2} = 2\pi r (h_{c,i_2} - h_{c,i_1}) u_{i_2} \quad (2.6)$$

$$u_{i_2} = u_{ref} \left(\frac{h_{c,i_2}}{h_{ref}} \right)^\alpha \quad (2.7)$$

where u_{ref} is the wind velocity measured at h_{ref} which is considered as the reference wind velocity value, and α is the wind shear exponent that can be calculated for small height differences as $\alpha = 1/\ln(h_{ref}/h)$. However, in our calculations we considered the mass flow rate ratio, $\dot{m}_{i_2}/\dot{m}_{i_1}$ based on numerical results. The

pressure drop correlations that were obtained for the collector and tower by considering the average value for c_p of air, and considering the average dimensional and field values for the collector _{i_1} and collector _{i_2} are as follows.

Collector pressure difference:

$$p_{c,o} - p_{c,i} \simeq \left[\frac{\dot{m}^2}{2\rho_{m,c}} \left(\frac{1}{A_{c,i}^2} - \frac{1}{A_{c,o}^2} \right) + \frac{q'' \dot{m}}{2\pi h_c^2 c_p \rho_{m,c} T_{m,c}} \ln \frac{r_{c,i}}{r_{c,o}} \right] \quad (2.8)$$

Tower pressure difference for Manzanares case:

$$p_{t,o} - p_{t,i} \simeq -\rho_{m,t} g h_t \quad (2.9)$$

where $\rho_{m,c} - \rho_{m,t}$ are calculated by the average density values of air at inlet and outlet of collector and tower, by using Boussinesque approximation and lapse rate temperature change respectively. The ideal available power for the turbine is defined as

$$\dot{W} \simeq \frac{\dot{m}(p_{c,o} - p_{t,i})}{\rho_{turb}} \quad (2.10)$$

To calculate the turbine power for available pressure difference, the collector efficiency η_c was considered in our calculation as 0.32 based on reported values from Manzanares prototype.

$$P_t = \eta_c \dot{W} \quad (2.11)$$

2.4.2 Experimental Procedure

To have a better understanding of SCPPS, and also benchmark our numerical results, an experimental study was conducted at a laboratory scale. Particle image velocimetry (PIV) was used to visualize and measure the velocity flow field in a small prototype (1/1000 scale of Manzanares prototype). The CFD analysis was performed for the laboratory prototype as well, for both types of collectors, traditional collector and the double-inlet collector. Fig. 2.5 shows the laboratory experimental arrangement.

A sensitive hotplate (1% K) was used to create the temperature gradient underneath the collector plate (70C for this experiment). The collector roof in the experimental model is height-adjustable via four aluminum legs attached to the edge of the collector plate. Fig. 2.6 shows the experimental apparatus, including the hot plate, chimney, camera, and laser and optical tools.

The flow field was illuminated with a Quantel Evergreen double-pulsed Nd:YAG laser (532 nm), operating at a frequency of 15 Hz, and the laser plane was oriented parallel to the collector, 3.96 mm above the hotplate. Images were taken using a LaVision SCMOS four-megapixel camera, located 0.762 m directly above the model. The entire setup including the hotplate, chimney, camera, and laser, were enclosed in a cage made of PVC pipe and 3 mm thick plastic sheeting. This was done to contain the glycol tracer particles in a large volume around the model.

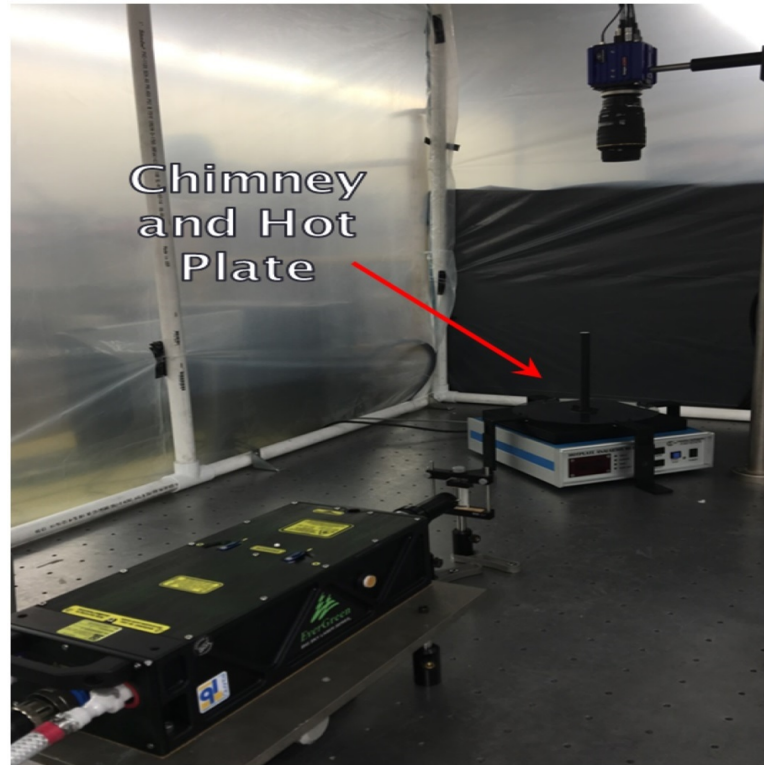


FIGURE 2.5: PIV SCPPS apparatus

2.5 Results and Discussion

CFD simulations were performed for both cases A and B for a range of heat flux at the collector ground. Steady state numerical calculation was performed for both cases in an axisymmetric computational domain. To study the effect of available heat flux from the collector ground to the air on different field variables including temperature, density, pressure, and velocity, several calculations were performed for solar heat flux values q'' of 400-1000 Wm^2 . All calculations were performed with second-order formal accuracy for all field variables. As mentioned before, for all mass, momentum and energy solutions, the residual convergence tolerance was set not to exceed 10^{-7} . As defined before, outlet mass flow rate is selected to calculate the iteration error values. The maximum relative iteration error, e_{m_i} , is

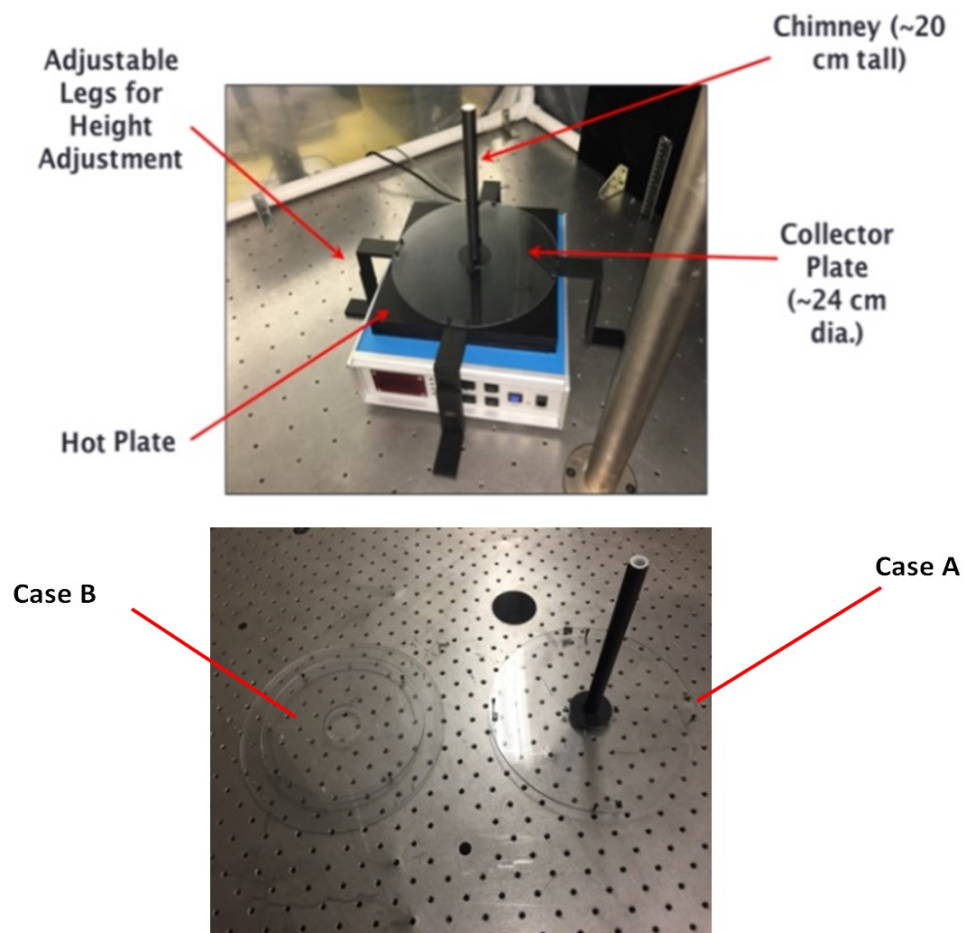


FIGURE 2.6: Collector and hot plate arrangement, two types of used collector in the experimental analysis

8.210^{-7} %. To study field variables quantitatively in the domain of SCPPS and perform post processing we obtained results in three regions (Fig. 2.7).

Air velocity in the collector is a function of its buoyancy and the geometry of the tower/collector. The driven buoyant air rotates the turbine which, in the majority of designs for SCPPS, is placed at the interface of the collector and tower (Fig. 2.7). Buoyant driven air velocity was captured along the collector from the spacing between two inlets until the axis of tower. In many articles, the reported velocity values are not a function of radiation or available heat flux at the collector. However, in our analysis the maximum velocity was obtained for

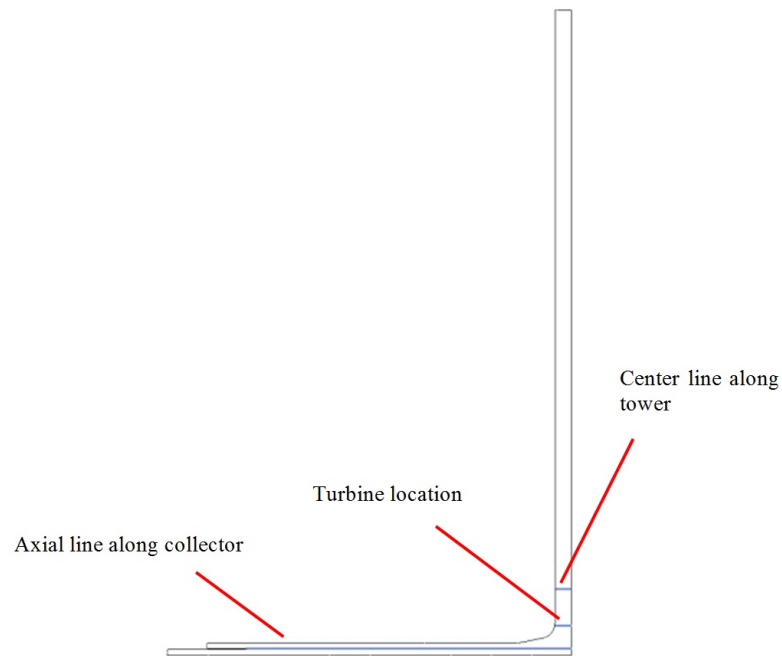


FIGURE 2.7: Location of probes for post processing

1000 W/m^2 and the minimum is for 400 W/m^2 (Fig. 2.8).

As shown in Fig. 4.8, the air velocity increases along the collector until reaching the chimney/tower interface. The maximum velocity is not at the axis due to the curve at the interface of the collector/tower and change of the air flow direction. However, along the tower the fully developed velocity is observed at a 20 m height (Fig. 2.9). As shown in Fig. 2.9 maximum velocity in all velocity profiles at this location for different heat flux values are located at the axis, $r = 0$.

As mentioned above, change of density plays a key role in this renewable power plant system. The density distribution along the collector is presented in Fig. 2.10. Maximum density is at the inlet collector location and minimum density occurs at the axis and the centerline of the collector. As it is apparent from Fig. 2.10, increasing in the heat flux leads to increase in the density variation along the

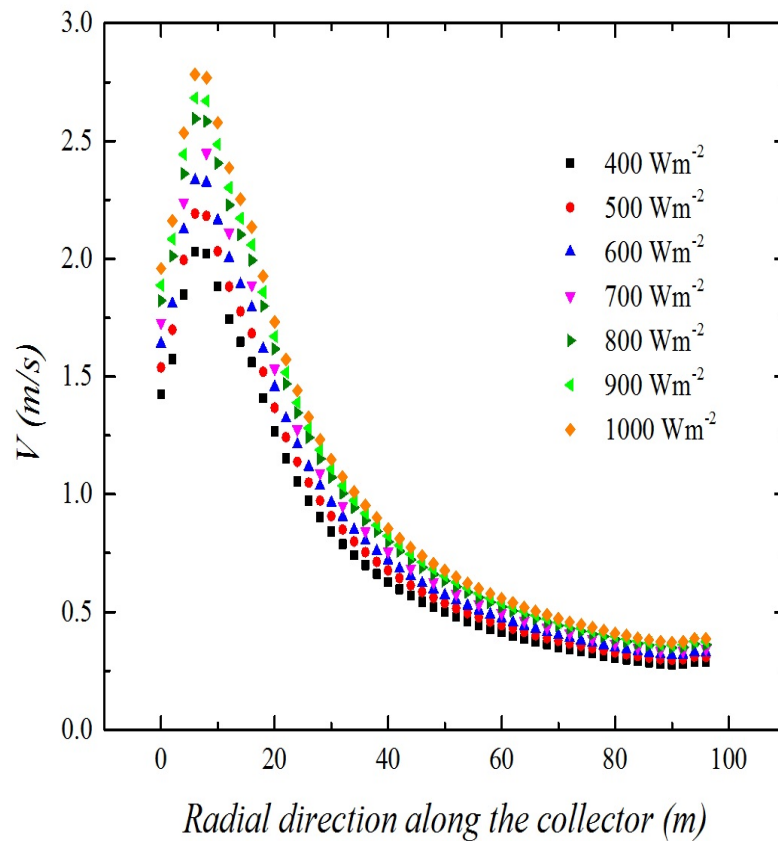


FIGURE 2.8: Velocity distribution along the collector for different heat flux values

collector. The evolution of pressure reduction due to density reduction is shown in Fig. 2.11.

In simulations pressure gauges were set to zero, and we just observe the effect of buoyancy effect to drive the flow, and have flow from upstream to downstream, which is the collector center. The total pressure as the sum of dynamic and static pressure is zero along the collector, leading to negative values for static pressure in the plot. Comparing this simulation with reality, we must note that we are ignoring the stack effect by setting the outlet pressure to zero as well.

Fig. 2.12 shows the temperature behavior along the collector probe line for different heat flux values. The maximum temperature for each profile occurs at

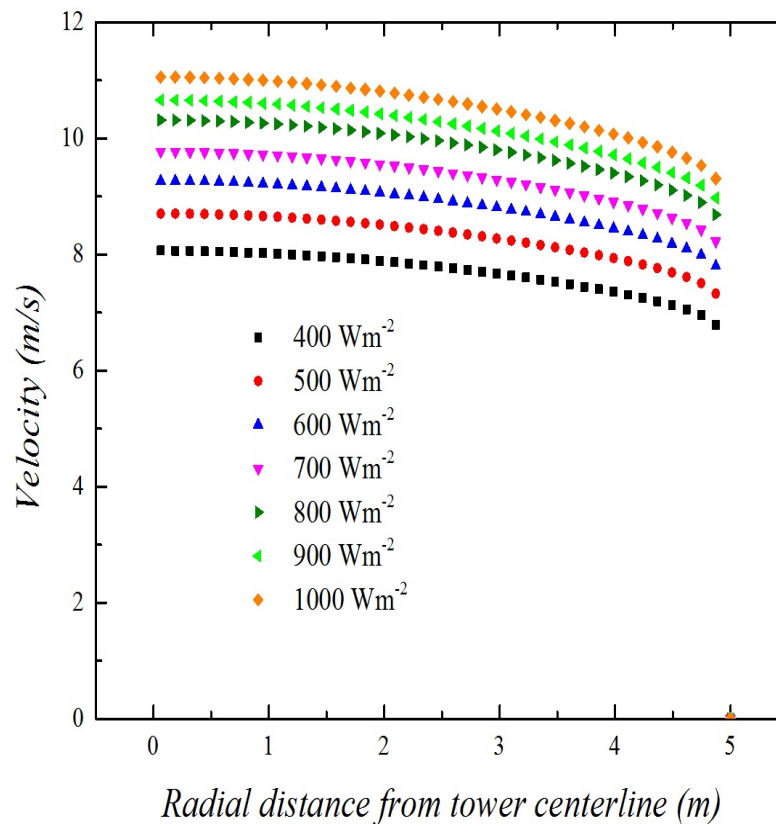


FIGURE 2.9: Velocity profile at 20 m of tower

the center zone of the collector: the bulk of air has achieved the maximum heat from the ground by passing through the collector which leads to the occurrence of the minimum density as shown in Fig. 2.10.

To calculate the available output power of SSCP, the velocity at the turbine location was considered. As shown in Fig. 2.13, the velocity profile is not fully developed yet. However, the maximum velocity occurs at the edge of turbine blades. The maximum available power based on the kinetic energy of air flow is $0.5\rho u^2$. To have a more realistic approach we considered the reported turbine efficiency (85%) and calculated 2/3 of the remained energy. In the case of an enclosed turbine, it is a conservative estimate which can also be considered to account for internal turbine conversion losses.

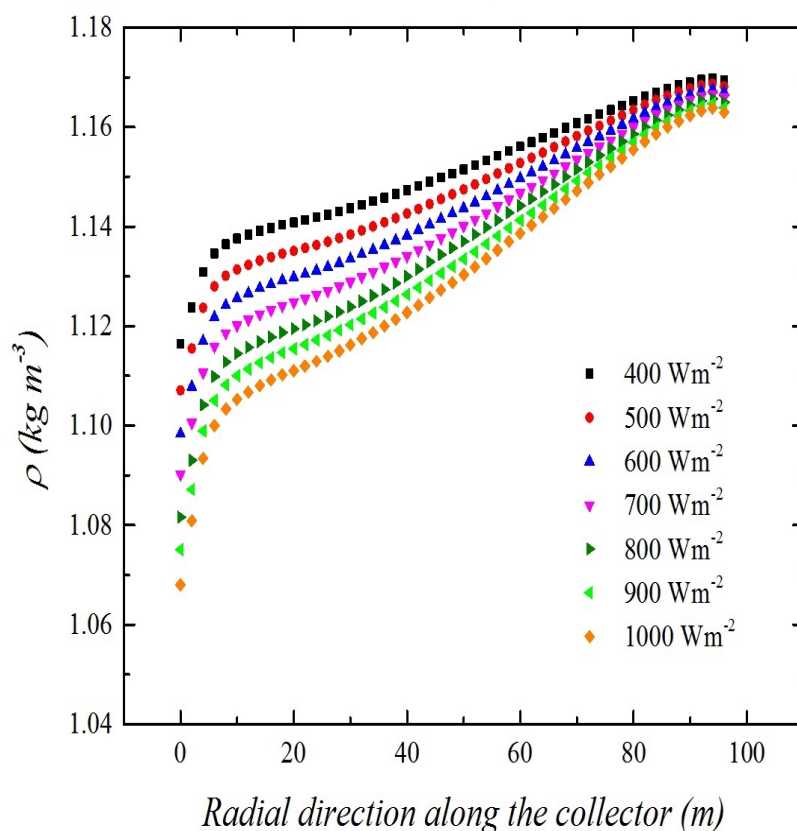


FIGURE 2.10: Density distribution along the collector

The output power from case B was calculated from CFD results and analytical correlations (Fig. 2.14). It appears that for double-inlet collector the output power increases about 14% in comparison with single-inlet. As heat flux increases, we observe reduction in power increase in case B (double-inlet collector) due to the air back-flow/return from the collector to ambient condition. Return mass flow increases after 800 W/m^2 due to the greater temperature difference of air inside of the collector close to the inlet zone and the ambient temperature.

It is obtained that the characteristics of double-inlet SCPPS is not the same as single-inlet and back flow occurs for a lower heat flux. Analytical approach for case B gives us higher power output due to ignoring the back-flow effect, and several simplifications in this one-dimensional analysis, including using average values for

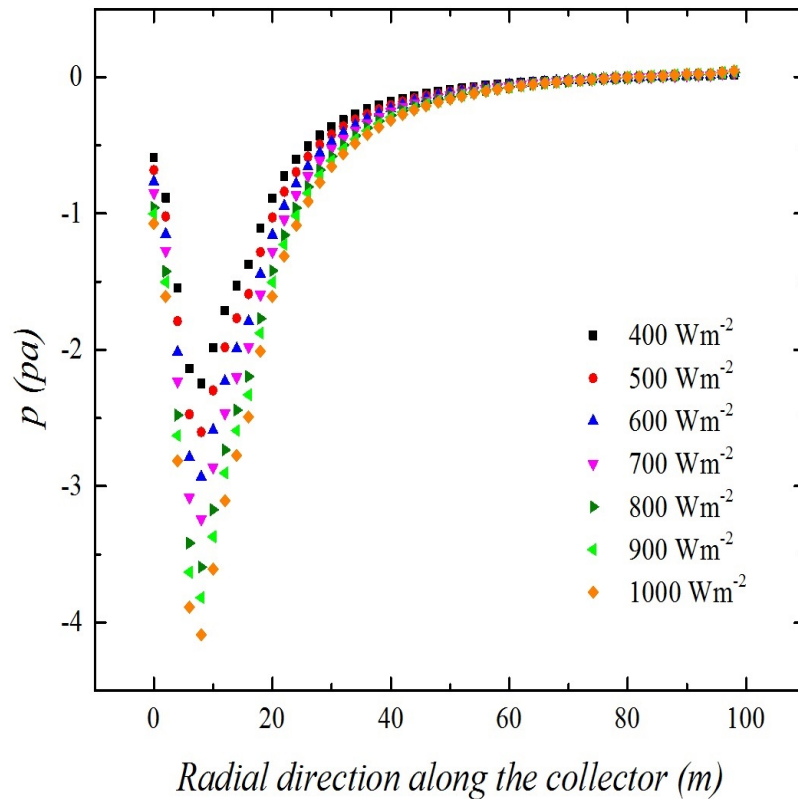


FIGURE 2.11: Pressure evolution along the collector

density, temperature. Also in the analytical-correlation the friction is neglected in the derived PDEs. However, we have considered the same collector efficiency factor to have a more realistic approach in our analytical model. To evaluate our numerical analysis more quantitatively, a small modular SCPPS was fabricated to perform PIV measurements. Hot plate plays the same role as irradiated collector ground which provides heat to the air and generates buoyancy-driven air flow. The velocity field was evaluated and measured to calculate the total mass flow rate and the updraft velocity. Mass flow rate and therefore average updraft velocity is the system response quantity (SRQ) in our validation analysis. Several experiments were performed for different cases; however, in this article we are presenting the results for the single inlet collector validation metric analysis. Fig. 2.15 presents

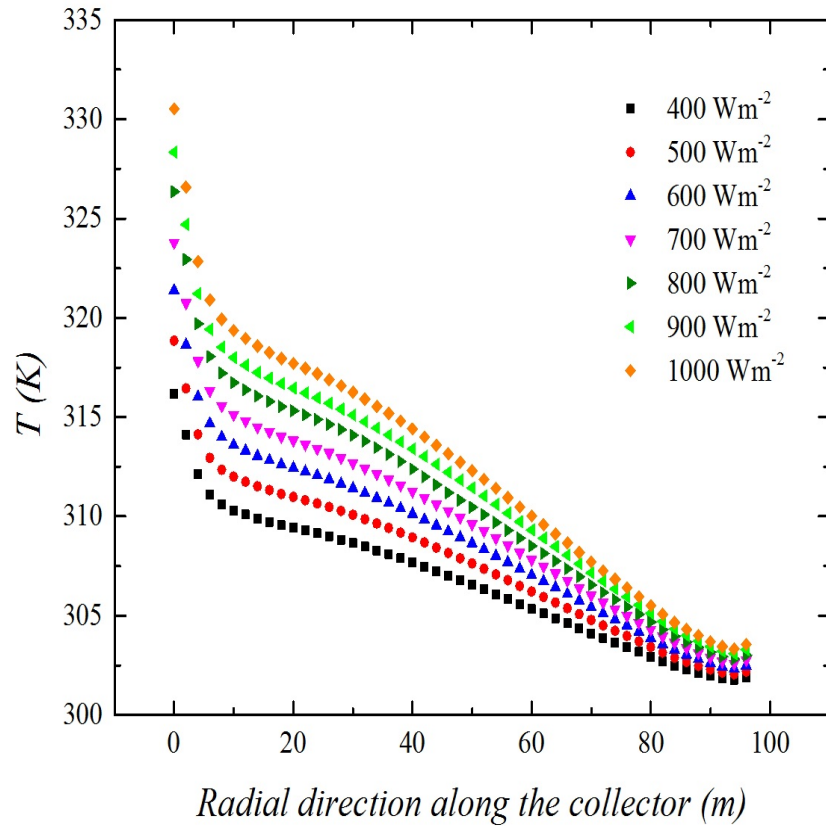


FIGURE 2.12: Temperature distribution along the collector

the region of interest to measure the velocity in the small SCPPS. Several simulations were performed for this prototype similarly to the large-scale, Manzanares system. The epistemic uncertainty of the applied grids was quantified by GCI study as a part of our solution verification.

The iteration error was 100 times smaller than grid uncertainty and we did not include them in our error uncertainty calculation. To perform validation, error is defined as, $E = S - D$ [19]. The experimental data was considered as the reference of error. However, the uncertainty of error includes the uncertainty of the simulation based on epistemic uncertainty observed by solution verification. Validation model assessment was performed by using modified area validation metric [20, 21].

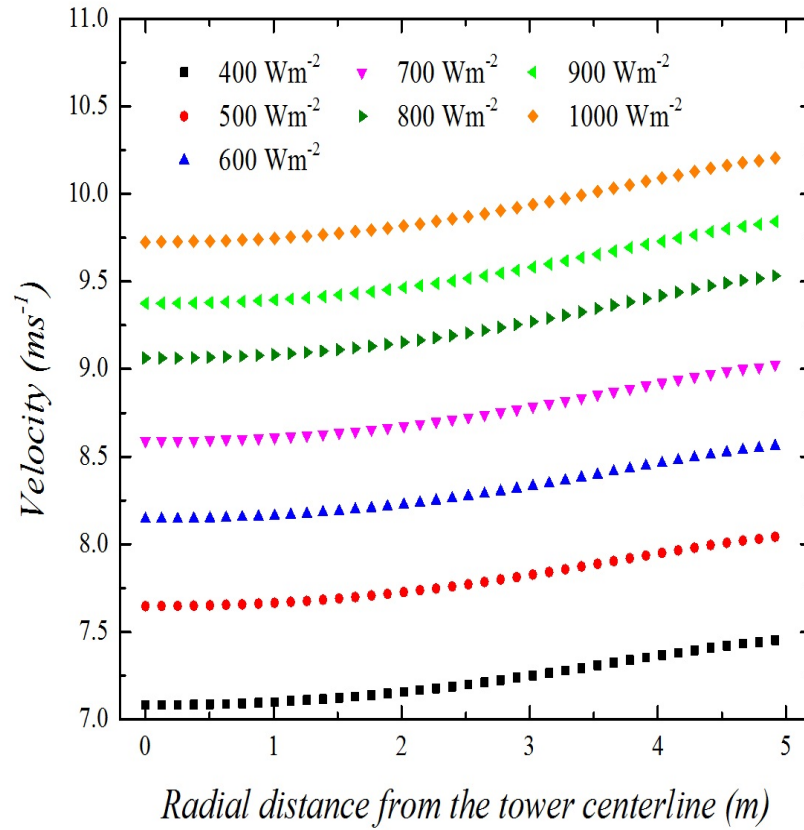


FIGURE 2.13: Velocity distribution at the turbine location

The cumulative and empirical probabilities of the system of response quantity from experimental measurements and from simulation results were observed. The quantitative mismatch of cumulative distribution of experimental data and empirical distribution function (EDF) of simulation results of SRQ, which called validation metric area (d), were calculated. Fig. 2.16 is the EDF/CDF representation of cumulative experimental and numerical results.

The colored areas are the mismatch of experimental and simulation cumulative values. Red area presents the positive mismatch (d^+) and blue area presents the negative mismatch (d^-) which is counted to calculate the model error uncertainty, u_{model} . The validation standard uncertainty, u_{val} , which is defined as the summation of all uncertainties as input uncertainties and experimental uncertainties.

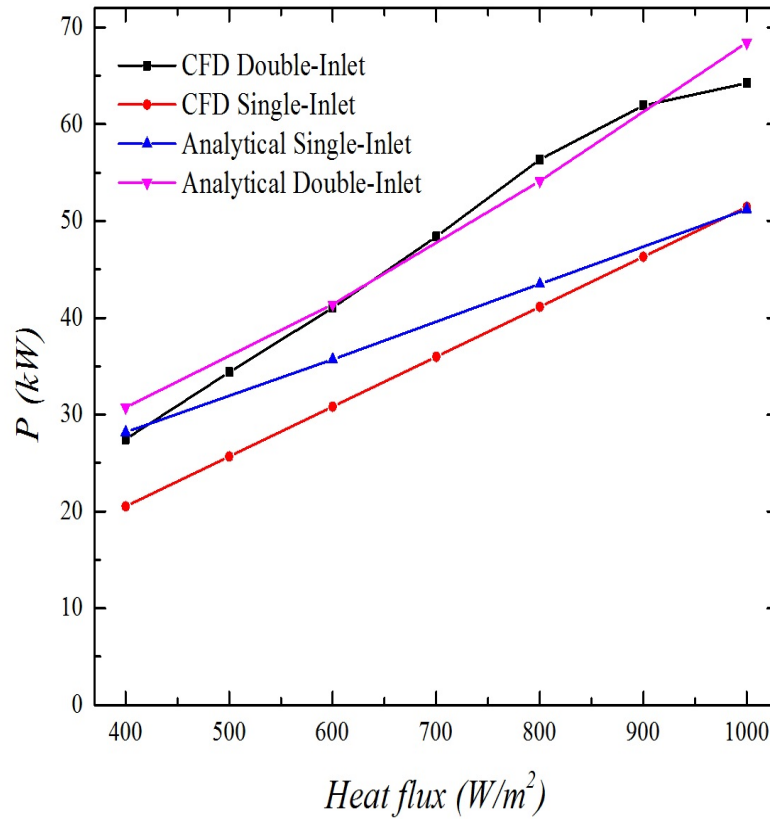


FIGURE 2.14: Output power for different cases

In our analysis, we have just considered u_{model} and did not have values for the other uncertainties. Therefore, the validation standard uncertainty u_{val} in our simulation is the same as u_{model} . The validation metric which is E and u_{val} can be correlated by using a factor of safety and define an interval which u_{val} falls in with a defined confidence level. The chosen confidence level based on reported V&V20 standards is 95%.

$$u_{model} = [S - F_s d^-, S + F_s d^+] = [8.15, 10.3] mm/s \quad (2.12)$$

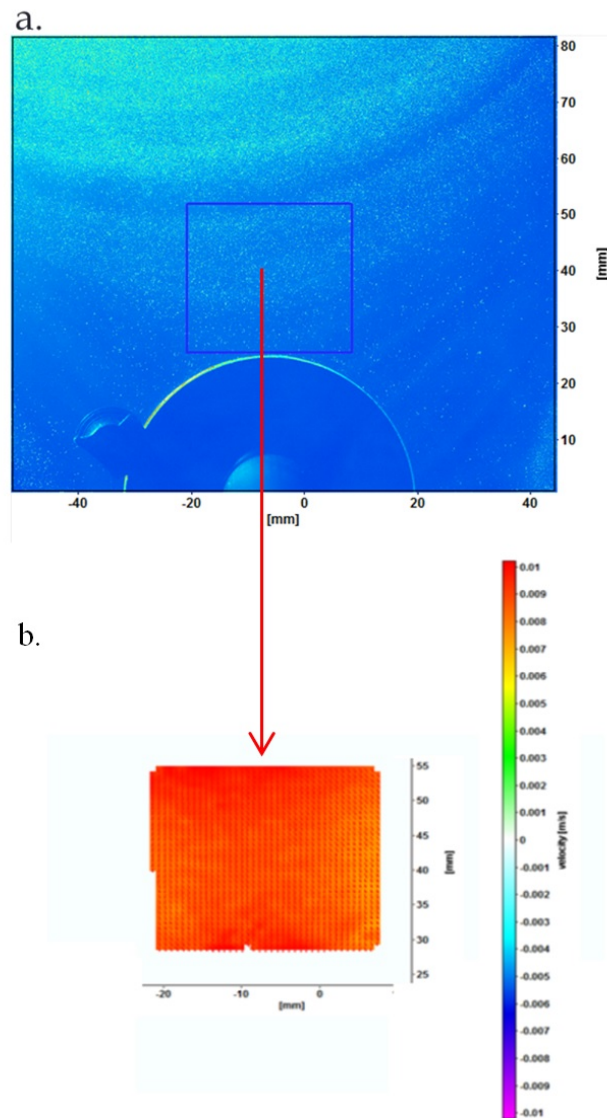


FIGURE 2.15: Experimental region of interest, blue Square (a) and averaged velocity vector/contour plot of the area of interest (b)

2.6 Conclusion

Double-inlet collector design for SCPPS was presented and evaluated against the traditional collector design. Computational analysis for different cases was conducted to evaluate this idea. For Manzanares prototype applying double-inlet collector design increases the overall efficiency up to 14%. One-dimensional analytical study for double-inlet collector also was conducted and compared against

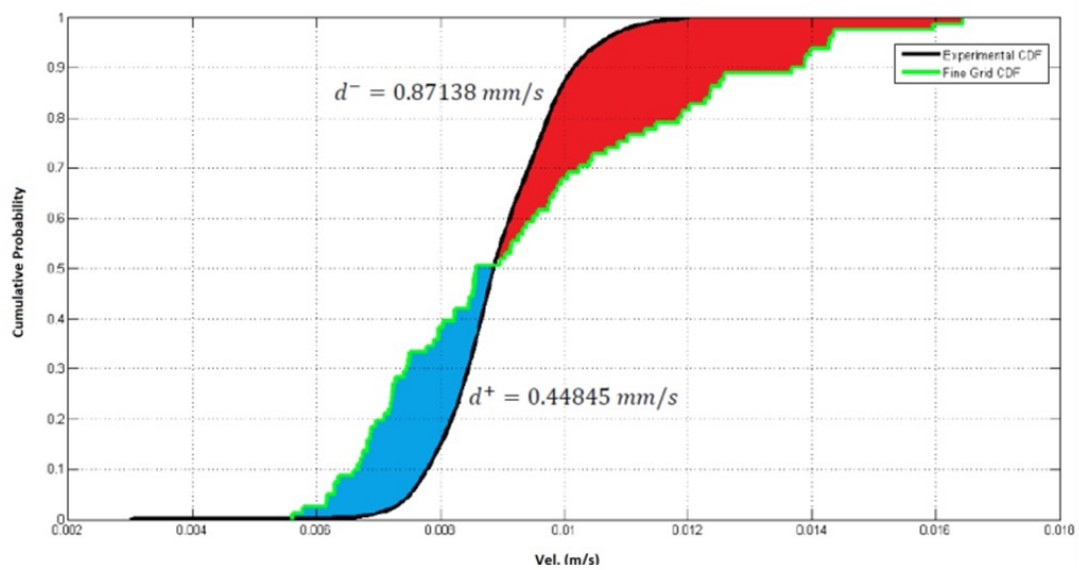


FIGURE 2.16: Cumulative probability of D and S, area metric validation representation

the CFD results for traditional and the proposed design. In the analytical study with respect to ignoring the backflow effect, the agreement of results decreases by increasing the available heat flux. PIV analysis was performed to have a better understanding on SCPPS air flow for a smaller prototype. Validation metric study was performed for this prototype to evaluate the fidelity our CFD model. The validation standard uncertainty of model was obtained for the smaller prototype.

Bibliography

References

- [1] Crabtree, George W., and Nathan S. Lewis. "Solar energy conversion." *Physics today* 60, no. 3 (2007): 37-42.
- [2] Haaf, W., K. Friedrich, G. Mayr, and J. Schlaich. "Solar chimneys part I: principle and construction of the pilot plant in Manzanares." *International Journal of Solar Energy* 2, no. 1 (1983): 3-20.
- [3] Bernardes, MA dos S., A. Voß, and G. Weinrebe. "Thermal and technical analyses of solar chimneys." *Solar Energy* 75, no. 6 (2003): 511-524.
- [4] Bonnelle, Denis. "Solar chimney, water spraying energy tower, and linked renewable energy conversion devices: presentation, criticism and proposals." PhD, University Claude Bernard-Lyon (2004).
- [5] dos Santos Bernardes, Marco Aurelio, Ramon Molina Valle, and Márcio Fonte-Boa Cortez. "Numerical analysis of natural laminar convection in a radial solar heater." *International journal of thermal sciences* 38, no. 1 (1999): 42-50.

- [6] Schlaich, Jorg, Rudolf Bergemann, Wolfgang Schiel, and Gerhard Weinreb. "Design of commercial solar updraft tower systems—utilization of solar induced convective flows for power generation." *Journal of Solar Energy Engineering* 127, no. 1 (2005): 117-124.
- [7] Fathi, Nima, Patrick Mckdaniel, Seyed Sobhan Aleyasin, , Matthew Robinson, Peter Vorobieff, Salvador Rodriguez, and Cassiano de Oliveira. "Improving the Efficiency of the Solar Chimney Power Plant by Use of Waste Heat from Power Plants (Nuclear and Conventional)." *Journal of Cleaner Production* (2017).
- [8] Pretorius, Johannes Petrus. "Optimization and control of a large-scale solar chimney power plant." PhD diss., Stellenbosch: University of Stellenbosch, 2007.
- [9] Betz, Albert. *Introduction to the theory of flow machines*. Elsevier, 1966.
- [10] Pasumarthi, N., and S. A. Sherif. "Experimental and theoretical performance of a demonstration solar chimney model—Part I: mathematical model development." *International Journal of Energy Research* 22, no. 3 (1998): 277-288.
- [11] P. Vorobieff, A. Mammoli, N. Fathi, V. Putkaradze , "Free-standing inflatable solar chimney: experiment and theory," *American Physical Society Division of Fluid Dynamics*, San Francisco, CA, 2014.
- [12] Putkaradze, Vakhtang, Peter Vorobieff, Andrea Mammoli, and Nima Fathi. "Inflatable free-standing flexible solar towers." *Solar Energy* 98 (2013): 85-98.

- [13] Schlaich, Jörg. The solar chimney: electricity from the sun. Edition Axel Menges, 1995.
- [14] Fluri, T. P., and T. W. Von Backström. "Performance analysis of the power conversion unit of a solar chimney power plant." *Solar Energy* 82, no. 11 (2008): 999-1008.
- [15] Denantes, F., and E. Bilgen. "Counter-rotating turbines for solar chimney power plants." *Renewable energy* 31, no. 12 (2006): 1873-1891.
- [16] Fluri, T. P., and T. W. Von Backström. "Comparison of modelling approaches and layouts for solar chimney turbines." *Solar Energy* 82, no. 3 (2008): 239-246.
- [17] "Annular Flow Convection Chimney (AFCC), Multi Inlet Solar Thermal Array Collector-Tower" Nima Fathi, Peter Vorobieff, Seyed Sobhan Aleyasin and Andrea Mammoli . (2015) Flintbox.
<http://www.flintbox.com/public/project/29725/>
- [18] Fathi, Nima, Seyed Sobhan Aleyasin, and Peter Vorobieff. "Numerical-analytical assessment on Manzanares prototype." *Applied Thermal Engineering* 102 (2016): 243-250.
- [19] Oberkampf, William L., and Christopher J. Roy. *Verification and validation in scientific computing*. Cambridge University Press, 2010.
- [20] Voyles, Ian T., and Christopher J. Roy. "Evaluation of model validation techniques in the presence of aleatory and epistemic input uncertainties." In *17th AIAA Non-Deterministic Approaches Conference*, p. 1374. 2015.

- [21] Voyles, Ian T., and Christopher J. Roy. "Evaluation of Model Validation Techniques in the Presence of Uncertainty." In 16th AIAA Non-Deterministic Approaches Conference, p. 0120. 2014.

Chapter 3

Inflatable Free-Standing Solar Chimney Power Plants¹

We propose a novel design for a solar updraft tower, wherein the chimney that generates the updraft is a self-supporting, free-standing stack of hollow gas-filled tori. Considerations for the design stabilizing the structure via a combination of shape, overpressure, and buoyancy are presented. Filling the tori with air rather than with a light gas may be advantageous for stability. The chimney shapes are optimized for deformation under wind loading. We also present simple cost calculations and results of CFD modeling to confirm the viability of the design.

Variables.

A cross-section of the torus exposed to the wind

A_c horizontal cross-sectional area of the chimney

¹Originally published as: Putkaradze, Vakhtang, Peter Vorobieff, Andrea Mammoli, and Nima Fathi. "Inflatable free-standing flexible solar towers." *Solar Energy* 98 (2013): 85-98.

C_d	drag coefficient of the torus
F	force on the torus
f	dimensional factor incorporating drag coefficient introduced in Eq. 7
g	acceleration due to gravity
h	vertical deformation of the torus
M	molar mass
N_{el}	estimate of turbine output power in solar chimney
\dot{m}	mass flow rate of air through the chimney
p	absolute excess pressure in the torus
P	relative excess pressure in the torus
P_{max}	maximum turbine power
q	major radius of torus
r	minor radius of torus
R	gas constant
s	direction of the torque
S	representative area due to torus deformation
T	torque on the torus (Section 3.3); absolute temperature (Section 3.5)
U	average wind velocity at a given altitude
\bar{u}	average vertical velocity inside the chimney
V	scaled wind force (Section 3.3)
\dot{V}	volumetric flow rate (Section 3.5)
z	altitude
ΔH	change in stagnation enthalpy

ΔP_T total (inlet-to-exit) turbine pressure loss

η_{tt} turbine efficiency

μ relative deformation h/r

ϕ torus deflection angle

Subscripts

d downwind direction

k count referring to current torus in stack

u upwind direction

w due to wind

3.1 Introduction

Solar updraft towers (also known as solar chimneys) offer a simple and reliable way of generating electricity from solar radiation [1]. For solar chimneys, the principle of energy production is very simple: a solar collector heats up air in a collector (greenhouse) occupying a large area. The air escapes the collector through a tall (hundreds of meters) pipe, which connects the hot volume of the collector with the cooler air above the ground. The temperature difference induces the convection, and a turbine within the pipe harvests the energy of the updraft.

The advantages of the design are as follows:

1. Unlike most other renewable-energy facilities, the huge thermal mass involved in the design means very low variability of the output, with the possibility of continuous production of dispatchable energy.
2. The only components of the design requiring regular maintenance are the generating turbines located at ground level.
3. The facility does not need a continued supply of water.
4. The facility can be built from a variety of cheap (and locally sourced) materials.

However, despite these unique advantages (especially compared with photovoltaic or wind- turbine systems), there are also significant drawbacks. The key flaw of this design is extremely low efficiency (0.5-5 %) [2]. One of the ways to improve this efficiency would be by enhancing the thermodynamics of the updraft flow, but that requires increasing the temperature differential between the greenhouse on the bottom and the exhaust on top of the updraft tower, which would mean building taller towers. Thus the present state of the art relies on a very tall free-standing updraft chimney to drive the flow. In this paper, we are going to focus on overcoming the difficulty of building the towers of desired height (hundreds of meters) that are sufficiently structurally stable to reliably withstand wind and other atmospheric effects.

An example of a state of the art updraft tower facility is the Jinshawan Tower [3] currently under construction in north China's Inner Mongolia Autonomous Region. The operation of the first stage of the facility started in December 2010, and the full height of the updraft tower will be about 900 m. One of the problems

immediately apparent here is that the taller the tower, the better the efficiency, however, the challenges of building a very tall structure soon begin to outweigh the thermodynamic benefit. Moreover, the costs of erecting the tower soon begin to dominate the overall cost of the facility and increase the levelized electricity cost (LEC) from the tower. For a 100-MW plant, the cost of the chimney already represents about half of the overall cost [4].

The first operational updraft tower prototype [4] built in Manzanares, Spain, had the tower height of 195 meters, with thin iron sheet used for construction. The main cause for the decommissioning of the facility in 1989 [5] was the failure of the tower's guy wires in a storm, which led to the tower collapse. Towers for proposed full-scale facilities, such as the Ciudad Real Torre Solar in Spain [6, 7], are even taller (750 m to 1500 m).

Because of the gigantic scale required for working solar updraft structures, any mistakes in design and construction are likely to be very costly. Thus numerical modeling of chimney/collector systems has attracted understandable recent attention. A study by [8] produces good results in modeling the first operational updraft tower mentioned above [4], using $k - \varepsilon$ turbulence model. In this study, the collector array, the chimney, and the turbine are all included in the model, and the thermophysical properties of the soil under the collector are also taken into account. The size of the structure and the number of factors that have to be taken into consideration make this problem a challenge to model. Modelers are somewhat helped by dimensional analysis of [9] that introduce similarity parameters allowing to scale solar chimney models. The possibility of using a converging

or diverging tower has also been studied numerically by [10], with results directly pertinent to the discussion that follows in the present paper.

Here we propose a design that takes advantage of the attractive features of the solar updraft tower as a concept, yet eliminates the most expensive component of the construction, namely the chimney itself, by replacing it with a lightweight self-supporting construction of stacked gas-filled toroidal shells which is designed to withstand the forces of the wind by optimizing its flexing properties.

3.2 Conceptual design and theoretical considerations

The goal of this paper is to discuss methods of replacing the steel updraft chimney as the most costly and vulnerable part of the design. Several authors have tried to solve this problem by proposing chimneys that implement buoyant elements in their designs and are thus self-supported (see [11–13] or [14] for a recent review of the literature and references). While these ideas are certainly appealing, they have several drawbacks. First, the designs presented in these works repeat the straight cylinder geometry of the steel chimneys; under the wind load, the deformation is concentrated in the elements immediately adjacent to the ground. [14] suggests using an accordion-like structure attaching the tower to the ground; however, under repeated oscillations due to wind this structure will also experience a lot of wear. In addition, the elastic response for the accordion structure is difficult to predict and for very strong winds, the structure may exhibit some undesirable

behavior. Second, due to constant wear of buoyancy-providing bladders due to the deformations of the structure itself, light gas (helium) would leak from bladders, and subsequent loss of buoyancy would present a problem.

All the designs described in earlier works lose stability if they experience loss of helium and thus loss of buoyancy. The buoyancy of floating towers has to be adjusted just right, so the stresses due to the lifting force on the attachment to the ground do not exceed critical values, and at the same time high enough so that the structures preserve the stability of the vertical state in the air. This would require a constant and individually adjusted supply of helium to the bladders, and since helium is becoming expensive, the cost of maintaining the buoyancy in the long term use of these towers must be taken into account. There could be a way to substitute hot air instead of helium, since hot air is in abundance in the greenhouse, but on demand and consistent supply of hot air to the bladders also presents a challenge and adds to the cost. Other lighter than air gases, such as hydrogen and methane, are highly combustible and probably should be avoided for these applications.

The idea of this paper is to suggest an *air-filled* tower that is self-supporting with its shape optimized to take into account the wind pressures, as shown in Fig. 3.1. The tower's rigidity is designed in such a way that the deformation along the tower is controlled. Moreover, since the tower is filled with air, maintaining the desirable pressure in each individual toroidal bladder can be achieved with a simple arrangement of valves and pumps. Such a system could even accommodate the winds that are strongly varying with elevation. Initially we considered toroidal

bladders filled with a lighter-than-air gas, *e.g.*, helium, to support the weight. However, as it turns out, filling these bladders with air is not only highly economical, but allows to solve the issue of tower stability in a much more efficient way. The shape of the tower, chosen to deform in the optimal fashion under the wind, has the additional advantage that the load on each bladder from the weight of the chimney above it is approximately proportional to the size of the bladder itself, and thus extra pressure generated by the supporting weight in each bladder distributed over the respectively larger volumes of the bottom tori will be very small. In addition, there are extra stability advantages achieved by filling the bladders with air, as we discuss in details in Sec. 3.3.3. *All the following considerations will be carried out for air-filled bladders.* While helium-filled bladders and a mixture of air/hot air/helium/etc. can still be used, we believe that the air-based design is the simplest, the most economical, and the most advantageous for stability.

The toroidal bladder may have a rigid structural frame (like a zeppelin) or be semi-rigid (like a blimp). It may be possible to deflate and secure the bladder in the case of extreme weather events. The largest helium-filled airships of the 1930s (USS Acron and Macon) were 240 meters long. A 1000-m tall tower would require merely quadrupling this size, which will be greatly aided both by seventy years of advances in the materials science and by the fact that the lift of the tower would merely have to match its own weight. However, from the point of view of both strength and reliability, as well as stiffness, a design with multiple buoyant compartments (toroidal in shape) is even more attractive (Fig. 3.1). The buoyant gas can be helium (considered in the following section) or even hot air, with a

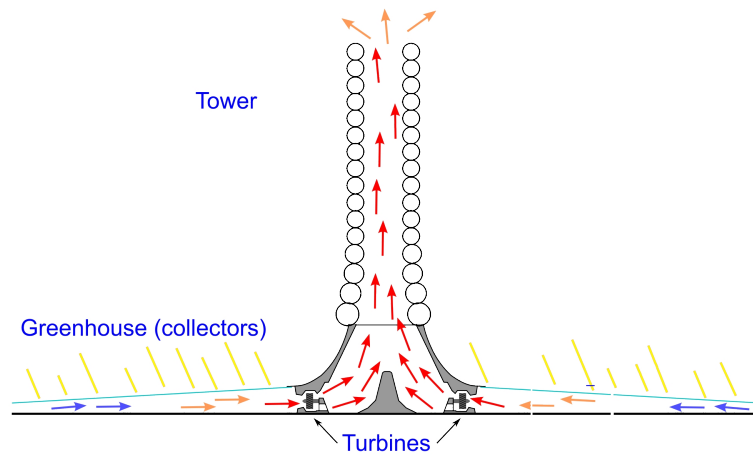


FIGURE 3.1: Schematic of a solar updraft tower facility with a chimney comprised of toroidal bladders.

possibility of using solar-heating for the latter.

There are different ways to optimize the design of the solar chimney itself. It is clear that the main obstacle in designing tall towers is presented by the forces of wind introducing transversal stresses to the construction. These considerations have provided a lot of difficulties for the designers of *rigid* tall structures. Perhaps the most famous example is provided by the celebrated Eiffel tower. To our knowledge, the most detailed and historically accurate paper [15] explores some of the history of the tower, and derives the solution for the tower's shape based on a careful analysis of Eiffel's own ideas. We will briefly mention the results of that paper here, as it is of relevance to our discussions.

Eiffel's considerations, put in modern scientific language, can be summarized as follows. Consider an arbitrary cross-section of the tower perpendicular to its axis. There are support forces acting tangentially to the outer shape, generated by the support beams of each of the tower's elements. These forces should pass exactly through the application point of the force of wind resistance of the part above

that cross-section. That condition eliminates the need of strong diagonal support throughout the tower, thus radically reducing the weight and cost of the tower, and make it more aesthetically appealing by giving it an “airy” look that the Eiffel tower is now renowned for. A nonlinear integro-differential equation for the tower can be derived starting with these arguments, and making some assumptions for the force of wind on an infinitesimal tower element. If it is assumed that the velocity of the wind is constant with height, and the force on an element is proportional to its area, then the solution of this integro-differential equation for the tower shape is exponential. As it turns out, Eiffel was also worried that the coefficient of wind resistance changes from the bottom elements to the top elements of the tower, so to enhance the tower stability, the design eventually included one exponential function at the bottom part of the tower, and another one at the top part of the tower.

Thus, in some sense, the exponential shape is optimal for rigid structures, as it minimizes the torques acting on a given cross-section. Assuming exponential shape is also a possibility for the solar updraft towers. Eiffel’s original design did not take wind loading into consideration. Had a realistic wind-loading profile (unknown during the time of the conception and construction of Eiffel’s tower) been added to his considerations, the shape of the tower would have been a bit different [16]. However, Eiffel’s assertion that his tower profile conforms to the moment distribution due to wind loading is, interestingly enough, proven correct. These advantages of the exponential profile for rigid structures notwithstanding, as the tower in our design is allowed to flex freely, it is worthwhile to explore

other possibilities for its shape. The main difference of our flexible tower and rigid structures is that some flex is not detrimental to our tower's performance; however, a "break" (i.e. a sharp deformation blocking the air flow) in the tower would close the air flow and prevent the tower from operating. Also, a tower which is plagued by consistent breakage of this kind under the wind will wear out prematurely. Thus, the goal of designing the tower structure is to distribute deformations, in some sense, equally along the tower. We will make this statement more precise in the following sections.

3.3 Optimization strategy: prescribed deformation design

3.3.1 Formal problem set-up

Let us now consider a more detailed model and try to eliminate the "break" (*i.e.*, a sharp bend forcing flow blockage) in the tower under the wind force by distributing deformations equally (in some sense) along the tower. To achieve that, we will need to derive a model for deformations. As it turns out, since the tower is assumed to be built out of tori, the contact forces are non-linear, and cannot be linearized by any method. Therefore, the model is radically different from that of a tower that can be modeled as a continuous structure, and Eiffel's considerations do not apply here.

The force between two tori Let us consider two tori in contact, for example, the tori numbered k and $k + 1$. These tori have small radii r_k and r_{k+1} in contact correspondingly. Let h_k and h_{k+1} be the maximum normal deformations of the k -th and $k + 1$ -st torus. Assume that the excessive pressure inside these tori is p_k and p_{k+1} and the deformations are small, so the total volume and pressure change of each torus is negligible. To the first approximation, one can assume that the area changes linearly away from the maximum contact.

The typical width of the contact area of torus k and $k + 1$ on the side of k -th torus is given by $\sqrt{2r_k h_k}$. The total area of the shaded, sickle-like contact area for the torus k , as illustrated in Fig. 3.2, can be estimated by multiplying half of the perimeter of k -th torus exposed to the deformation πq_k by the typical contact width $\sqrt{r_k h_k}$ (ignoring the pre-factor, see below), to give

$$S_k \simeq \pi q_k \sqrt{r_k h_k}. \quad (3.1)$$

Note that this is simply an estimate, the detailed dimensions of sickle-like shape depending on many factors. For example, the way adjacent tori are attached to each other and whether vertical gaps between tori are allowed in the upwind direction will influence the dimensionless pre factor in that expression. However, the important feature is the square root singularity, which will be discussed immediately below.

Technically, there is a factor of an order 1 in Eq. (3.1) that takes into account unequal forces along the torus: they are higher at the maximum deformation

point and diminish away from it, resulting in the sickle-like shape of deformation as shown in Fig. 3.2. This pre-factor also incorporates $\sqrt{2}$ from the typical width of the sickle-like area. However, this pre-factor can be incorporated into the dimensionless parameter V introduced below

Suppose we define the tilt of the k -th torus *with respect to the vertical* to be ϕ_k . A sketch of the tori in contact is shown in Fig. 3.2. Then, in the most basic approximation, assuming the tori were in contact initially, the deformation of the torus at contact is computed by the change of coordinates of the torus and its neighbors. Since the deformations are caused by the wind, we will assume that the wind direction is from the right, and denote the variables as being “upwind” (subscript u) and “downwind” (subscript d). Assuming that the angle is computed as positive counter-clockwise and remains small, the deformations are given by the formulas:

$$h_{k,u} = |q_k\phi_k - q_{k-1}\phi_{k-1}|, \quad h_{k,d} = |q_{k+1}\phi_{k+1} - q_k\phi_k|. \quad (3.2)$$

Notice that $h_{k+1,u} = h_{k,d}$, coming from the fact that the tori are attached so they keep continuous, persistent contact throughout their perimeter at all times. If one connects these tori with, for example, elastic springs, that formula would not be accurate. The deformation $h_{k,u}$ (and similarly $h_{k,d}$) consists of two parts: the positive part contributed by the tilt of the k -th torus, assuming the positive angle is measured counterclockwise, and negative shift of the $k - 1$ -st torus. The absolute value sign accounts for cases when the deformation happens on the upwind or

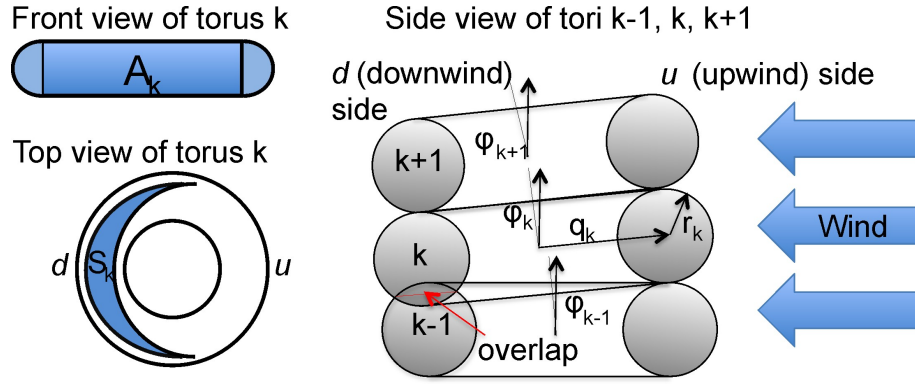


FIGURE 3.2: Tori $k - 1$, k and $k + 1$ in contact. Top left: front (windward) view. The toroidal cross-section (area A_k) exposed to the wind is a combination of a rectangle and two half-circles. Bottom left: top view. The contact area S_k between two tori caused by the wind deformation is shown. Right: side view.

downwind part of the tower. For static configurations considered in this paper, the compressed area is always on the downwind side. However, the absolute value in (3.2) becomes important for modeling the dynamics of the tower, which will be considered in future works.

Equilibrium conditions The net torque acting on the k -th torus computed with respect to its center is thus

$T_k = q_k \times F_k$, where the applied force F_k is computed from $F_k = S_k p_k$, the deformed area times excessive pressure in the k -th torus. From Eq. (3.1), we obtain

$$T_k = q_k p_k \cdot \pi q_k \cdot (s_k \sqrt{2r_k |h_{k,d}|} - s_{k+1} \sqrt{2r_k |h_{k,u}|}). \quad (3.3)$$

The sign convention assumes that the downwind part of the deformation generates clockwise torque, as shown in Fig. 3.3, taken with the positive sign. Here p_k is the excess pressure in the k -th torus. The factors $s_k = \text{sign}(\phi_k - \phi_{k-1})$ define the direction of the torque. Indeed, if the local relative tilt of the tower changes the

direction, the contact area shifts from the upwind to downwind part of the torus, *i.e.* the darkened sickle-like contact shape on the left of Fig. 3.2 abruptly shifts to the other side of the torus, contributing to the change of sign in the torque expression T_k . For steady states of equally pressurized tori ($p_k = P = \text{const}$) that we considered below, the angles ϕ_k can be assumed to be monotonically increasing, so $s_k = 1$. However, these coefficients will become important for the questions of dynamics and control of the tower, which we will address in future works.

This torque defined by Eq. (3.3) has to balance the torque due to the wind acting on all the tori above the k -th torus. The cross-section of the torus exposed to the wind is

$A_k = r_k(\pi r_k + 2q_k) \cos \phi_k$. Then, the magnitude of the force on the i -th element is computed as

$$F_i = C_d U_i^2 A_i \cos \phi_i \simeq C_d U_i^2 r_i (\pi r_i + 2q_i) \cos \phi_i, \quad (3.4)$$

where U_i is the average wind velocity acting at the elevation z_k and, correspondingly, R_i is the Reynolds number of the i -th torus. Here, C_d is, for simplicity, assumed to be the drag coefficient of a single torus which is typically of order 1 for large values of properly defined Reynolds numbers. We can define, for example, $R_i = U_i \sqrt{q_i r_i} / \nu$, although other definitions of Reynolds number are possible as well. Then the torque due to wind resistance (as denoted by subscript w) above the k -th torus is

$$T_{k,w} = \sum_{i=k+1}^N (z_i - z_k) F_i, \quad (3.5)$$

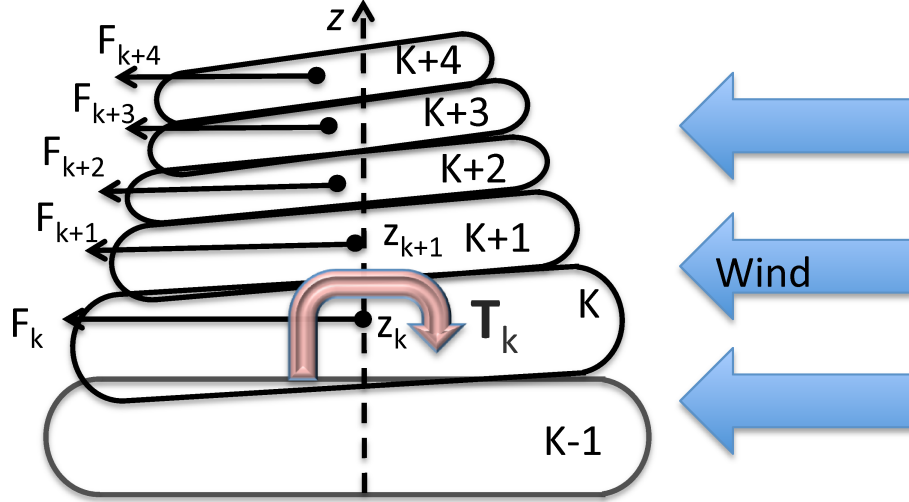


FIGURE 3.3: An illustration of torque balance on the flexible tower.

and the condition for the equilibrium is simply $T_{k,w} = T_k$ for each k , where T_k is given by Eq. (3.3) and $T_{k,w}$ by Eq. (3.5). More precisely, we get a system of coupled, nonlinear difference equations for ϕ_k as follows:

$$p_k \pi q_k^2 (s_k \sqrt{2r_k |q_k \phi_k - q_{k-1} \phi_{k-1}|} - s_{k+1} \sqrt{2r_k |q_{k+1} \phi_{k+1} - q_k \phi_k|}) = \sum_{i=k+1}^N C_d U_i^2 r_i (\pi r_i + 2q_i) \cos \phi_k (z_i - z_k). \quad (3.6)$$

Note that our equations are invariant with respect to rotations about the vertical axis z , but not with respect to horizontal axes (x, y) . However, we do not think that this symmetry must be enforced. The strong winds that may threaten the structure normally blow in the horizontal direction only (it is highly unusual to have a vertical or inclined wind, although there are rare exceptions). In addition, the bottom torus is fixed to be horizontal, so the z -direction is truly special. A reader will notice that we have computed all the deformations by projecting the boundary of the tori onto the z -axis, see Eq. (3.2). A more detailed deformation estimate

based on the Euclidian differences between the tori boundaries could be derived, but this would make the solutions appreciably more complicated (although still attainable). Thus, we believe that our solution represents a sufficiently accurate description of the tower design under the constraints as described here.

It is worth noticing that *given* the geometry of the tower, all the angles can be found in a recursive manner. While that solution may be interesting for applications, we will proceed in a different way. We will find the geometry of the tori and corresponding shapes of the tower that, in some sense, optimize deformations along the tower for uniform winds.

It is also worth noticing the singular nature of Eq. (3.6) when the arguments in the square roots tend to zero. It may seem like these forces are singular when no deformations are present and thus must be avoided, for example, by regularizing this force and taking into account small deformations caused by the static weight of the tori at rest. This indeed will make the reaction forces linear for small angles and square root like for large angles. However, in our opinion, dealing with the square roots is advantageous. First, for any reasonable wind speeds, the deformations will be described by the square root, rather than the small deformation regularizations, so the square root is truly physical. Second, and more important, this singularity is in *restoring* force, which means that the restoring force is faster than any linear force could have been, and thus the system is, loosely speaking, more than linearly stable. There is a large body of literature dedicated to the dynamics of chains with singular forces of this type, called Hertzian-type chains, see for example [17, 18].

These works show that the singularities of this type are actually advantageous, in addition to being scientifically interesting.

3.3.2 Analytic solution for tower shape

The system of difference equations (3.6), in general, cannot be solved analytically. However, an explicit solution can be found in a particular case of ϕ_k being small, so $\cos \phi_k \simeq 1$. This is true even for rather large values of deflection from the vertical, for example, if $\phi = \pi/6$, then $\cos \phi \simeq 0.86$ which is still acceptable. In principle, this analytic solution can be found for any function $C(\xi)$ and any velocity profile $U(\xi)$. However, to keep the discussion concise, we shall assume, just like it was done in Eiffel's considerations, that the force exerted by the wind per unit area is constant. That assumption is not essential, but it is commonly used and it does make the formulas substantially simpler. Thus, for the torque balance, we posit

$$p_k \pi q_k^2 (s_k \sqrt{2r_k |Q_{k+1}|} - s_k \sqrt{2r_k |Q_k|}) = f \sum_{i=k+1}^N r_i (\pi r_i + q_i) (z_i - z_k) = T_{k,w}, \quad (3.7)$$

where for convenience we have called

$$Q_k = q_k \phi_k - q_{k-1} \phi_{k-1}, \quad k > 1. \quad (3.8)$$

Let us rewrite this equation as

$$\sqrt{2r_k |Q_{k+1}|} + \sqrt{2r_k |Q_k|} = \alpha_k = \frac{T_{k,w}}{p_k \pi q_k^2} \quad (3.9)$$

If one assumes free boundary conditions $Q_N = 0$ on the top, where $k = N$, then starting at $k = N - 1$ and computing $k = N - 2$, $k = N - 3$, *etc.*, we find the exact solution of Eq. (3.9) as

$$\begin{aligned}
Q_N &= 0 \\
\sqrt{2r_{N-1}Q_{N-1}} &= \alpha_{N-1} \\
\sqrt{2r_{N-2}Q_{N-2}} &= \alpha_{N-2} - \alpha_{N-1} \\
\sqrt{2r_{N-3}Q_{N-3}} &= \alpha_{N-3} - \alpha_{N-2} + \alpha_{N-1} \\
&\dots \\
\sqrt{2r_2Q_2} &= \alpha_2 - \alpha_3 + \alpha_4 - \alpha_5 + \dots
\end{aligned} \tag{3.10}$$

Since Q_k is only defined for $k > 2$, there is no equation for Q_1 . This, in turn, gives values of Q_k explicitly as

$$\begin{aligned}
Q_N &= 0 \\
Q_{N-1} &= \frac{1}{2r_{N-1}}\alpha_{N-1}^2 \\
Q_{N-2} &= \frac{1}{2r_{N-2}}(\alpha_{N-2} - \alpha_{N-1})^2 \\
Q_{N-3} &= \frac{1}{2r_{N-3}}(\alpha_{N-3} - \alpha_{N-2} + \alpha_{N-1})^2
\end{aligned} \tag{3.11}$$

$$\dots \tag{3.12}$$

$$Q_2 = \frac{1}{2r_2}(\alpha_2 - \alpha_3 + \alpha_4 - \alpha_5 + \dots)^2. \tag{3.13}$$

Thus, the values of Q_k can be computed analytically for every set of torque values $T_{k,w}$ generated by the wind. Once the values of Q_k are found, we can find the

angles ϕ_k from Eq. (3.8). This time, we need to start from the bottom, at $k = 0$, and utilize the boundary condition that the first torus remains fixed, *i.e.* $\phi_1 = 0$. From Eq. (3.8), we get, iteratively:

$$\begin{aligned}\phi_2 &= \frac{1}{q_2} Q_2 \\ \phi_k &= \frac{1}{q_k} (Q_k - q_{k-1} \phi_{k-1}), \quad k = 3, \dots, N.\end{aligned}\tag{3.14}$$

Solution (3.11,3.14) is valid for an arbitrary set of radii q_k and r_k and applied wind forces, no optimization procedure has been undertaken yet. Different conditions can be imposed on the optimization, and the analytic solution we have derived here allows for a quick and efficient tower design. As an example, let us demonstrate how to optimize the tower in a specific case of practical importance for the solar updraft tower.

Under the influence of strong winds, the tower will deform according to Eq. (3.6). While deformation, even a large one, may be acceptable in a flexible structure, we want to enforce the uniformity of this deformation along the tower. More precisely, we would like to avoid the situations when the tower “breaks” (kinks) at some point, restricting the air flow and rendering our design inoperative. Thus, in what follows, we consider optimizing the tower design so there is as little chance as possible for the obstruction of the air flow inside the tower to occur. As one will see below, the optimization procedure is not unique. In the rest of the paper, we shall assume that the chance of obstruction is minimized if the following condition is enforced:

The vertical compression of any torus caused by the wind has to be a fraction μ of

the radius of that torus, with μ being the same for all tori. This way, the relative deformation caused by the wind is equally distributed along the tower and makes it less likely for the air flow in the tower to be blocked.

This condition, expressed in formulas, enforces $h_k = \mu r_k$, where h_k is both the upwind and downwind parts defined by Eq. (3.2). Let us for convenience non-dimensionalize the excess pressure p_k in each torus using, *e.g.*, the atmospheric pressure p_0 , so that $P_k = p_k/p_0$. Thus Eq. (3.6) now defines a set of conditions for q_i as follows:

$$P_k \pi q_k^2 p_0 \sqrt{2\mu} (r_k - r_{k+1}) = f \sum_{i=k+1}^N r_i (\pi r_i + 2q_i) (z_i - z_k), \quad k = 1, \dots, N-1 \quad (3.15)$$

Since f also has units of pressure, we can set

$$\mu = \frac{1}{2} \left(\frac{Vf}{p_0} \right)^2, \quad V \text{ dimensionless}, \quad (3.16)$$

so that the constant V is the sole dimensionless dynamic parameter containing the information about loading due to the wind and reaction forces.

The numerical value of the parameter V for design of a particular tower should be chosen in such a way that for typical winds in the area the tower should be fully operational. For example, the value $V = 2000$ that we chose will facilitate continuous operation for sustained winds on the order of 10 m/s. If stronger winds are anticipated, the tower should be simply deflated. In our opinion, it does not make sense to plan for uncommon, extremely high, hurricane-strength winds (say, 35 m/s and above), as this will lead to small values of parameter V and,

correspondingly, to a tower which is very inefficient for energy production due to severe constriction on the top.

With this convenient rescaling using V , Eq. (3.15) becomes:

$$VP_k\pi q_k^2(r_k - r_{k+1}) = \sum_{i=k+1}^N r_i(\pi r_i + 2q_i)(z_i - z_k), \quad k = 1, \dots, N - 1. \quad (3.17)$$

The optimization proceeds as follows:

1. Specify the desired geometry of the tori, which is obtained from either engineering or economy reasons. We shall perform computations for two particular examples: a) all tori are the same small radius, $r_k = R$, and b) all tori are similar in shape, so $r_k/q_k = \text{const}$.
2. Specify the geometry of the *top torus only*, *i.e.*, $q_N = q_T$. This scale is normally determined from engineering considerations, such as the power of the turbine and the cost of the apparatus.
3. One can further adjust excessive pressures P_k to improve the flow of air through the tower by changing its shape, for example, increase the diameter of the upper tori. Generally, higher pressures P_k lead to larger diameters on top and smaller on the bottom. Thus, we shall assume that P_k are chosen to be maximum possible for each torus, limited by the fabric strength, and assume $P_k = P$ for all k in what follows. ²
4. Using typical wind for the area, estimate the parameter V in (3.17).

²See also (3.20) using p_k to control the dynamics

5. Solve for tower shape, *i.e.* determine q_{N-1}, q_{N-2} *etc.* recursively from (3.17).

Optimization procedure I Let us first illustrate the results of the optimization procedure when for all r_k being the same, $r_k = R$ for $k = 1, \dots, N$.

We shall denote this solutions as "fixed-height" design. The advantage of this procedure is that the shape q_k can be computed explicitly if we define the top torus' geometry, *i.e.* q_N and $r_N = R$.

This equation can be solved by specifying the scale, let us say $q_N = q_T$ – the radius of the top torus – and proceeding to q_{N-1}, q_{N-2} and so on until we reach q_1 . Once we obtain the sequence of radii q_N, q_{N-1}, \dots , we can choose an arbitrary part of this sequence and it will be satisfying the optimization condition as well. We use that fact to remove the expanding part of the tower developing for the step from N to $N - 1$ unless the constant V is chosen to have a particular value.

For this calculation, we assume that all z_i to be equally spaced, so that $z_i - z_k = H(i - k)$. We shall also assume that all the tori are inflated to the same pressure $P_k = P = 1$, meaning the excessive pressure in each torus is equal to the atmospheric pressure. In Fig. 3.4, we present a tower shape obtained from Eq. (3.17).

It is also interesting to make a note about the connection between the towers presented here and Eiffel's idea, leading to exponentially decreasing width of the tower versus height. In our case, the dependence is, in general, not exponential. For some designs when R_k is a certain power of q_k , the shape has the form $q_k \sim f(k) \exp(-\gamma k)$ where $f(k)$ is a slowly varying (algebraic) function of k , and

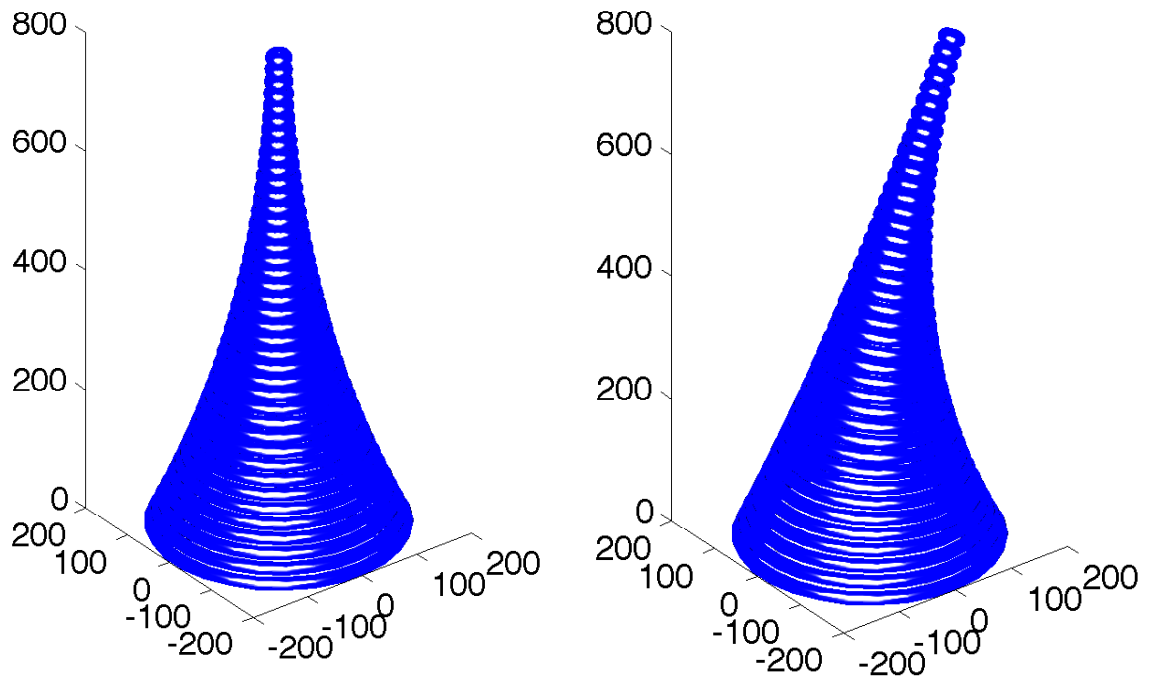


FIGURE 3.4: Left: solar tower computed from Eq. (3.17) with $V = 2000$. The radius of the bottom torus is roughly 200 m, top torus 10.5 m, the tower height is 800 m and the inner diameter of each torus is 10 m (leading to a rather severe constriction on top). Right: the same solar tower with the relative maximum deformation δR_k for each torus being 1% of the smaller radius $R_k = R$. Since the radius q_k of the tower is smaller at top, and $R_k = R = \text{const}$, the tilt ($\arctan(h_k/q_k)$) is correspondingly larger for the top tori.

γ is a parameter depending on V and P . For $R_k = R = \text{const}$, the dependence of the tower width with height is approximately quadratic. It is interesting that some analogues with Eiffel's ideas persist here, radically different physics notwithstanding. This is probably the best testament to Eiffel as a modern visionary, whose ideas reach far beyond his time.

Optimization procedure II Let us now turn to the tower design using similar tori, when $r_k = \alpha q_k$ with α being a given number, common for all tori. Such a selection means that all the tori are similar in shape, but vary in size.

We shall call this "proportional" design. Considering q_k as the unknown variable in (3.17) gives an implicit equation for q_k as a function of q_{k+1} :

$$VP_k\pi\alpha q_k^2(q_k - q_{k+1}) = \sum_{i=k+1}^N r_i q_i (\alpha\pi + 1)(z_i - z_k), \quad k = 1, \dots, N-1. \quad (3.18)$$

with

$$z_{k+1} - z_k = 2r_k = 2\alpha q_k. \quad (3.19)$$

Equations (3.18) and (3.19) must be solved simultaneously, as coupled implicit equations. Starting with $q_N := q_T$ as before, and choosing, for example, $z_N = 0$, we can find q_{N-1} and z_{N-1} , followed by q_{N-2} and z_{N-2} and all the way to q_1 and z_1 . Since z_k only enter the equations in a difference with other z_k , we can choose $z_1 = 0$ by a simple shift. In Fig. 3.5, we show the results of simulations with $V = 2000$ and $\alpha = 0.2$. We also show the tower deformed under the wind force. It is clear that such a procedure is advantageous to the optimization procedure defined in Fig. 3.4, as the constriction of the tower is much less severe at the top. The proportional tower design is clearly advantageous over explicit designs: for the same values of the parameter V , corresponding to the same wind speed tolerances, the proportional tower design is much less restrictive with regard to the air flow inside the tower. Conversely, had we taken the tower designs obtained by the fixed-height and proportional methods with similar levels of internal flow constriction, the fixed-height design would have had considerably less tolerance to wind. The superior performance of the proportional design will also be demonstrated below in the analysis of Section 3.5.

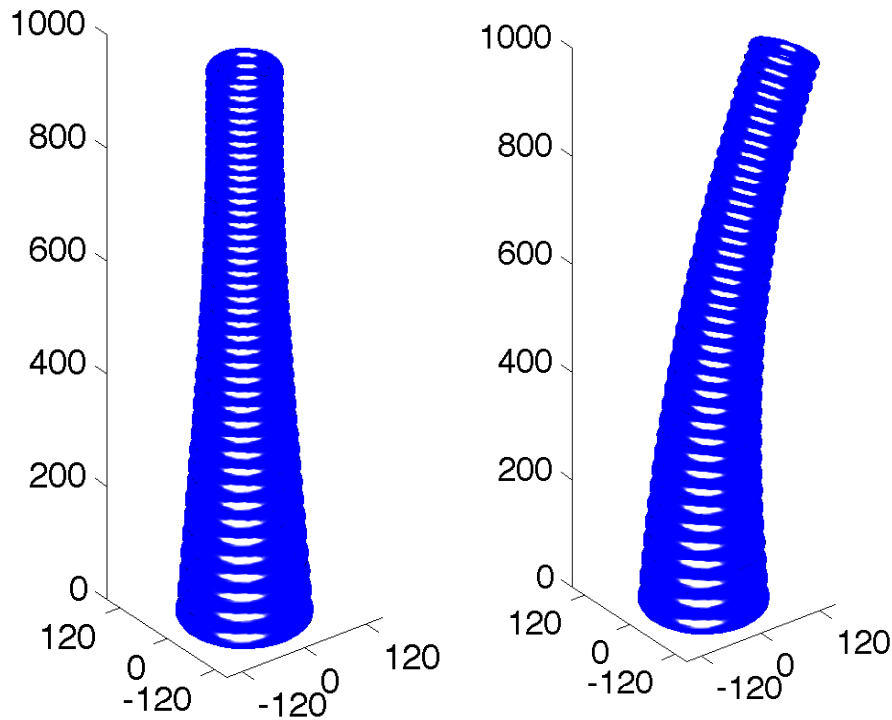


FIGURE 3.5: Left: solar tower computed from Eq. (3.18) and (3.19) with $V = 2000$. The ratio of smaller to larger radii of all tori is assumed to be 0.1. The radius of the top torus is 50 m, the radius of the bottom torus is 88.4 m. Right: the same solar tower with the relative tilt for each torus being 1% .

3.3.3 Control of tower deformation using adjustable air pressure

The calculations we have done in this paper so far were based on rather simple and crude estimates of the wind forces for each individual bladder. However, it is certainly true that the wind resistance is far more complex than we have assumed here, so pre-inflating each bladder to the computed pressure will not produce exactly the desired deformation profile in practice. This problem can be dealt with by controlling the pressure in each bladder in real time, using the deformation of the

tower as a guide. This procedure can also accommodate arbitrary change of wind speed away from the surface, thus adding robustness to the tower construction.

Consider, for the moment, the idealized situation where all the forces on each bladder are known, and we need to compute the pressures P_k yielding a given deformation profile, namely, the set of deformation angles ϕ_k . This problem can be solved exactly even in the more complex formulation of Eq. (3.6), as the left-hand side of the equation is proportional to p_k , and the right-hand side is independent of p_k , so the solution is computed simply as

$$p_k = \frac{\sum_{i=k+1}^N (z_k - z_i) F_i}{\pi q_k^2 (s_k \sqrt{2r_k |q_k \phi_k - q_{k-1} \phi_{k-1}|} - s_{k+1} \sqrt{2r_k |q_{k+1} \phi_{k+1} - q_k \phi_k|}}. \quad (3.20)$$

This solution is simple, but of course too idealized. In reality, the forces on each bladder are not known. However, the deformations of the tower can be measured in real time. This can be accomplished by either scattering a light from small reflective elements attached on the outside of the tower, analyzing tower shapes from on-site visual observations, installing small beacons (possibly including GPS units) along the tower, etc. Thus, if we consider ϕ_k to be known from observation, and also p_k known from valve and pressure sensors, then from the equilibrium conditions (Eq. (3.6)) we can determine F_i , $i = 1, \dots, N$ by solving a linear system. Once F_i are known, we can solve Eq. (3.20) to determine the pressures necessary to equilibrate the tower to the desired configuration. The pressures in each bladder have to be adjusted accordingly. Unfortunately, this will alter the shape of the tower and thus change all F_i , and the process would need to be repeated. Luckily, the procedure converges, so the desired configuration can be reached, provided

that the time necessary to adjust the pressures in the bladders is much smaller than the typical time of the wind change.

3.3.4 Deformations of bladders due to the supporting weight

One may wonder whether the tower will be able to support its own weight, since it is made out of elements that are heavier than air, and overpressure in the bladders increases their mass. That would certainly be a problem with the cylindrical tower, which will need rather a high overpressure to keep it upright and stable. However, remember that the cross-section of the tower and thus the weight of each torus is decreasing rapidly with height. It is most convenient to illustrate this for the case of an exponential tower. In that case, the weight of all the bladders, including extra air, above a given level is always roughly equal to the fraction of the weight of the bladder itself. This can be seen as follows. Let us assume that the mass of the bottom bladder is M_0 . Then, the mass of the k -th bladder roughly equals $q^k M_0$ with $0 < q < 1$, up to algebraic corrections in k (such as k^2) which grow much slower than q^k . Then the mass of all the bladders above the k -th bladder is

$$\sum_{i=1}^N M_i = \sum_{i=1}^N q^i M_0 = q^{k+1} M_0 \frac{1 - q^{N+1}}{1 - q} \simeq \frac{q}{1 - q} M_k. \quad (3.21)$$

Since the radius of the bladder also decreases exponentially with k , the larger bladders in the bottom will have proportionally more area to support the extra weight. This translates into roughly equal deformation relative to the bladder's size.

A more precise calculation for the shapes shown in Fig. 3.4 gives the relative deformation of each bladder in the inflated state to be about 1% of the radius of each bladder, for the conditions used in the computations for these figures, and correspondingly produces no appreciable change in the pressure. Thus, the towers will have no difficulty supporting their own weight.

The heavier-than-air design of the towers has additional effects on the stability:

1. As we discussed above, the use of the ambient air for inflation radically simplifies addition of air into the towers. The tower can be built to remedy small leaks appearing in bladders with a pump and valve system.
2. The use of ambient air also allows additional control of the tower rigidity by inflating and deflating each individual bladder.
3. Due to a very large support system and optimized wind torque application, the tipping of the tower is unlikely, and the base of the tower will not detach from the ground even under strong wind loading.
4. Should one of the bladders develop leaks too strong for the pumps to compensate for, it can be simply deflated. The tower's center of mass, as well as the center of torque application, will move downward, and the tower will remain stable. This will allow the tower to operate until necessary repairs are ready to be made.
5. Because of the use of the ambient air, should repairs be needed, *e.g.* to repair a leaking bladder, all the tori below it can be deflated and then re-inflated again, making it possible to conduct all repairs at or near ground level. If

the tower is built in an area prone to excessively strong winds exceeding design tolerances, due to *e.g.* hurricanes or tornadoes, then the tower can be deflated when such an inclement weather is approaching and re-inflated when it has passed.

3.4 Savings and other considerations

Let us begin with noting that a careful cost study for the construction of a solar-chimney power plant with an inflatable tower should be conducted together with a parametric investigation of the proposed plant geometry, performance, appropriate materials and components, etc. Here we present some preliminary considerations suggesting that the inflatable design may not just simplify the construction, but bring along substantial cost savings when compared with the rigid-tower design.

Costs of the construction of full-scale solar chimney plants with a rigid chimney have been assessed by [19], [20], [21], and recently by [22] for comparable power plants (output 100 MW, chimney height between 850 and 1000 m). However, the estimates of the cost of the chimney varied rather strongly – from the best case of 68 million to 156 million. Notably, the chimney represents at least about 20% and likely as much as about 40% of the total cost of the construction.

Any cost estimate of the inflatable tower would involve a large inherent uncertainty, simply because there are few, if any, precedents for building kilometer-sized inflatable structures. One estimate that appeared in the literature relates to a free-floating buoyant tower using the design originally proposed by [12]. The

estimate presented in the paper by [23] is USD 30 million, which includes the costs of gas (helium) and rigid structural elements necessary for that construction. This suggests that our free-standing solar tower might be even cheaper.

A crude cost estimate for the solar tower we propose may be obtained using the pricing of a mass-produced inflatable structure similar in size to the basic element of the chimney described above, namely the torus. Pre-fabricated spherical coated-fabric helium-filled advertising balloons (diameters ~ 8 m) are commercially available from a variety of sources for about USD 800. One can theoretically use the same fabric, although modern film materials, such as [24] may be more appropriate for our design, as they have superior resistance to wear and elements, and lower cost. If we estimate our cost (scaled up about sixfold from an 8 m balloon to a 50 m torus) as USD 5,000 per torus on average, which should also include the air valve and pressure sensor, then the rough estimate for the cost of fabricating a 1 km tall tower suitable for a 200-MW plant and consisting of 500-1,000 tori would be USD 5 million (or, 3.8 million, using a 1.316 conversion rate). Let us mention here that the inflatable tower design also saves on foundation work and transportation costs, as compared with the rigid towers. Thus it is reasonable to expect that the cost of the inflatable tower will be at least several times lower than that of the rigid tower. Moreover, the difference in costs is likely to increase with chimney height.

An additional possibility of savings (which should be considered in detail in future work) involves the turbine(s) used to produce electricity. For a traditional cylindrical tower, these turbines are of modest sizes and can be installed in a ring at

the bottom of the tower, as Fig. 3.1 shows, with the axis of each of turbine parallel to the ground. An alternative is a single turbine (again, of relatively modest size) coaxial with the tower and located near the inlet. [25] considered using a conical tower with a turbine near the top. However, this design in combination with a traditional (rigid) chimney has no tangible advantages (why restrict the airflow?) and is likely to develop additional problems due to difficulty of maintenance and the extra expense required to strengthen the construction. In the case of an inflatable chimney, however, the shape of the tower is dictated by stability requirements, the extra mass near the top due to the turbine can be offset via buoyancy, and the maintenance procedure can be simplified by the ability to bring the turbine down to ground level via controlled deflation of the tower.

Let us warn the reader that the shape of the tower dictated by the stability considerations described in the previous section may impede the power production, similar to the converging tower of [25]. According to a numerical study of [10], if a converging, diverging, or straight chimney is to be considered with a turbine at the ground level, the most energetically advantageous configuration is that with a diverging (wider at the top) chimney. However, if a converging chimney shape is necessitated by other considerations, then the placement of the turbine near the top may have to be considered, as we discuss in the next section. Here the penalty in the power production due to the tower shape must be offset by the lowered upfront cost of the facility, or by the possibility of a taller tower for the same initial investment.

With a wide-based tower shown in Fig. 3.4, it may be possible to use a single

turbine with a vertical axis located at the inlet, or a smaller turbine near the exit. The next section discusses the respective advantages/disadvantages of different turbine placement choices and tower shapes. The dimensions of the tower could easily allow to adapt mass-produced turbines, with minimal modifications to the hub and additional ease of maintenance, because all the components can be serviced at ground level.

3.5 Modeling of the updraft flow

We performed numerical modeling with the goal to assess the effect the tower shape (as determined by stability considerations outlined in Section 3.2) has on the overall performance of the chimney. The scope of the modeling was limited by this goal, and thus we used simplifying assumptions to account, *e.g.*, for the effect of the turbine, etc., as described below. The simulations assumed a tower height of about 1 km. For this height, both the differences in temperature and in pressure at the bottom and the top have to be taken into consideration.

The simulation models both the chimney and the collector. The conditions at the entry of the collector are assumed as follows. Air enters the greenhouse at pressure 1 atm (101.3 kPa). We assume the unheated air outside the greenhouse is at $T_0 = 20$ °C. The temperature of the ambient air near the chimney exit can then be calculated using the standard value for atmospheric lapse rate [26], with the average drop of temperature with elevation estimated at 6.5 °C

per km. Pressure at the exit is calculated using the standard barometric formula $p(z) = p_0 \exp(-Mgz/RT)$, where z is the elevation, p_0 is ground pressure, M is molar mass, R is gas constant, and T absolute temperature. With setting $M = 29$ g/mol for air, this simple formula based on ideal-gas considerations is remarkably accurate (within 5% for elevations below 6 km, [27]) in predicting the pressure change with elevation. The numerical model has to take buoyancy into account.

For modeling, three tower geometries were used: one based on the fixed-height solution (Fig. 3.4), one based on the proportional solution (Fig. 3.5), and a straight tower with the same vertical cross-sectional area as the proportional tower. The modeling did not directly account for the presence of the turbine, but in numerical calculations for each geometry, three values of the pressure drop at the exit were considered. The first was zero. The second and the third were selected to represent characteristic values of pressure drops due to the use of a turbine at the bottom or at the top of the chimney.

The decision not to model the turbine explicitly was driven partly by computational limitations and partly by the motivation to preserve the simplicity and generality of the modeling, as we are primarily concerned with the effect of the chimney shape.

The numerical simulation assumes the flow of air in the chimney is steady (in the average flow sense) and axisymmetric. Based on the characteristic internal dimensions of the structure $L \sim 10$ m, and the anticipated velocities $U \sim 10$ m/s, the representative Reynolds number would be $UL/\nu \sim 6 \times 10^6$, indicating

turbulent flow. Thus $k - \varepsilon$ turbulence model was used. The calculations were performed with a commercial CFD package [28] on a 16-core AMD Opteron, 36 Gb RAM workstation. Several mesh sizes were used to ensure 99% or better mesh convergence. For the results presented here, this resulted in the computational domain discretized with 500,000 to 750,000 (depending on the specific geometry) two-dimensional unstructured mesh elements. Calculations were performed with double precision, the iteration error range was set not to exceed 10^{-6} (10^{-9} for the energy equation). Under these conditions, the solutions converged in less than 2,000 iterations for all cases.

At the entrance to the collector, the temperature and pressure were set to be T_0 and p_0 , at the exit of the chimney T_1 and p_1 . The latter value takes into account both the change in pressure in the atmosphere and the pressure drop added to account for the turbine effects. The outer radius of the collector was maintained at 1753 m for all the numerics, leading to the collector area of about 9.6 km². This choice was dictated by the largest grid size we could reasonably use while maintaining grid convergence at 99% or better. To simplify the calculations, the boundary conditions *both* at the collector surface and on the chimney wall were assumed to be convective, while the ground served as the source of constant heat flux at 770 W/m².

The chosen tower geometries are characterized by comparable surface and foundation areas, so the construction costs of all three designs would be similar.

Fig. 3.7 shows the velocity and temperature maps inside the chimney for all three tower shapes in the case when the additional pressure drop to represent the effect

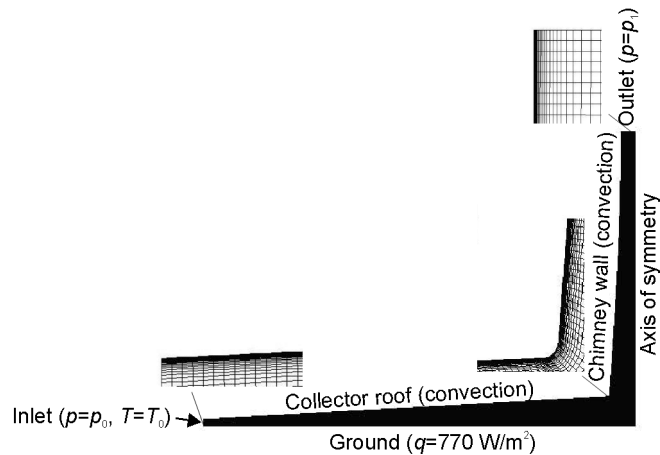


FIGURE 3.6: Computational domain, boundary conditions, and closeups of the grid for numerical modeling (proportional tower shape). For clarity, the most sparse grid is shown (50,000 nodes). The actual calculations used a finer grid with about 10 times more elements.

of the turbine was neglected. There are notable differences in the flow behavior, particularly prominent when the straight tower is compared with the fixed-height tower. For the former, velocity distribution is much more uniform, and the exit velocity is appreciably lower. The temperature at the core of the fixed-height tower is also much higher. We will compare the performance of all three geometries in quantitative terms, however, first let us provide some justification for the values we chose for the pressure drops included in the boundary conditions.

The pressure drops included in the boundary condition p_1 to simulate turbine losses (from stator, rotor, and diffuser) were estimated as follows. The efficiency of a turbine can be written in terms of total (inlet-to-exit) pressure loss ΔP_T as

$$\eta_{tt} = \left(1 + \frac{\Delta P_T}{\rho \Delta H}\right)^{-1}. \quad (3.22)$$

Here ρ is average density, and ΔH is the change in stagnation enthalpy. Equation (3.22) [29] was used by [30] for their calculations of the solar chimney turbine

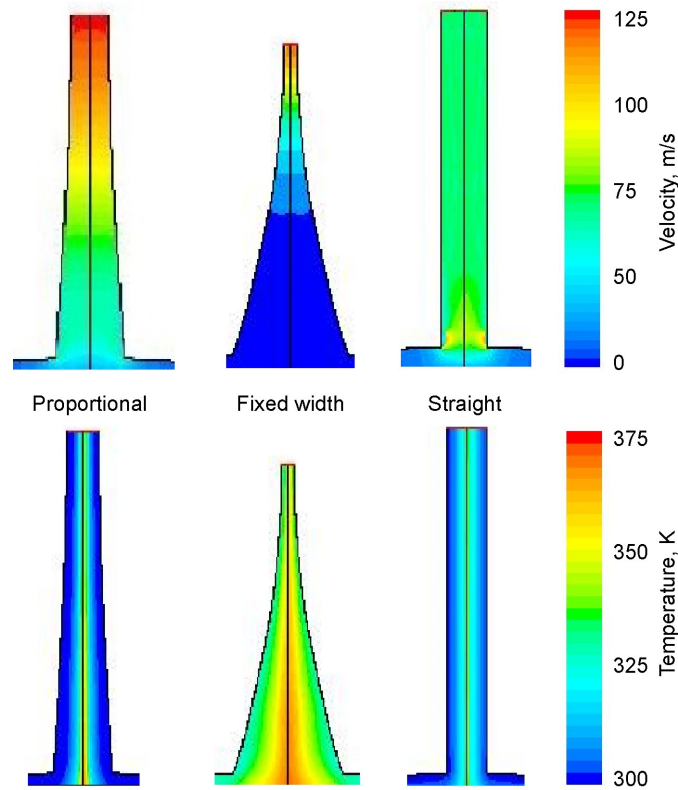


FIGURE 3.7: Results of numerical simulation of the air flow in solar updraft towers of different shapes (top row – velocity, bottom row – temperature, no ΔP_T pressure drop). Left –proportional shape with decreasing inner cross-section computed using Eqs. 3.18,3.19 with $V = 2000$. Center – fixed-height shape computed using Eq. 3.17 with same V value. Right – reference straight tower with the same vertical cross-sectional area as the proportional tower. The vertical extent of the images is 1 km.

characteristics, including efficiency. Here we can use the same equation “backwards” at a given location (e.g., bottom or top of the chimney) to estimate the pressure drop for known average flow parameters and prescribed efficiency η . Then the pressure drop is included into the outlet pressure condition p_1 , and the numerical calculation and subsequent estimation of the pressure drop repeated, usually providing convergence within 95% within two cycles of iteration. One more aspect of the flow the model does not take into account is the mixing in the flow due to the presence of the turbine, which is likely to affect the temperature and velocity fields.

Inasmuch as the turbine efficiency is concerned, different values are stated (or, in some cases, assumed) in literature – from 40 to 80% [31] to the highest attainable value of nearly 90% [30]. The latter is backed up by a careful treatment of all the factors contributing to turbine efficiency optimization, so we based our calculations described in the previous paragraph on 89% efficiency.

This procedure for estimating the pressure drops, while not at all rigorous, produces plausible values that manifest reasonable change with assumed location of the turbine – higher at the bottom of the chimney, lower near its top. Table 3.1 presents the quantitative results we obtained for the geometries and pressure drops we considered. In the first three columns, Table 3.1 lists the case number, the tower shape (proportional, fixed-height or straight), and the assumption about the turbine location (none, top, or bottom of chimney). In the fourth column we present the value of ΔP_t obtained by the iterative procedure described above.

For example, in the case of the straight chimney with no turbine (Case 5), the pressure difference between the inlet and the outlet is 10,000 Pa. With the turbine at the bottom (Case 7), $\Delta P_t = 4,700$ Pa, and the inlet-outlet pressure difference used in the simulation is reduced to $10,000 - 4,700 = 5,300$ Pa. The next two columns show the fluxes of kinetic energy at the top and at the bottom of the chimney in the form $1/2 \rho \bar{u}^3 A_c$, where \bar{u} is average vertical velocity at the appropriate location (top or bottom of chimney), and ρ and A_c are density and cross-sectional area of the chimney at that location. All of these numbers are normalized by the value for the straight chimney with the highest pressure drop. The last (seventh) column shows the estimate of the power output using the assumed pressure drop

Case	Tower shape	Assumed turbine location	ΔP_T , Pa	Scaled kinetic energy flux, top	Scaled kinetic energy flux, bottom	Scaled turbine output estimate
1	Fixed	None	0	1.91	0.01	-
2	Prop.	None	0	19.2	1.74	-
3	Prop.	Top	2048	14.0	1.27	0.47
4	Prop.	Bottom	4500	7.34	0.65	0.83
5	Straight	None	0	2.08	2.08	-
6	Straight	Top	2054	1.92	1.92	0.50
7	Straight	Bottom	4700	1.00	1.00	1.00

TABLE 3.1: Results of numerical simulations for different tower geometries and different assumptions about turbine placement and corresponding pressure drops. Labels “Fixed” and “Prop.” refer to fixed-height and proportional designs as described in the text. Kinetic energy fluxes $\frac{1}{2}\rho\bar{u}^3 A_c$ are normalized by the value for the straight tower and maximum pressure drop. Turbine output, estimated as $\eta_{tt}\bar{u}A_c\Delta P_T$, is likewise normalized.

ΔP_T at the chosen location (top or bottom of the chimney, according to column 3), and the value of turbine efficiency η_{tt} used in the same calculation. These fluxes show total extractable kinetic and pressure energy, without making any further assumptions about the turbine efficiency (with one implicit assumption used to estimate ΔP_T .)

Case 1 (Fixed height tower shape, no ΔP_T) was characterized by a very poor mass flow rate (8.2 times worse than the proportional tower) and kinetic energy flux, so that further cases for this geometry were not considered. This is not at all surprising, considering the strong role of the acceleration pressure drop in the chimney [32], which the converging design exacerbates. However, this does not rule out the use of the fixed-height shape altogether, because it may be feasible to decouple the outside shape of the tower from its inside shape, *e.g.*, by placing an expanding funnel inside a very wide fixed-height tower. The straight tower produces a little

more turbine power (16% for the bottom turbine location and maximum associated pressure drop) than the proportional tower. Thus the performance penalty for the proportional tower shape is quite modest.

Some interesting conclusions can also be derived from the results for kinetic and pressure energy fluxes, if these results are considered in the context of the power extraction technique. Modern wind turbines (referred to as lift turbines, [33]) use aerodynamic lift on their blades to extract a fraction of the kinetic energy of the flow. Drag turbines, relying on the force (and thus pressure) of the wind to power them, are also possible, however, lift turbines are usually about twice as efficient as the drag turbines in extracting energy from the flow [33]. There are also devices specifically designed to combine extraction of energy from lift and from drag (Savonius rotors, etc.). Here, however, let us limit our considerations to pure “lift” and “drag” devices. Table 3.1 shows that for a straight chimney and a prescribed pressure drop, there is no advantage in extracting kinetic energy near the top or near the bottom of the chimney. This will not be the case, however, for a converging chimney, where the kinetic energy flux is greater near the top. Thus, if kinetic energy is harvested, top turbine placement might be worth some consideration. The preferable drag turbine placement for the same chimney shape, on the other hand, would favor the bottom of the chimney.

For a practical decision on the turbine placement, additional factors must be considered. Bottom turbine placement is favorable for service access (although an inflatable tower with a turbine placed near the top can be deflated for turbine service). A slower-rotating and larger turbine located near the bottom of the

tower may be more expensive to maintain (because a reductor mechanism will be necessary) and may have lower efficiency. Another consideration pertinent to the turbines located near the bottom of the tower is that there, as [30] note, the flow enters in the *radial* direction from the collector to drive an *axial* turbine. That transition area could likely benefit from some optimization.

Let us also discuss how the results presented here compare with the results in literature. A well-known equation for the peak theoretical power P_{max} of a wind turbine, which disregards the contribution of pressure and just accounts for kinetic energy capture, can be written as

$$P_{max} = \frac{16}{27} \frac{\rho A_c \bar{u}^3}{2} \quad (3.23)$$

Here the ratio 16/27 is known as the Betz limit [34], or, more accurately, as the Lanchester-Betz-Joukovsky limit [35]. It refers to the maximum amount of kinetic energy of the flow of average density ρ and average velocity \bar{u} traversing the area A_c swept by the rotor of the wind turbine that can be converted to work. Many modern turbines have effective performance within 15% of that theoretical limit. The Lanchester-Betz-Joukovsky limit, however, does not apply to turbines in channels, which can actually produce more power than freestanding wind turbines. Thus columns 5 and 6 of Table 3.1 present (with normalization and no assumed coefficients) the same quantity as Eq. 3.23.

Another power estimate for a turbine in a solar chimney N_{el} [19] is

$$N_{el} = \eta_t \Delta P_T \dot{V}, \quad (3.24)$$

where η_t is a coefficient including the efficiencies of the turbine, gearing, and the generator, ΔP_T is the pressure drop at the turbine, and $\dot{V} = \bar{u}A_c$ is the volumetric flow rate. Equation 3.24 is effectively the same as one used to populate column 7 of Table 3.1.

Let us note that in our modeling, the collector roof was considerably taller than in many other simulations, and this may have had an effect of the flow behavior that may be worth considering further in terms of optimization – the velocity at the chimney exit is much higher, and the temperature increase across the collector – lower. Another reason for that might be in the sensitivity of the numerical model to the boundary conditions, in particular, the pressure boundary condition at the outlet. Our original assumption is that the inlet-outlet pressure difference driving the flow in a 1000 m tower is 10,000 Pa. For modeling the power plant in Manzanares [4] with FLUENT (the same software we employed), [36] applied a twofold approach. First, they derived a system of governing equations and solved it iteratively. Second, they used an axisymmetric CFD grid with $k - \varepsilon$ turbulence model. Both results were in good agreement with the experimental data, but it is noteworthy that the inlet-outlet pressure difference in the CFD modeling was zero.

As a check, we conducted a numerical simulation of the Manzanares plant with our model and simple boundary conditions consistent with those used by other researchers (Table 3.2), using the same assumption as [36] (trivial inlet-outlet pressure difference), and were also able to achieve very good agreement with the reported data (average outlet velocity 14.9 m/s, turbine output estimate 49 kW).

Position	BC type	Note
Collector inlet	Pressure inlet	$\Delta P \sim 0$
Collector ground	Wall	Heat flux 1000 W/m ²
Collector roof	Wall	Adiabatic
Chimney wall	Wall	Adiabatic
Chimney axis	Axis	Axial symmetry
Chimney outlet	Pressure outlet	$\Delta P \sim 0$

TABLE 3.2: Boundary conditions used for modeling the Manzanares power plant.

For the Manzanares tower of a relatively modest height, the zero pressure difference assumption makes better sense than it would for a 1000 m tower. However, modeling the exit of the 1 km chimney as a pressure outlet at 10,000 Pa less than the inlet pressure may also be less than perfect. For a more accurate representation, some volume of atmosphere above the exit could be considered, with appropriate wind speed and pressure conditions applied at its boundary. This would allow to account for the jet of air leaving the chimney and interacting with the atmospheric cross-flow, with the actual collector inlet to chimney outlet pressure difference likely different from 10,000 Pa. The computational penalty for implementing this representation, however, would be huge.

Thus for a 1 km tower, modeling with a trivial inlet-outlet pressure drop would at least represent an interesting limit case, which we decided to consider for the same three tower shapes as shown in Fig. 3.7. For all geometries, this modeling produced much reduced velocities at the tower exit (Fig. 3.8, Table 3.3). The straight chimney still produces the highest mass flow rate, but again, the proportional design does not fare too badly either – the decrease in kinetic energy flux compared with the straight design is only about 20%. The most realistic values for the exit velocities are likely somewhere in between the maxima and minima from Table 3.3,

	Fixed	Proportional	Straight
Case of 10,000 Pa, m/s	111.1	123.0	58.0
Case of no pressure drop, m/s	16.1	15.3	12.6

TABLE 3.3: Average exit velocities for different tower shapes and the cases of 10,000 Pa vs. zero inlet-outlet pressure difference. Pressure drop due to the turbine is not considered here.

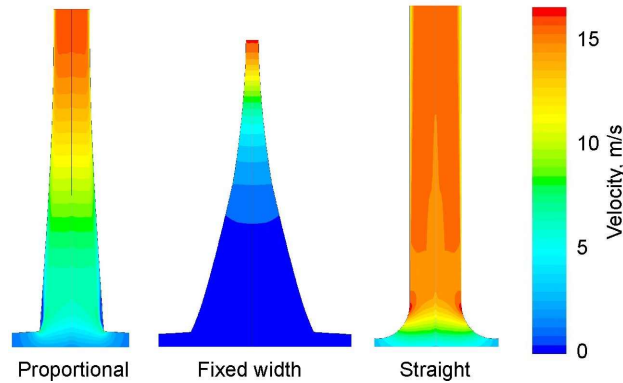


FIGURE 3.8: Velocity maps for the flow with no inlet-to-outlet pressure drop.

perhaps closer to the lower end of the range.

Our numerical analysis focused on the effects of the chimney *shape* rather than of the overall performance of the system, and used many simplifying assumptions. Thus a direct comparison with other modeling results presented in literature would not be rigorous or fair. However, it must be noted that the results for the straight tower shape (and bottom location of the turbine), when adjusted for the differences in the collector shape (in our model the collector area is relatively small, but the collector roof is taller than in most other models) are quantitatively consistent with the figures characterizing performance of 100-MW power plants from literature [19–22].

We must also add a cautionary note regarding the numerical results in general. Computational models of solar chimneys appear to be keenly sensitive to many subtle factors, including boundary conditions, geometry (especially if it includes

abrupt transitions), implementation of turbulence modeling, *etc.* Thus it is always advisable to validate numerical results with experimental data or, due to the lamentable scarcity of the latter, to use common-sense conservation and scaling considerations to check if the numerical results make physical sense. In the immediate future, we intend to acquire experimental data specifically pertaining to the effects of chimney and collector shape on the flow (using a small-scale prototype), and use that data to conduct a code validation exercise for a solar-chimney numerical model.

3.6 Conclusions

The proposed design makes it possible to radically reduce the challenges associated with the construction of a solar updraft tower, with the potential to greatly simplify the construction of solar updraft facilities and to make solar-generated dispatchable power available in a variety of locations. Realistic optimization considerations for the design lead to elegant analytic solutions describing a free-standing tower comprised of a stack of soft toroidal shells made from widely available materials. Replacing a traditional updraft chimney with such a tower will also result in a significant reduction in the upfront construction cost. The inflatable updraft tower shape dictated by stability considerations is less than optimal for producing the optimal *internal* flow, however, the penalty may be a fair trade-off for the simplification of construction and cost reductions.

In the immediate future, we plan a small-scale feasibility study that will involve constructing a prototype of an inflatable chimney at the University of New Mexico. The prototype will be highly reconfigurable and will allow us to examine several factors that may influence the chimney performance, including the collector height. Investigation of the prototype will also make it possible to address several other issues of importance not covered in the present study, such as the effect of flow-induced vibrations due to vortex shedding on the stability of the flexible chimney. In addition, the experimental data will provide a set of useful validation benchmarks for numerics³.

³Appendix B presents the validation experimental analysis.

Bibliography

- [1] Xinping Zhou, Fang Wang, and Reccab Ochieng. A review of solar chimney power technology. *Renewable and Sustainable Energy Reviews*, 14:2315–2338, 2010.
- [2] US DOE. Annual energy outlook 2011. US Energy Information Administration DOE/EIA-0383, 2010.
- [3] Xinhua news agency. China’s first solar tower plant starts operating in desert. News release, December 28 2010.
- [4] W. Haaf, K. Friedrich, G. Mayr, and J. Schlaich. Solar chimneys part I: Principle and construction of the pilot plant in Manzanares. *International Journal of Solar Energy*, 2(1):3–20, 1983.
- [5] D. Mills. Advances in solar thermal electricity technology. *Solar Energy*, 76(1-3):19–31, 2004.
- [6] J. Schlaich, R. Bergermann, W. Schiel, and G. Weinrebe. Design of commercial solar updraft tower systems utilization of solar induced convective flows for power generation. *Journal of Solar Energy Engineering*, 127:117–124, 2005.

-
- [7] J.V. Muñoz-Lacuna. Ciudad Real tendrá una torre solar que doblará en altura a las Torres Gemelas. *Las Provincias* (España), February 13 2006.
- [8] Ming Tingzhen, Liu Wei, and Pan Yuan. Numerical analysis of the solar chimney power plant with energy storage layer. In D. Yogi Goswami and Yuwen Zhao, editors, *Proceedings of ISES World Congress 2007 (Vol. I Vol. V)*, pages 1800–1805. Springer Berlin Heidelberg, 2009.
- [9] Atit Koonsrisuk and Tawit Chitsomboon. Dynamic similarity in solar chimney modeling. *Solar Energy*, 81:1439–1446, 2007.
- [10] A. Koonrisuk and T. Chitsomboon. Effect of tower area change on the potential of solar tower. In *The Second Joint International Conference on Sustainable Energy and Environment*, pages B–029, Bangkok, Thailand, November 2006.
- [11] Daya Senanayake. Chimney, US Patent 5527216, 1996.
- [12] C Papageorgiou. Solar turbine power stations with floating solar chimneys. *IASTED Proceedings of power and energy systems, EuroPES*, pages 151–158, 2004.
- [13] Christos Papageorgiou. Floating solar chimney, US Patent 7735483, 2010.
- [14] Christos Papageorgiou. *Floating solar chimney*, pages 187–222. *Solar Energy*; Radu D. Rugescu, ed. InTech Europe, 2010. ISBN 978-953-307-052-0.

- [15] P. D. Weidman and I. Pinelis. Model equations for the Eiffel Tower profile: historical perspective and new results. *Comptes Rendus Mecanique*, 332:571–584, 2004.
- [16] P. D. Weidman. Modified shape of the Eiffel tower determined for an atmospheric boundary-layer wind profile. *Physics of Fluids*, 21:067102, 2009.
- [17] A. Stefanov and P. Kevrekidis. On the existence of solitary traveling waves for generalized hertzian chains. *J Nonlinear Science*, 22:32749, 2012.
- [18] G. James, P. G. Kevrekidis, and J. Cuevas. Breathers in oscillator chains with hertzian interactions. *Physica D*, pages 39–59, 2013.
- [19] J. Schlaich. *The solar chimney: electricity from the sun*. Axel Menges, 1995.
- [20] Jorg Schlaich, Rudolf Bergermann, Wolfgang Schiel, and Gerhard Weinrebe. Sustainable electricity generation with solar updraft towers. *Structural Engineering International*, 14(3):225–229, 2004.
- [21] M.A.d.S. Bernardes. *Technische, ökonomische und ökologische Analyse von Aufwindkraftwerken*. PhD thesis, Universität Stuttgart, 2004.
- [22] TP Fluri, JP Pretorius, C Van Dyk, TW Von Backström, DG Kröger, and GPAG Van Zijl. Cost analysis of solar chimney power plants. *Solar Energy*, 83(2):246–256, 2009.
- [23] Xinping Zhou, Jiakuan Yang, Fen Wang, and Bo Xiao. Economic analysis of power generation from floating solar chimney power plant. *Renewable and Sustainable Energy Reviews*, 13(4):736–749, 2009.

- [24] Tedlar. DuPont Tedlar PVF Films and Adhesives, 2012. URL http://www2.dupont.com/Tedlar_PVF_Film/en_US/index.html.
- [25] M.A. Padki and S.A. Sherif. On a simple analytical model for solar chimneys. *International Journal of Energy Research*, 23:345–349, 1999.
- [26] P.H. Stone and J.H. Carlson. Atmospheric lapse rate regimes and their parameterization. *Journal of the Atmospheric Sciences*, 36:415–423, 1979.
- [27] J.K. Fink. *Physical Chemistry in Depth*. Springer, 2009.
- [28] CFD Fluent. ANSYS, 2012.
- [29] R.I Lewis. *Turbomachinery Performance Analysis*. John Wiley and Sons, London, 1996.
- [30] T.W. Von Backström and A.J. Gannon. Solar chimney turbine characteristics. *Solar Energy*, 76(1):235–241, 2004.
- [31] LB Mullett. The solar chimney – overall efficiency, design and performance. *International Journal of Ambient Energy*, 8(1):35–40, 1987.
- [32] T.W. von Backström and A.J. Gannon. Compressible flow through solar power plant chimneys. *Journal of Solar Energy Engineering*, 122(3):138–145, 2000.
- [33] P. Gipe. *Wind Energy Comes of Age*. John Wiley & Sons, Inc., 1995.
- [34] A. Betz. Das Maximum der theoretisch möglichen Ausnützung des Windes durch Windmotoren. *Zeitschrift für das gesamte Turbinewesen*, 26:207–309, 1920.

- [35] G.A.M. van Kuik. The Lanchester-Betz-Joukovsky limit. *Wind Energy*, 10: 289–291, 2007.

- [36] R. Sangi, M. Amidpour, and B. Hosseinizadeh. Modeling and numerical simulation of solar chimney power plants. *Solar Energy*, 85:829–838, 2011.

Part II

Combined Power Cycles

Chapter 4

Efficiency Enhancement of Solar Chimney Power Plant System by Use of Waste Heat from Nuclear Power Plant¹

A solar chimney power plant system (SCPPS) is an effective system for converting solar irradiation to electrical power. It can be combined with a conventional power plant to improve its efficiency and minimize its environmental impact. Rather than dumping the waste heat rejected by a nuclear power plant to a wet cooling tower, a better solution may be to connect it to an SCPPS. This is particularly true in arid regions. The SCPPS can serve the function of a dry cooling tower and produce

¹Originally to be published as: N. Fathi, P. McDaniel, S.S. Aleyasin, M. Robinson, P. Vorobief, S. Rodriguez, C. de Oliveira, "Efficiency Enhancement of Solar Chimney Power Plant System by Use of Waste Heat from Nuclear Power Plant", Journal of Cleaner Production, Elsevier, 2017.

additional electrical power. In a solar chimney power plant, the energy of buoyant hot air is converted to electrical energy. SCPPS includes a collector at ground level covered with a transparent roof. Sun heats the air inside the collector and the ground underneath. A tall chimney is placed at the center of the collector, with a turbine located at its base of the chimney. In this investigation, the surplus heat from the nuclear cycle is used to increase the temperature of the air in the collector and therefore produce more electricity in the solar chimney power plant. The efficiency of the nuclear plant will be lowered due to the higher temperature of the condenser, but the loss can be made up by the increased power of the solar chimney. Heat from the sun is always free once the solar plant has been constructed and is not normally considered in the efficiency calculation. Computational fluid dynamics (CFD) and thermal analysis has been performed to apply the available surplus heat from the nuclear cycle and measure the available kinetic energy of air for the turbine of the solar chimney power plant system. The feasibility of the system is evaluated, and the thermal efficiency of the combined power plant has been computed. By applying this idea to a typical 1000 MW nuclear power plant with a nominal 35.3% thermal efficiency, its efficiency can be increased to 42.0%. The combined cycle as presented is advantageous in environments where water is scarce. The cooling tower is replaced by the solar chimney power plant utilizing the surplus heat from the available warm steam in the secondary loop of the reactor.

Nomenclature

Variables

ϵ	dissipation rate (per unit mass), m^2/s^3
η	efficiency
g	acceleration due to gravity, m/s^2
h	height, m
k	turbulence kinetic energy (per unit mass), m^2/s^2
\dot{m}	air mass flow rate, kg/s
μ	dynamic viscosity
p	pressure, N/m^2
q	heat transfer per unit mass, J/kg
q''	heat flux, W/m^2
\dot{W}	flow power, W
R	air specific gas constant, $J/kg.K$
S	user defined source term
T	temperature, K
ρ	density, kg/m^3
u	velocity component, m/s
c_p	specific heat capacity, $J/kg.K$
σ	diffusion term
x	spatial component, m

Subscripts

th	thermal
------	---------

Abbreviations

<i>ASME</i>	American Society of Mechanical engineers
<i>CFD</i>	computational fluid dynamics
<i>CHT</i>	computational heat transfer
<i>CSP</i>	concentrating solar power
<i>CAM</i>	customer adoption model
<i>DER</i>	distribution energy resource
<i>EOS</i>	equation of state
<i>HES</i>	hybrid energy system
<i>FSI</i>	fluid solid interaction
<i>ISO</i>	independent system operator
<i>LWR</i>	light water reactor
<i>MSR</i>	molten salt reactor
<i>PV</i>	photovoltaic
<i>RPS</i>	renewable portfolio standard
<i>SRQ</i>	system response quantity
<i>TTD</i>	terminal temperature difference
<i>M&S</i>	modeling and simulation
<i>SCPPS</i>	solar chimney power plant system
<i>VHTR</i>	very high temperature reactor
<i>VPP</i>	virtual power plant

4.1 Introduction

4.1.1 Motivation and Background

While renewable energy systems are steadily improving their global share [1], the challenge is to convince the industry and governments to invest more money in the renewable energy field and to make it more attractive by decreasing the capital cost. Until recently, uncertainties in funding have limited renewable energy development, especially in the US. That limitation has been one of the barriers to progress. Another limitation of many renewable energy systems is the variability in their output, which makes them unsuitable for baseline power production. Therefore, fossil fuels are still the dominant source of energy globally. The estimated US energy consumption in 2015 relied heavily on fossil fuels which generated about 82% of US primary energy. Coal provides 58% of the energy used for power and most oil (71%) is used for transportation. Nuclear energy provides around 8% of the total primary energy consumption and all of it is used for electricity generation as is shown in Fig. 4.1 [2]. The share of nuclear energy in electricity generation is around 21%.

Fossil fuels have two major limitations including the finite sources, being a function of political and sectarian issues. Also, there is no balance between the fuel consumption and discovery of new fossil reserves around the world [3]. More importantly, the consumption of fossil fuels, which accounts for 60% global greenhouse gas emissions [4], has negative impacts on both environment and human

health. Climate changes including receding of glaciers [5], rise in sea level, desertification and formation of hurricanes are some of these destructive impacts on the environment [6]. On the other hand, every year millions of premature death and various diseases such as allergies and asthma [7] due to air pollution are reported worldwide. Only in the US, the US Environmental Protection Agency estimated that in 2010 there were more than 160000 premature deaths due to air pollution [8]. To tackle these issues, many countries introduced renewable energy plans and aim to supply part of their energy from renewable resources such as wind, solar biomass and geothermal. In 2014, the share of solar and wind powers in the net electricity consumption in the European Union was 12%; however, this share in Denmark and Portugal was 37% and 27%, respectively [9].

Proper technologies are required to extract electrical energy from solar energy. Solar chimney power plants are one of the available technologies which have been studied since 1970s.

The share of solar energy in 2015 US energy consumption is just 0.43%. This is a dramatic small share for solar energy. Solar energy incident upon the earth is considerable. However, it is diffuse and approximately 23% of the energy is absorbed by the atmosphere. There are different types of solar energy systems including flat-plate collectors like photovoltaic (PV), focusing collectors like solar concentrated tower (SCT) and SCPP. One of the systems which have not been studied comprehensively in the approach of combined cycle with other primary power plant systems is SCPPS.

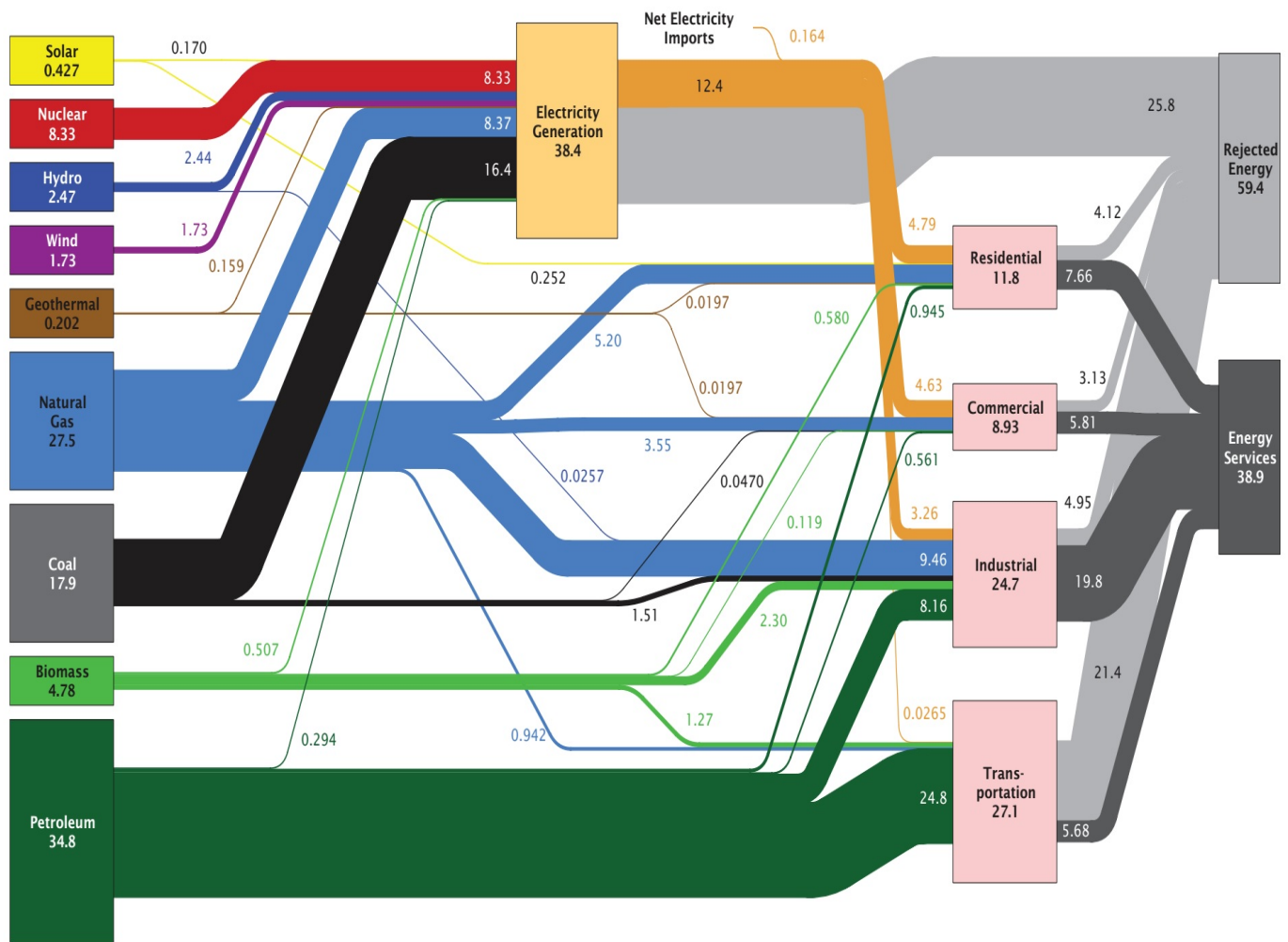


FIGURE 4.1: Estimated US energy flows in 2015. Values are in quadrillion British units. Total energy input is 98.3 Quads.

Solar chimneys are one of the rare examples of renewable energy power plants that can produce a reliable baseline power. In a solar chimney plant, the energy of buoyant hot air is converted to electrical energy. The plant consists of a collector at the base covered with a transparent roof that collects the solar radiation, heating up the air inside and the ground underneath. In the center of the collector, there is a tower, and a turbine is located at the base. The hot air flows up the tower as a result of the buoyancy effect, and its energy is extracted and converted to electrical energy by means of the turbine. A typical solar chimney is shown in Fig.

4.2.

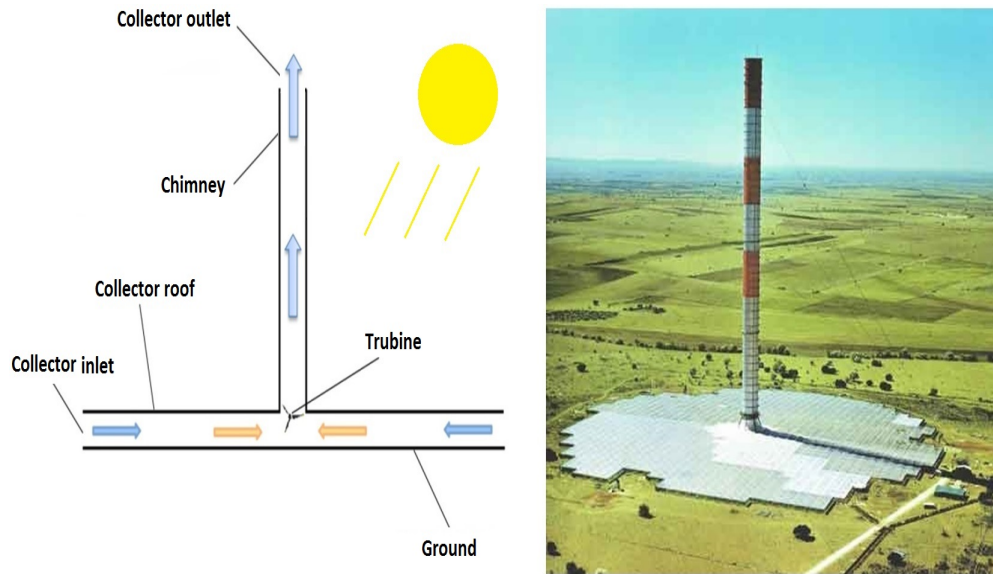


FIGURE 4.2: Schematic of an SCPPS (left), Manzanares prototype (right).

During the day, the sun heats the ground under the collectors, and at night, the heated ground continues warming the air, thus sustaining the power-generating updraft flow.

The primary goal of this research is a fundamental feasibility study of having SCPPS combined with a nuclear reactor power plant cycle to replace cooling tower. Consequently, the effect of this combined cycle on the efficiency SCPPS was also investigated. Therefore the second objective of this investigation is to detect the possible increase of SCCPS efficiency by utilizing the available waste heat. It was observed that the performance of solar chimney systems increases by making them utilize an available source of waste heat. This would make it possible to be built in a smaller scale.

4.1.2 Previous Work

The first prototype of solar chimney power plant was constructed in Manzanares, Spain. This plant operated between 1982 and 1989, and its electricity was used as a part of the local electrical network [10]. The information from the Manzanares prototype has been used for extrapolation to larger models for solar chimney power plant systems (SCPPS) [11]. In 1991 Yan et al. developed a detailed model for an SCPPS by using a practical correlation. They considered several key parameters, such as air velocity, air flow rate, output power, and thermal efficiency [12]. Several researchers studied the effect of different geometrical parameters on plant efficiency. In 1995 Schlaich et al. reported that according to the mathematical model, there were no optimal dimensions for a solar chimney; however, by considering construction costs, a thermo-economically optimal plant configuration might exist [13].

One of the important aspects of solar chimneys is that to provide 24/7 power and to be economically competitive, they must be built on a large scale, requiring corresponding upfront investment. The efficiency of SCPPS is extremely low ranging from 0.5 to 10% of solar energy input. Therefore, considerable research efforts have been made to enhance the efficiency of SCPPS. As the ground under the collector has a certain thermal storage capacity, during night time, SCPP cannot work as efficient as day time. Kreetz [14] introduced the concept of water-filled tubes/tanks under the collector roof to increase the thermal storage capacity. This idea helps to smooth out the generation of warm air to drive the turbine and improve the power output after sunset [15]. In an attempt to improve the SCPPS

function at night, double-roof collector was proposed by Pretorius [16]. This gives the plant the ability to store and release energy to regulate the output power.

It is usually assumed that the tall chimney follows a conventional design (rigid construction, foundation, guy wires, etc.). Such a construction on the scale suitable for a commercially viable SCPPS is not only very expensive, but also presents a challenge in terms of surviving an extreme weather event. To address this issue, a free-standing inflatable design was proposed to reduce the construction costs and increase the survivability of a solar chimney [17]. The prototype was able to withstand hurricane-strength winds [18]. Chimney outlet air velocity was measured experimentally as the system response quantities (SRQ) to validate the numerical simulation results [19].

Over the last few years, concentrating solar power system projects have been rapidly increasing [20]. In these systems, solar radiation is concentrated onto a focal point or line using mirrors or lens to enhance the efficiency of extracting solar energy compared to the conventional SCPPS.

Fig.4.3 depicts the open air Brayton cycle of a SCPPS. The concept presented here is a combined cycle adding the SCPPS to a power plant system to utilize the surplus heat and produce more electricity. In principle, many combined cycles using the same concept are possible, including SCPPS installations combined with an array of traditional PV collectors, with an array of algal bioreactors, or even installed over a landfill to utilize its waste heat. Several examples of combined cycles were described and studied to address sustainability challenges that energy industry faces [21]. This technology has a broad application to all thermal power

plants. Several investigations have proposed combined cycle power plants that utilize available heat from a high temperature reactor or fossil fuel plant [22]. Simplified mathematical models have been developed to study the thermal power plant system. A typical system has the heat recovery steam generator (HRSG) fed by the exhaust of the turbine. HRSG provides heat to produce steam that drives a bottoming steam turbine for extra electric power production [23]. In this article, the focus is on a typical nuclear power plant as the main element of this combined cycle. Current light water reactors (LWRs) power plants operate with thermal efficiencies in the range of 30 to 35% rejecting 65 to 70% of the energy consumed. Advanced molten salt reactors (MSRs) and very high temperature reactors (VHTRs) will reach efficiencies in the 42 to 48% range [24]. The ratio of heat output from a power plant that is actually converted into electrical energy is called the thermal efficiency, η_{th} of the system,

$$\eta_{th} = \frac{\textit{Electrical Energy Generated}}{\textit{Heat Produced by the Reactor}} \quad (4.1)$$

By combining the solar chimney tower system with a nuclear power plant, the overall thermal efficiency will increase because of the extra electrical power produced by the turbine in the SCPPS (Fig.4.4). The issue is how to apply the waste heat from the nuclear power plants, such as pressurized water reactor (PWR), molten salt reactor (MSR), or VHTR. The authors suggest replacing the cooling tower with an SCPPS to extract more heat from the overall system. This would make it possible to build smaller solar chimney plants and consequently decrease the upfront cost, producing a competitive levelized cost of electricity.

4.1.3 Utilization by Grid

The SCPPS technology can be added to the mix of generation resources. The SCPPS could enter the grid at several levels. The first would be to provide electricity, locally, for the power plant (pumps, fans, etc.). Secondly, it can be employed for direct use on the grid allowing the solar chimney to be used in various ways and fit in with the future framework of the grid. The simplest method by which the solar chimney can provide a service to the electrical grid is in economic dispatch mode. When the demand is high, output power from a solar chimney power plant can be dispatched to the grid before expensive peaking plants are used. However, this does not lend itself to day-ahead resource planning due to the solar chimney being a function of weather and cooling tower output, both of which are subject to random fluctuations.

In either scenario, potential output of the SCPPS can be used in forecasting to allow for optimization of the resources available locally or grid-wise. Presently, the grid is beginning a transformation from a centralized generation scheme to a distributed paradigm. There are many reasons for this development such as increased penetration of rooftop solar, the emergence of renewable energy portfolio standards (RPS) which requires a certain percentage of electricity generation from renewable sources, and an overall concern over reliability and sustainability of energy resources for consumers. The shift from centralized to distributed generation has led to changes in how loads are met in certain areas of the US (independent system operators), and developments continue to be proposed. An important recent concept that must be mentioned here is the virtual power plant (VPP) [25].

The idea of a VPP is to aggregate generation resources that may be small in capacity or intermittent (or both) and to let them act as a collective to meet the load (or perform another grid service). Another important development for the future of the grid comes from hybrid energy systems (HES). This concept decouples the pairings between the traditional sources and sinks, such as coal only for generation of electricity [26]. Fig. 4.5 illustrates the solar chimney as a resource in a VPP scheme. The resources are aggregated and with forecasts and current demand on the grid, a dispatch schedule is produced for each resource to satisfy the agreed bid to the independent system operator (ISO).

As the numbers of distributed resources continue to increase, there are several studies that show how the grid can benefit and continue to be stable. One example uses the distributed energy resource customer adoption model (DER-CAM). DER-CAM was initially designed to increase investment in distributed energy systems and provide a scheduling service for the resources [27]. As research continued, it was found that what is best for one customer may not be optimal for the operation of the entire grid. For example, if there are several cold water storage units on a grid, the optimal time to charge the individual units (for the customer) would be early morning before a time-of-use tariff or demand charge can be recorded. However, if all the individual customers do this, there will be a spike on that portion of the grid. DER-CAM was used to solve this issue by performing a collective optimization to save money for the consumer and smooth the spike [28].

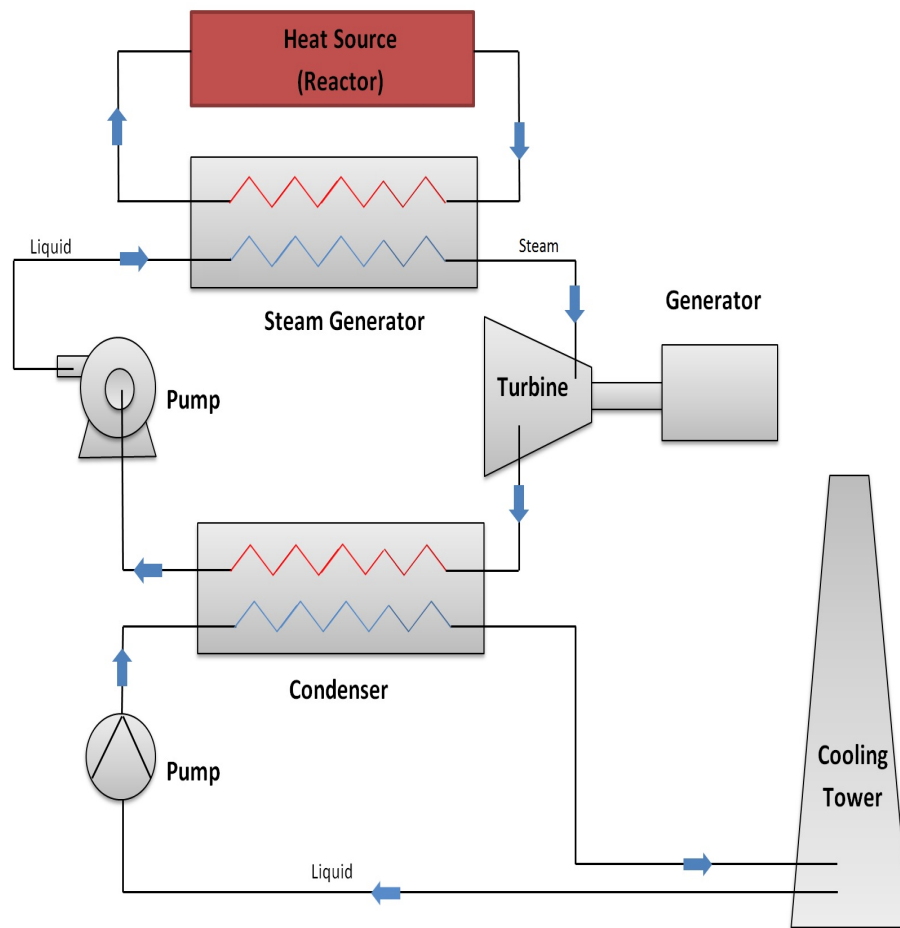


FIGURE 4.3: Schematic diagram of a pressurized water reactor and the steam turbine that convert work into electrical energy with a cooling tower.

4.2 Modeling and Simulation

4.2.1 CFD analysis

To have a better understanding of the air flow behavior in an SCPPS and its relationship with the available heat flux at the collector, computational fluid dynamics (CFD) analysis was applied. A CFD simulation using the finite volume method was employed to investigate the sensitivity of turbine output power to different values of the available heat flux at the collector part. This numerical flow calculation helps us to evaluate the nuclear-solar combined cycle when SCPPS is used

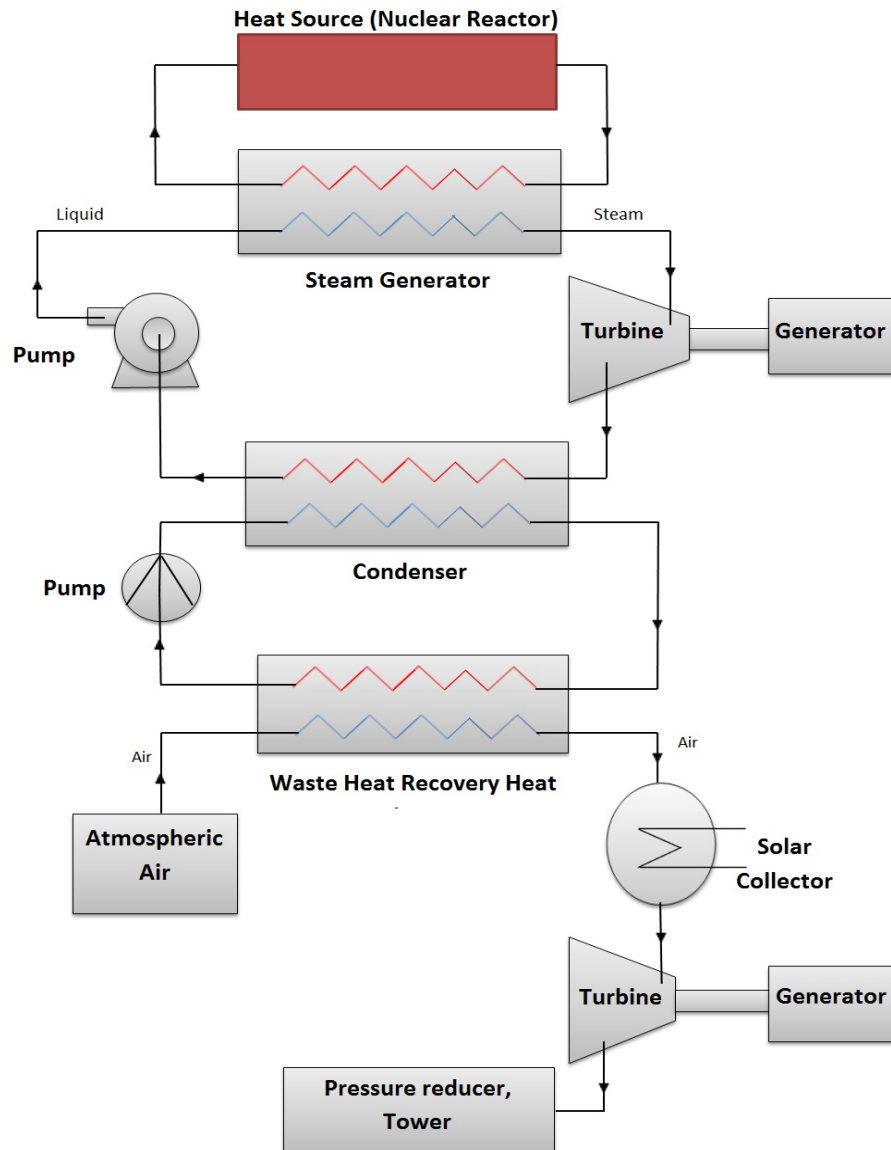


FIGURE 4.4: Block diagram of an open air-Brayton cycle of SCCPS (instead of cooling tower) combined with a pressurized water reactor.

to replace a conventional cooling tower. To date numerous numerical models with various coupling between the collector, turbine, and chimney have been introduced to evaluate SCPPS [29]. To measure the reliability of the CFD results, due to the limited available experimental data for validation, analytical correlation and mathematical models have been applied. The analytical correlation for output power for an SCPPS was studied, and the modified form of that was compared against

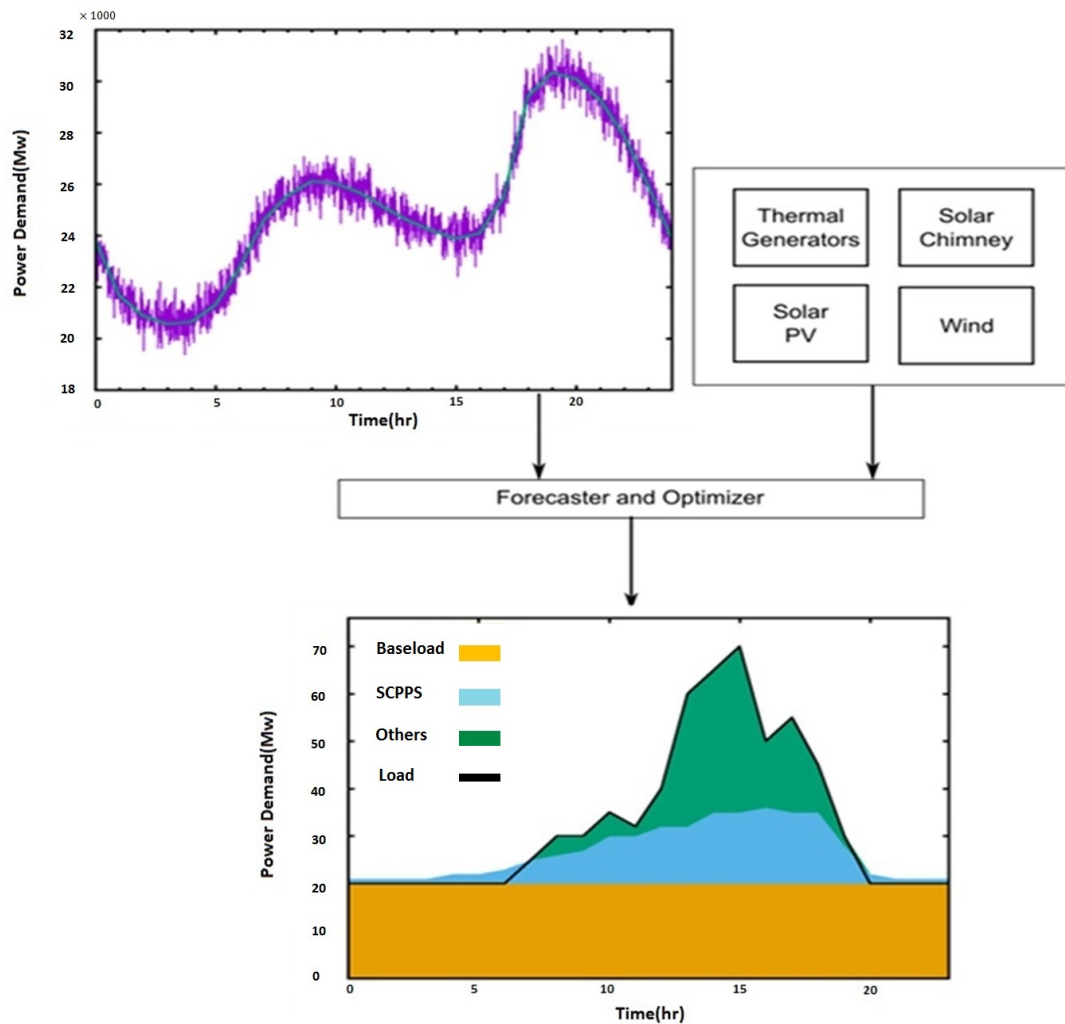


FIGURE 4.5: Example process of producing a schedule given base load generators, solar chimney, and other distributed energy resources (DERs; such as photovoltaic arrays, wind farms, etc.).

CFD and available experimental data from the Manzanares prototype [30]. In the present investigation, the Manzanares prototype was modeled and simulated by considering the real dimensions and available operating conditions with respect to the available reports [2]. Table 4.1 presents the dimensions of the Manzanres prototype.

In the numerical analysis, the heat flux was calibrated with respect to the actual values from the available experimental data. The mass flow rate obtained from

Prototype component	Size (m)
Mean collector radius	122.00
Collector height	1.85
Chimney radius	5.08
Chimney height	196
Rotor blade length	5

TABLE 4.1: Manzanares prototype dimensions.

the CFD results, along with other parameters, was used to evaluate the maximum mechanical power for each case. ANSYS ICEM (Integrated Computer Engineering and Manufacturing) CFD was employed to generate a quadrilateral cell mesh. The calculations were carried out on a four-core, 32GB RAM Xeon computer. Table 4.2 presents the applied boundary conditions in our numerical flow calculation.

To perform this steady-state CFD simulation, the standard $k - \epsilon$ two-equation model was applied. The standard $k - \epsilon$ model has been a common turbulence model in industrial CFD since it was proposed by Launder and Spalding[31]. This is due to its robustness, economy, and reasonable accuracy in simulation of certain basin turbulent flows in engineering applications. However, unless special measures are taken $k - \epsilon$ models are not suitable in the evaluation of flows where adverse pressure gradients or separation are present. They typically predict a delayed and reduced separation compared to observations. This can result in overly optimistic design evaluations for flows which separate from smooth surfaces (aerodynamic bodies, diffusers, etc.). The $k - \epsilon$ model is therefore not widely used in external aerodynamics. Applying a wall function helps the accuracy of the standard $k - \epsilon$ model. The standard $k - \epsilon$ model includes two extra transport equations: one for turbulence kinetic energy (k) and the other for dissipation rate (ϵ). The model

transport equation for k was adjusted from the exact equation based on experimental data. However, the model transport equation for ϵ bears little resemblance to its mathematically exact counterpart. The standard $k - \epsilon$ is suitable for high Reynolds-number flows, and the setup we investigate here definitely falls within the high Reynolds number range, especially in the tower it exceeds 10000.

Model component	Boundary condition
Collector ground	Thermal flux
Chimney wall	Adiabatic
Collector roof	Adiabatic
Chimney center line	Axis
Collector inlet	Zero gauge pressure
Collector outlet	Zero gauge pressure

TABLE 4.2: Applied boundary conditions in CFD analysis

$$\frac{\partial \rho}{\partial t} + \frac{\partial}{\partial x_j} [\rho u_j] = 0 \quad (4.2)$$

$$\frac{\partial}{\partial t} (\rho u_i) + \frac{\partial}{\partial x_j} \left[\overline{\rho u'_i u'_j} + u_i \frac{\partial u_j}{\partial x_j} - \nu S_{ij} \right] + \frac{\partial p}{\partial x_i} = 0, \quad i = 1, 2, 3 \quad (4.3)$$

Here u_i is the local velocity and u'_i represents the velocity fluctuation. S_{ij} is the mean strain rate calculated as follows:

$$S_{ij} = \frac{1}{2} \left(\frac{\partial u_i}{\partial x_j} + \frac{\partial u_j}{\partial x_i} \right) \quad (4.4)$$

The equations for turbulence kinetic energy k and dissipation rate ϵ are

$$\frac{\partial}{\partial t}(\rho k) + \frac{\partial}{\partial x_i}(\rho k u_i) = \frac{\partial}{\partial x_j} \left[\left(\mu + \frac{\mu_t}{\sigma_k} \right) \frac{\partial k}{\partial x_j} \right] + G_k + G_b - \rho \epsilon - Y_M + S_k \quad (4.5)$$

$$\frac{\partial}{\partial t}(\rho \epsilon) + \frac{\partial}{\partial x_i}(\rho \epsilon u_i) = \frac{\partial}{\partial x_j} \left[\left(\mu + \frac{\mu_t}{\sigma_\epsilon} \right) \frac{\partial \epsilon}{\partial x_j} \right] + C_{1\epsilon} \frac{\epsilon}{k} (G_k + C_{3\epsilon} G_b) - C_{2\epsilon} \rho \frac{\epsilon^2}{k} + S_\epsilon \quad (4.6)$$

Here G_k and G_b denote the generation of turbulence kinetic energy due to the mean velocity gradients and buoyancy respectively. Y_M represents the contribution of the fluctuating dilation in compressible turbulence to the overall dissipation rate. σ_k and σ_ϵ are turbulent Prandtl numbers for k and ϵ respectively. $C_{1\epsilon}$, $C_{2\epsilon}$ and $C_{3\epsilon}$ are constants. S_k and S_ϵ are user-defined source terms.

4.2.2 Thermal analysis

In this investigation, the second part of M&S was performed by means of numerical thermal simulation to identify the thermal characteristics of the combined nuclear-solar cycle. Once the thermal characteristics of the systems have been identified, then a search can be undertaken for off-the-shelf components that come close to meeting the requirements of an optimal system. Fathi et al. reported the results of thermal power cycle assessment of combined nuclear power plants for low carbon grids recently by using a steady state thermal cycle modeling [32]. Here we provide a simple example of a solar tower power plant coupled to a nuclear power plant.

The nuclear power plant is modeled schematically, and the focus of the exercise is on the effects of the coupling. Only one steam turbine is considered and no nuclear feedwater heaters are included. Both of these would add to the cycle efficiency for the basic plant and the combined plant and their absence does not detract from the essence of the analysis.

To perform the cycle modeling the techniques described in [33] were followed. Scaling parameters given in [34] were applied for size estimates for turbomachinery. Air compressor and turbine polytropic efficiencies follow the published scaling rules [33]. Steam turbines were simply set at a 90% isentropic efficiency. The heat exchanger was designed to meet a 1% pressure drop and the effectiveness of 95%. The output power of SCPPS was considered as an electrical power to the combined thermal cycle.

4.3 Results and Discussion

4.3.1 CFD/Thermal Results

In the following subsection, we present the results of the preliminary analysis of combining a larger (200 MW) SCPPS with a 1000 MW nuclear power plant. The goal of the CFD analysis is to have a better understanding of the air flow behavior with respect to the different rate of available heat flux (solar irradiation and nuclear waste heat). For this purpose, several CFD exercises were performed for different values of heat flux to cover all the cases. The minimum available solar radiation

characterizes the winter case. From a typical 1000 MW nuclear reactor, 600 W/m^2 extra added heat flux can be obtained from the waste heat. A nominal output power for the Manzanares prototype is about 50 kW based upon the experimental data. Fig. 4.6 presents a comparison of the available turbine output power based on reported experimental data for the Manzanares power plant (experimental data in Fig. 4.6) and on our CFD results for the same setup, including the case when the solar output of the plant is boosted by adding 600 W/m^2 from the waste heat.

In our numerical calculation, we have considered the turbine efficiency as 85%. As shown in Fig. 4.6, the output in the light blue area (200-400) represents the winter case. The same case boosted by 600 W/m^2 from the available surplus heat is represented by the light orange zone, and is roughly the same as the unboosted summer case. Note that the available surplus heat from the secondary cooling loop of the reactor, considering the operating range of heat exchanger effectiveness, may be appreciably greater than 600 W/m^2 . However, with respect to the reported characteristics of the Manzanares prototype, the above-mentioned flux value is chosen as the designed shift range of heat flux [30]. For the summer case, it is assumed that the amount of power increase can be zero for the maximum available reported solar irradiation of 1000 W/m^2 , to be more conservative in our evaluation. By considering both the summer and winter cases using the Manzanares SCPPS as a model, we obtain a range from 0 to 300% increase in the output electricity of the turbine of the solar chimney power plant. For the annual added power, 150% is chosen, ignoring the power increases during fall and spring cases to be on the conservative side. By building a bigger prototype on the order of 1 km height,

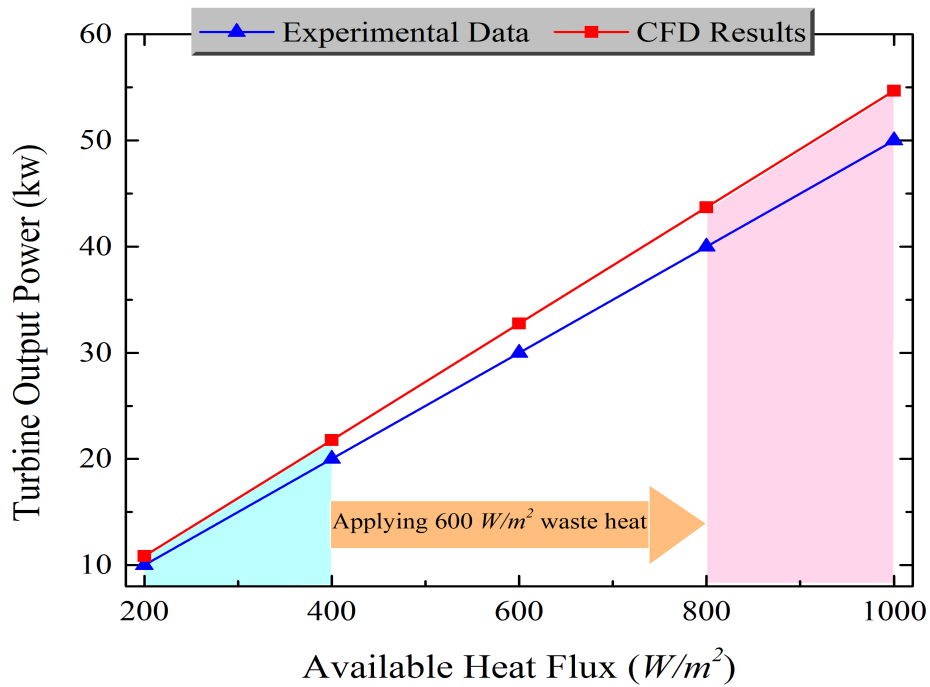


FIGURE 4.6: Experimental and numerical comparative representation of the output turbine power of Manzanares prototype vs a range of available heat flux and the effect of applying heat waste to the solar cycle

power generation from the turbine can be raised from 100 to 200 MW. That makes the presented idea more economically beneficial and decreases the capital cost of the SCPPS and the nuclear power plant as well

A brief outline of the thermal analysis approach to be considered was set forth in the modeling and simulation part. The presentation of the current investigation and results will follow simple coupled nuclear-solar cycle. Consider a nominal nuclear power plant that produces saturated steam at 7.2 MPa and $288 \text{ }^\circ\text{C}$. This gives an enthalpy of 2769.9 kJ/kg and an entropy of $5.80029 \text{ kJ}/(\text{kg K})$. Start by considering a nominal standard day at $15 \text{ }^\circ\text{C}$. Expanding the steam isentropically to an average day condenser pressure of 6.58 kPa and a temperature of $38 \text{ }^\circ\text{C}$

gives a final enthalpy of 1793.3 kJ/kg. The nominal terminal temperature difference (TTD) across the condenser is 23 °C. The ideal enthalpy drop across the turbine is 976.6 kJ/kg. For a 95% efficient steam turbine, the net work will be 927.7 kJ/kg resulting in a steam quality of 69.8% and an enthalpy of 1842.2 kJ/kg at turbine exit. To return the saturated water to 7.2 MPa requires 9.1 kJ/kg for an 80% efficient pump or a net energy produced of 918.7 kJ/kg. Then to raise the temperature to 288 °C requires 2602.3 kJ/kg. This gives a thermodynamic efficiency of $918.7/2602.3 = 35.3\%$. A 1000 MW(e) power plant will require a heat input of 2832.8 MW(t) and a heat dump to the circulating water system of 1832.8 MW(t).

Now consider a hot day when the water reservoir is 30 °C and the condenser maintains the same TTD. The condenser conditions are now 53 °C and 14.2 kPa. This gives a turbine work of 830.3 kJ/kg and a steam turbine exit quality of 71.3%. The efficiency drops to 33.3%. The electrical power output is now 942.7 MW(e) and the circulating water heat dump is 1888.2 MW(t). Consider also a nighttime temperature of 5 °C. The efficiency will be 36.7%. The electrical power output will be 1038.4 MW(e) with a circulating water heat dump of 1794.1 MW(t).

Now let us add a solar tower to this power plant to perform the function of waste heat removal. For a nominal 1000 MW(e) nuclear plant we will add a 200 MW(e) solar plant to dissipate waste heat and produce additional electricity. Nominal conversion efficiency for the solar energy absorbed will be 8%. We will assume that the Terminal Temperature Difference for the collector of the solar tower is

the same at 23 °C. We are now cooling the steam with air, but the heat exchanger (solar collector) is very large. However, the solar collector will heat the air by an additional 20 °C, and the solar collector heat exchanger surface is another 10 °C above the peak air temperature. So the minimum condenser water temperature will be $23 + 20 + 10 = 53^{\circ}\text{C}$. Accordingly, on a 30 °C day the condenser steam temperature will be 83 °C, and the pressure will be 53.2 kPa. The reactor will produce 828.6 MW(e) and the reactor efficiency will drop to 29.2%. But by rejecting the waste heat to the solar collector, the solar system will now produce 360.3 MW(e) for a nominal 200 MW solar tower. The total station power output will be 1188.9 MW(e).

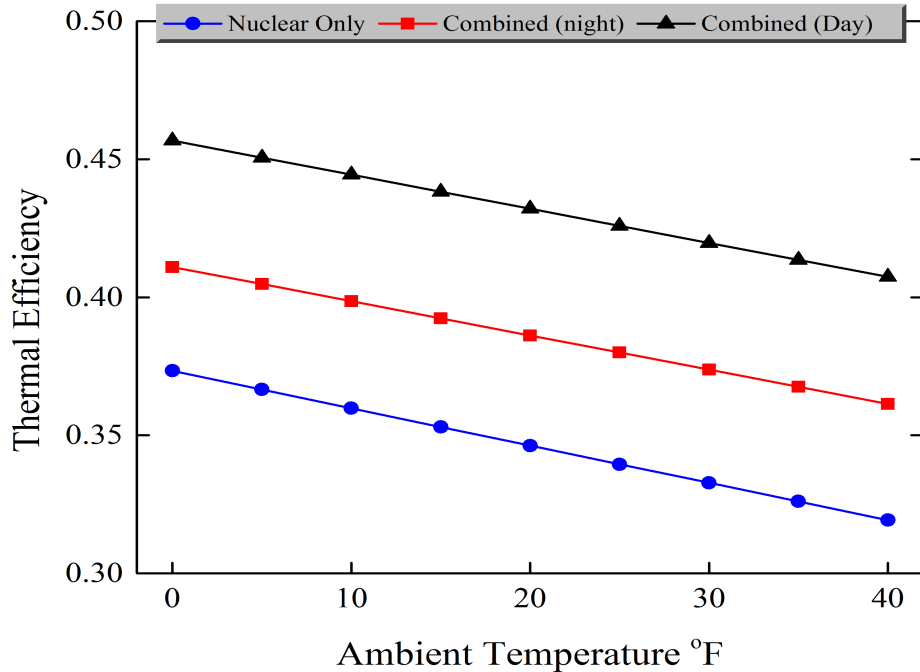


FIGURE 4.7: Thermal Power Plant efficiencies vs. Ambient Temperature.

This gives a combined efficiency for the nuclear plus solar plant of 42.0%, treating

the solar energy input as free. The increase in efficiency is 8.7% relative to the stand-alone nuclear plant. Similar efficiencies as a function of ambient temperatures are plotted in Fig. 4.7 for the basic nuclear plant, the nuclear and solar plants combined during daylight operation, and the nuclear and solar plants combined during nighttime operation. At the night time condition of 5 °C, when the solar tower receives no solar gain, the power produced by the SCPPS will be 146.6 MW(e) because it is being driven by the waste heat from the nuclear plant that would normally go to the circulating water system. This gives an overall plant efficiency of 40.5%, or an increase of 3.8% over the stand-alone nuclear plant operating at night-time temperatures. These calculations are summarized in Table 4.3. It is noteworthy that Fig. 4.7 shows a decrease for efficiency improvement with the combined cycle as the ambient temperature increases, which suggests that use of the combined cycle in hot and arid environments might be advantageous. This advantage may be made even more important when increased temperature due to climate change [35] is taken into consideration.

	Nuclear only	Nuclear hot day	Nuclear night	Combined nominal	Combined hot day	Combined night
Ambient temperature (°C)	15	30	5	15	30	5
Throttle enthalpy (kJ/kg)	2769.9	2769.9	2769.9	2769.9	2769.9	2769.9
Condenser temperature (°C)	38	53	28	68	83	38
Condensor pressure (kPa)	6.58	14.2	3.75	28.4	53.2	6.58
Turbine exit quality	0.698	0.713	0.688	0.728	0.742	0.698
Nuclear plant efficiency	0.353	0.333	0.366	0.313	0.293	0.353
Combined efficiency	0.353	0.333	0.366	0.438	0.420	0.405
Nuclear plant power (MW(e))	1000	942.7	1038.4	885.6	828.6	1000
Solar plant power (MW(e))	0	0	0	355.8	360.3	146.6
Total power (MW(e))	1000	942.7	1038.4	1241.3	1188.9	1146.6

TABLE 4.3: Comparison of nuclear only power plant with combined nuclear and SCPPS

This analysis can be extended to smaller ratios of SCPPS to the power produced by the nuclear plant. The results are plotted in Fig. 4.8. One can see that the combined daytime efficiency increase falls considerably with a decrease in the

solar plant design power. Realistic considerations for sizing the SCPPS should include efficiency (favoring larger sizes) and cost. Here applying the inflatable towers [8] could make larger solar components more feasible by lowering the cost of construction.

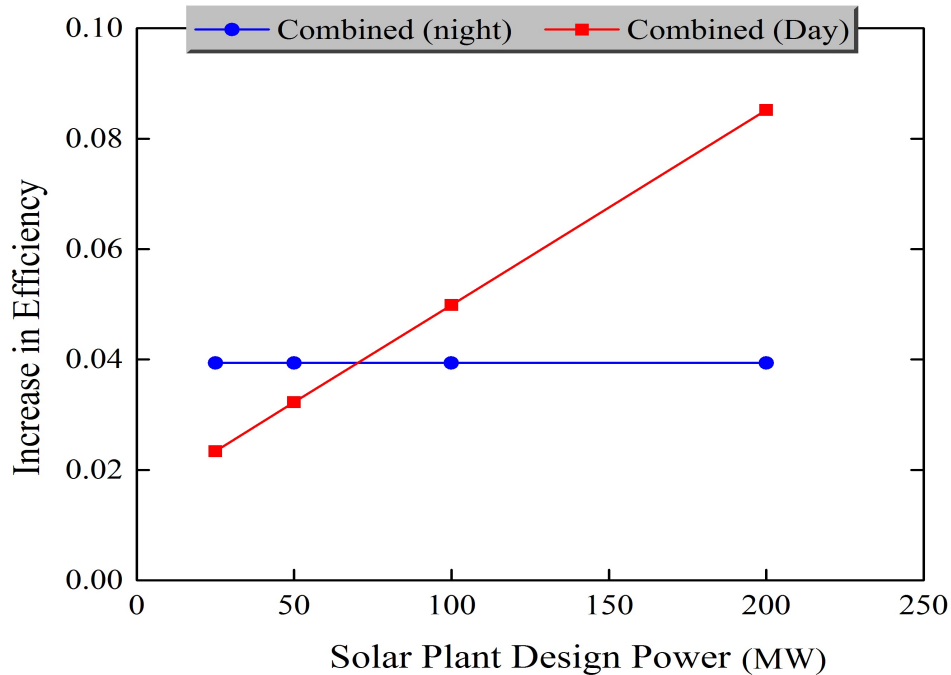


FIGURE 4.8: Increase in efficiency vs. the output power of SCPPS.

It is interesting to note that even at night, the efficiency increases, but the increase remains constant at about 4% even for smaller ratios of the solar tower power to the nuclear plant power. Only when the collector cooling can no longer maintain an exit TTD of 23 °C will the efficiency gain drop. Given the size of the required collectors, this will likely hold true down to relatively small SCPPS. By adding the solar tower as both an energy producer and waste heat absorber, the combined system has eliminated the need for a circulating water system. Thus the requirement to be located near a water supply has been eliminated.

4.3.2 Economic Considerations

As the results in the previous subsection shows, even a modestly-sized SCPPS can increase the efficiency of a nuclear power plant – both during the day and night-time operation. The boost in overall efficiency increases with the size of the SCPPS, but from practical considerations, an optimal size for the SCPPS component of the combined plant likely exists. In fully assessing the economic feasibility of the proposed combined cycle, costs must be compared between a power plant with a traditional cooling tower and with a solar chimney. A full comparison should consider construction costs, operation costs (including the cost of water), and the levelized electricity cost, and deserves a thorough future study. Here we present a preliminary assessment showing that the cycle we describe is likely not merely viable, but attractive from an economic standpoint. Here capital costs are the most important factor because they account for up to 74 % of the levelized cost of nuclear power [36].

Capital costs of modern nuclear power plants vary significantly – from USD 2 billion to USD 9 billion per unit, and have undergone a dramatic recent escalation, particularly in the US and in France [37]. Thus providing a realistic general capital-cost estimate for a nuclear power plant presents a considerable challenge. A study of a large number of nuclear power plants, both existing and under construction, in the US, and in Europe [38], provides an average capital cost estimate of GBP 4,613 (USD 7,381 using the 2012 conversion rate) per kW. For a 1000-MW power plant, that would mean the cost of USD 7.381 billion. Costs beyond the proper reactor, including the land and the cooling tower, can account for up to half of

the total amount [39]. Assuming a conservative estimate of the cooling tower and related systems comprising 15% of the cost of the plant, we arrive at a cost of USD 1.108 billion. Section 3 describes utilizing a 200-MW SCPP to dissipate the waste heat. A careful 2005 estimate of the cost of a 200-MW SCPP using a rigid tower is EU 606 million [40] (USD 770 million using the 2005 conversion rate, or USD 960 million adjusted for inflation to 2017).

Thus the capital cost of a traditional cooling tower and the cost of a rigid solar chimney-based cooling system are comparable. However, this does not take into account the savings that can be achieved by switching to a non-rigid tower design. The rigid tower accounts for at least 28 % of the total cost of the SCPP [40] (USD 269 million). A cost estimate for a replacement inflatable tower serving the same 200-MW plant is USD 5 to 30 million [17]. Replacing the traditional chimney with an inflatable one will also bring considerable savings in foundation construction and transport costs. Thus a solar chimney setup with an inflatable tower has the potential of both increasing efficiency and decreasing the capital cost.

4.3.3 Future Work

Our immediate goal is to design a platform based on numerical and analytical studies of all the components of the combined nuclear-solar thermal cycle. Specifically, we will consider the waste heat recovery heat exchanger which gets the surplus heat from the cooling loop of the nuclear thermal cycle and transfers it to the

open air Brayton cycle of the SCPPS. To have a better understanding of the performance of the whole combined cycle, thermal/CFD analysis will be performed for each of the components of the combined power plant cycle (Fig 4.9).

The thermal analysis will be performed by applying an open source object-oriented package, Modelica—block diagram thermal analysis. MATLAB thermal simulation also will be applied to perform code to code verification to evaluate the fidelity of our results. After performing the overall thermal/CFD analysis with respect to the available thermal hydraulics values, the waste heat recovery heat exchanger (Fig. 4.4) will be designed, rated and simulated based on ASME standards. Three-dimensional CFD/CHT simulations will be performed to have a better understanding of this heat exchanger and its thermal characteristics. Thermal/Structural fluid-solid interaction (FSI) simulation will be performed to observe the thermal stresses and evaluate the exchanger for all cases. As a final note, tube buckling and leakage analysis will be performed with respect to the CFD/CHT outputs to have a reliable design for the heat exchanger.

4.4 Conclusion

A novel idea to use the available surplus heat (waste heat) from thermal power plants for a solar chimney was presented to enhance the SCPPS efficiency compared to the traditional cooling setup. The possibility of this combined cycle was studied for a typical nuclear power plant. There also exists a possibility of reducing the capital cost of combined cycles for power plants, such as nuclear power plants

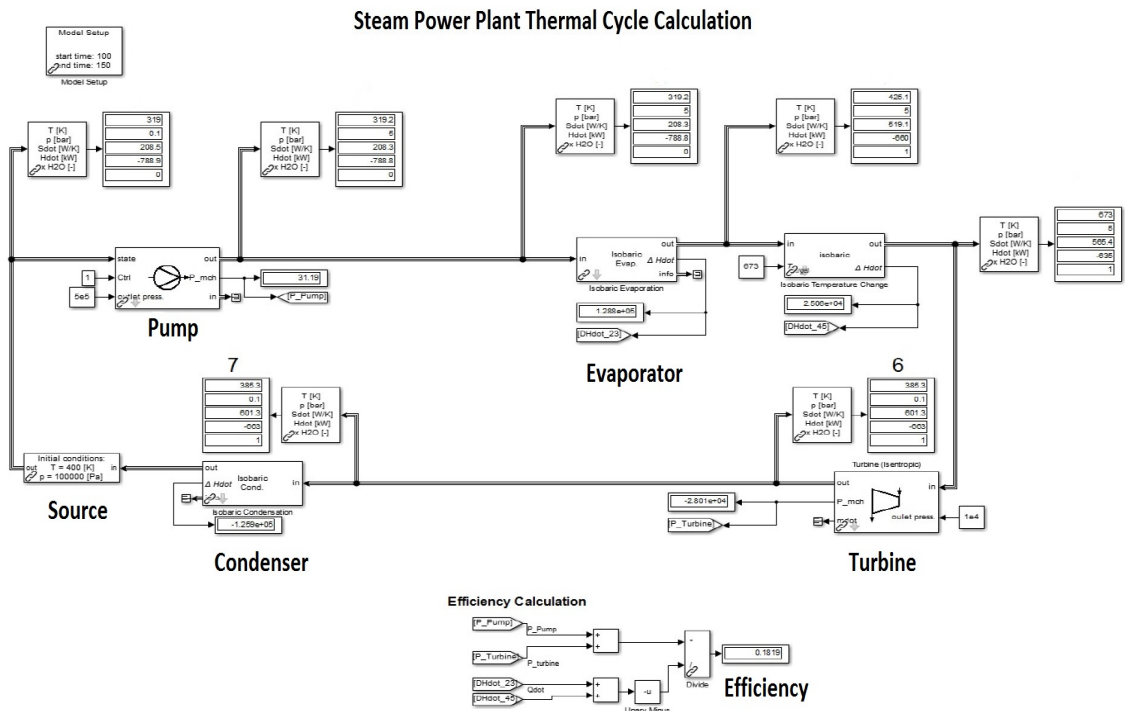


FIGURE 4.9: MATLAB thermal simulation block diagram for steam power plant cycle. 1-5 are thermal probes to read the thermal properties.

plus solar power plants. The total thermal efficiency of the combined thermal system can increase by up to 8.7%, which is considerable for the electrical power industry and should have a significant effect on capital cost and development of new generations of power plants. Utilizing the harvestable power increases the output power of the Manzanares-type SCPPS up to 150% annually. Another important advantage of the combined thermal system described here is that it does not require a body of water to provide cooling, and thus can be better suited for arid environments. This feature may become more important in the immediate future, as climate change is expected to lead to higher desertification of large areas. A detailed comparison of the technological complexity and cost of operation of the SCPPS versus the traditional nuclear plant cooling system remains a task for the future, along with considering redundancies that would need to be built

into the combined nuclear-solar power plant. Use of the recently proposed inflatable, free-standing chimney design is highly recommendable here both because it greatly reduces the SCPPS cost and increases its survivability to adverse weather events.

4.5 Acknowledgment

We would like to show our gratitude to Dr. Charles Forsberg, Department of Nuclear Science Engineering, Massachusetts Institute of Technology (MIT), for sharing many valuable insights with us during our work on this paper.

Bibliography

References

- [1] Trancik, Jessika E. "Renewable energy: Back the renewables boom." *Nature* 507, no. 7492 (2014): 300-302.
- [2] US Department of Energy. Quadrennial Technology Review report, vol. II Technology Assessments (US Department of Energy, 2015).
https://energy.gov/sites/prod/files/2015/09/f26/Quadrennial-Technology-Review-2015_0.pdf
- [3] Hossin, Khaled, and Khamid Mahkamov. "Performance Evaluation for a 10 kW Solar Organic Rankine Cycle Power System to Operate in the UK Climate Conditions." *The European Conference on Sustainability, Energy & the Environment 2015 Official Conference Proceedings*.
http://papers.iafor.org/papers/ecsee2015/ECSEE2015_15907.pdf
- [4] Y. Hua, M. Oliphant and E. J. Hu, "Development of renewable energy in Australia and China: A comparison of policies and status," *Renewable Energy*, vol. 85, pp. 1044-1051, 2016.

- [5] R. A. Kerr, "Is battered arctic sea ice down for the count?," *Science*, vol. 318, pp. 33-34, 2007.
- [6] X. Zhou, F. Wang and R. M. Ochieng, "A review of solar chimney power technology," *Renewable and Sustainable Energy Reviews*, vol. 14, p. 2315–2338, 2010.
- [7] K.-H. Kim, S. A. Jahan and E. Kabir, "A review on human health perspective of air pollution with respect to allergies and asthma," *Environment international*, vol. 59, pp. 41-52, 2013.
- [8] F. Caiazzo, A. Ashok, I. A. Waitz, S. H. Yim and S. R. Barrett, "Air pollution and early deaths in the United States. Part I: Quantifying the impact of major sectors in 2005," *Atmospheric Environment*, vol. 79, pp. 198-208, 2013.
- [9] A. Buttler, F. Dinkel, S. Franz and H. Spliethoff, "Variability of wind and solar power—An assessment of the current situation in the European Union based on the year 2014," *Energy*, vol. 106, pp. 147-161, 2016.
- [10] X. Zhou, F. Wang and R. M. Ochieng, "A review of solar chimney power technology," *Renewable and Sustainable Energy Reviews*, vol. 14, p. 2315–2338, 2010.
- [11] Padki, M. M., and S. A. Sherif. "On a simple analytical model for solar chimneys." *International Journal of Energy Research* 23, no. 4 (1999): 345-349.
- [12] Yan, M. Q., S. A. Sherif, G. T. Kridli, S. S. Lee, and M. M. Padki. "Thermo-fluid analysis of solar chimneys." In *Industrial Applications of Fluid*

- Mechanics-1991. Proceedings of the 112th ASME winter annual meeting, Atlanta, GA, pp. 125-130. 1991.
- [13] Schlaich, J., R. Bergermann, W. Schiel, and G. Weinrebe. "Design of commercial solar updraft tower systems-Utilization of solar induced convective flows for power generation." *Journal of Solar Energy Engineering-Transactions of The ASME* 127, no. 1 (2005): 117-124.
- [14] H. Kreetz, *Theoretische Untersuchungen und Auslegung eines temporären Wasserspeichers für das Aufwindkraftwerk*, Berlin: Technical University Berlin, 1997.
- [15] A. B. Kasaeian, S. Molana, K. Rahmani and D. Wen, "A review on solar chimney systems," *Renewable and Sustainable Energy Reviews*, vol. 67, pp. 954-987, 2017.
- [16] J. P. Pretorius, *Optimization and control of a large-scale solar chimney power plant*, Stellenbosch: University of Stellenbosch, 2007.
- [17] Putkaradze, Vakhtang, Peter Vorobieff, Andrea Mammoli, and Nima Fathi. "Inflatable free-standing flexible solar towers." *Solar Energy* 98 (2013): 85-98.
- [18] Vorobieff, Peter, Andrea Mammoli, Nima Fathi, and Vakhtang Putkaradze. "Free-standing inflatable solar chimney: experiment and theory." *Bulletin of the American Physical Society* 59 (2014).
- [19] Nima Fathi, Peter Vorobief, Seyed Sobhan Aleyasin. "V&V Exercise for a Solar Tower Power Plant." *ASME Verification and Validation Symposium* (2014).

<https://cstools.asme.org/csconnect/FileUpload.cfm?View=yes&ID=44167>

- [20] G. Manente, S. Rech and A. Lazzaretto, "Optimum choice and placement of concentrating solar power technologies in integrated solar combined cycle systems," *Renewable Energy*, vol. 96, pp. 172-189, 2016.
- [21] Forsberg, Charles W. "Sustainability by combining nuclear, fossil, and renewable energy sources." *Progress in Nuclear energy* 51, no. 1 (2009): 192-200.
- [22] Forsberg, Charles, Lin-wen Hu, Per Peterson, and Kumar Sridharan. Fluoride-salt-cooled high-temperature reactor (FHR) for power and process heat. No. DOE/NEUP-11-3272; MIT-ANP-TR-157. Massachusetts Inst. of Technology (MIT), Cambridge, MA (United States), 2015.
- [23] Conklin, James C., and Charles W. Forsberg. "Base-Load and Peak Electricity from a Combined Nuclear Heat and Fossil Combined-Cycle Plant." In *Proceedings of GLOBAL 2007 conference on advanced nuclear fuel cycles and systems*. 2007.
- [24] Zohuri, Bahman, and Nima Fathi. *Thermal-hydraulic analysis of nuclear reactors*. Springer International Publishing Switzerland., 2015.
- [25] Nikonowicz, Lukasz Bartosz, and Jaroslaw Milewski. "Virtual Power Plants-general review: structure, application and optimization." *Journal of Power Technologies* 92, no. 3 (2012): 135.

- [26] Guerrero, Josep M., L. Garcia De Vicuna, José Matas, Miguel Castilla, and Jaume Miret. "A wireless controller to enhance dynamic performance of parallel inverters in distributed generation systems." *IEEE Transactions on power electronics* 19, no. 5 (2004): 1205-1213.
- [27] Marnay, Chris, Giri Venkataramanan, Michael Stadler, Afzal S. Siddiqui, Ryan Firestone, and Bala Chandran. "Optimal technology selection and operation of commercial-building microgrids." *IEEE Transactions on Power Systems* 23, no. 3 (2008): 975-982.
- [28] Pensini, Alessandro, Matthew Robinson, Nicholas Heine, Michael Stadler, and Andrea Mammoli. "Assessment of grid-friendly collective optimization framework for distributed energy resources." In *Power and Energy Society General Meeting (PESGM), 2016*, pp. 1-5. IEEE, 2016.
- [29] Ming, Tingzhen, Wei Liu, Yuan Pan, and Guoliang Xu. "Numerical analysis of flow and heat transfer characteristics in solar chimney power plants with energy storage layer." *Energy Conversion and Management* 49, no. 10 (2008): 2872-2879.
- [30] Fathi, Nima, Seyed Sobhan Aleyasin, and Peter Vorobieff. "Numerical-analytical assessment on Manzanares prototype." *Applied Thermal Engineering* 102 (2016): 243-250.
- [31] Wilcox, David C. *Turbulence modeling for CFD*. Vol. 2. La Canada, CA: DCW industries, 1998.

- [32] Fathi, Nima, Patrick McDaniel, Charles Forsberg, and Cassiano de Oliveira. "Nuclear Systems for a Low Carbon Electrical Grid." In 2016 24th International Conference on Nuclear Engineering, pp. V001T03A007-V001T03A007. American Society of Mechanical Engineers, 2016.
- [33] Wilson, David Gordon, and Theodosios Korakianitis. "The design of high-efficiency turbomachinery and gas turbines." MIT press, 2014.
- [34] Walsh, Philip P., and Paul Fletcher. Gas turbine performance. John Wiley Sons, 2004.
- [35] Seager, Richard, Haibo Liu, Naomi Henderson, Isla Simpson, Colin Kelley, Tiffany Shaw, Yochanan Kushnir, and Mingfang Ting. "Causes of increasing aridification of the Mediterranean region in response to rising greenhouse gases." *Journal of Climate* 27, no. 12 (2014): 4655-4676.
- [36] US Energy Information Administration. "Levelized Cost and Levelized Avoided Cost of New Generation Resources in the Annual Energy Outlook 2017." AEO2017 Levelized Costs (2017).
https://www.eia.gov/outlooks/aeo/pdf/electricity_generation.pdf
- [37] Lovering, Jessica R., Arthur Yip, and Ted Nordhaus. "Historical construction costs of global nuclear power reactors." *Energy Policy* 91 (2016): 371-382.
- [38] Harris, Grant, Phil Heptonstall, Robert Gross, and David Handley. "Cost estimates for nuclear power in the UK." *Energy Policy* 62 (2013): 431-442.
- [39] Schlissel, David, and Bruce Biewald. "Nuclear power plant construction costs." Synapse Energy Economics Inc (2008): 2008-07.

[40] Schlaich, Jorg, Rudolf Bergermann, Wolfgang Schiel, and Gerhard Weinrebe.

”Design of commercial solar updraft tower systems—utilization of solar induced convective flows for power generation.” *Journal of Solar Energy Engineering* 127, no. 1 (2005): 117-124.

Chapter 5

Power Cycle Assessment of Combined Clean Energy Systems¹

The intermittency of renewable power generation systems on the low carbon electric grid can be alleviated by using nuclear systems as quasi-storage systems. Nuclear Air-Brayton systems can produce and store hydrogen when electric generation is abundant and then burn the hydrogen by Co-Firing when generation is limited. The rated output of a nuclear plant can be significantly augmented by Co-Firing. The incremental efficiency of hydrogen to electricity can far exceed that of hydrogen in a stand-alone gas turbine. Herein we simulate and evaluate this idea on a 50 MW small modular liquid metal/molten salt reactor. Considerable power increases are predicted for Nuclear Air-Brayton systems by Co-Firing with

¹Originally to be published as : N. Fathi, P. McDaniel, C. Forsberg, C. de Oliveira, “Power Cycle Assessment of Nuclear Systems, Providing Energy Storage for Low Carbon Grids,” *Journal of Nuclear Engineering and Radiation Science*, 2017.

hydrogen before the power turbine ².

Nomenclature

Variables

T temperature, K

p pressure

Subscripts

a air

w water

Acronyms

$GTCC$ Gas turbine combined cycle

$HRSG$ Heat Recovery Steam Generator

HTE High-temperature electrolysis

$NACC$ Nuclear Air-Brayton Combined Cycle

$NARC$ Nuclear Air-Brayton Recuperated Cycle

RIC Recuperator and intercooler

SCO_2 Supercritical Carbon Dioxide

TIT Turbine Inlet Temperature

²Some parts of this chapter were published as a technical paper at ASME ICONEO24 proceedings in 2016 as : Fathi, Nima, Patrick McDaniel, Charles Forsberg, and Cassiano de Oliveira. "Nuclear Systems for a Low Carbon Electrical Grid." In 2016 24th International Conference on Nuclear Engineering, pp. V001T03A007-V001T03A007. American Society of Mechanical Engineers, 2016.

5.1 Introduction

5.1.1 Motivation and Background

As the US moves toward a low carbon electrical grid, the only power sources that will be available to any great extent will be the renewables, solar and wind, and the dispatchable, nuclear. For these three types of sources to provide a stable grid, a strategy must be developed for them to work together. The intermittent characteristics of solar and wind sources require that an energy storage system be developed that can smooth the differences between power production and power demand. One possible solution is a nuclear component that develops its own storage. There will clearly be times when a solar system is incapable of generating power. The same is true of a wind system. At those times it would be very useful to have nuclear systems on line. Of course when the sun is shining and the wind is blowing, nuclear systems may not be needed. This poses a dilemma for nuclear systems as they produce very little revenue when shut down. Quite simply the electric grid needs an energy storage system, and it needs to be flexible. Here we describe several nuclear power systems that can meet this need. The total system has multiple components (Fig. 5.1). The reactor provides heat to the power cycle—the subject of this paper. The reactor operates at base load. The system can operate at base-load on nuclear heat. To produce peak power, hydrogen is added to the compressed air after nuclear heating in the power cycle to raise temperatures and power levels. At times of low electricity demand, electricity from the grid is fed to a High-Temperature Electrolysis (HTE) system to produce

hydrogen. Hydrogen is stored and used as fuel for peak electricity production. Hydrogen as a storage system has the advantage of low-cost storage using the same underground storage technologies as used for natural gas. However, the challenge is round-trip efficiency of electricity to hydrogen to electricity. HTE is the most efficient method to produce hydrogen. A Nuclear Air-Brayton cycle (described herein) is the most efficient method to convert hydrogen to electricity. This combination creates new options for using hydrogen for energy storage.

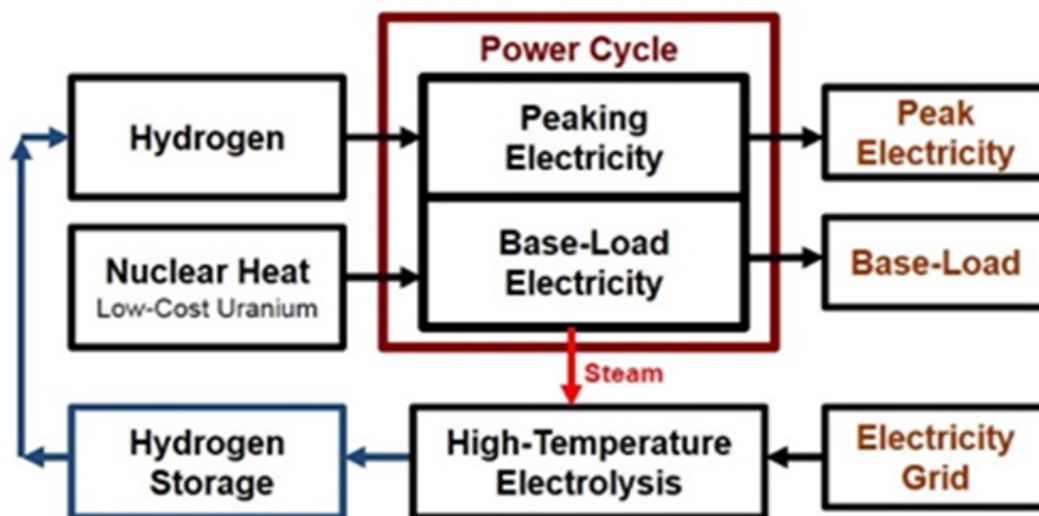


FIGURE 5.1: System description

5.1.2 Technical Approach

A nuclear system is needed to store energy when its production is not needed and recover that energy when it is needed to augment the nuclear system's baseload capability. One possible solution to this challenge is to develop a Nuclear Air-Brayton Combined Cycle (NACC) system. The standard Gas Turbine Combined

Cycle (GTCC) would be modified to use nuclear energy rather than chemical energy. This can be accomplished by replacing the gas turbine combustion chamber with a heat exchanger. A nuclear driven heat exchanger cannot reach the high temperatures that current gas turbine combustion chambers do as it requires a temperature drop from its walls to the working fluid (air) rather than a temperature drop from the working fluid to the walls of the chamber. However, there are compensating benefits. In particular a heat exchanger can be built with a smaller pressure drop in the working fluid, and the air can be heated multiple times. Heating the working fluid multiple times is very common in steam systems. Since this is an advanced concept and system performance is always better at peak cycle temperatures, only liquid metal systems and molten salt systems have been considered for this study. High temperature gas systems could also be considered, but the cycles would look enough different that they need to be analyzed in a different fashion. It is also possible to develop a Nuclear Air-Brayton Recuperated Cycle (NARC) system with an intercooler using either water ($NARC_w$) or air ($NARC_a$) to cool the intercooler. Liquid metal and molten salt heat exchangers were developed in the 1960's for the Aircraft Nuclear Propulsion program and performed quite well [1]. Sodium to air heat exchangers were used on the Fast Flux Test Facility to dump the heat generated in the nuclear core. Currently there are designs to use sodium-to-air heat exchangers for safety heat dumps on sodium fast reactors. Apparently such heat exchangers are not as complicated as sodium-to-water heat exchangers and do not have some of the severe safety issues [2]. The system of interest is described in Fig. 5.2. It is an open cycle Air-Brayton topping cycle mated to a Steam-Rankine bottoming cycle similar to

most Gas Turbine Combined Cycles. The Brayton system consists of one or two compressors and three gas turbines followed by a Heat Recovery Steam Generator (HRSG). The HRSG drives three steam turbines in the bottoming cycle. To improve the normal operating efficiency of the system a recuperator can be included after the HRSG. If this is done, an intercooler can also be included between the two compressors.

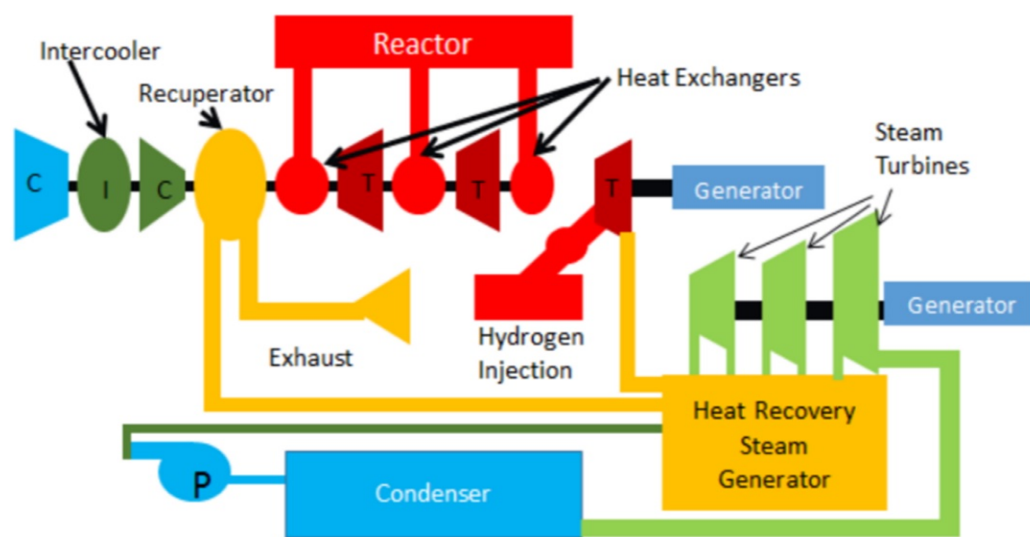


FIGURE 5.2: Schematic presentation complete nuclear Air-Brayton combined cycle with recuperator and intercooler

The recuperator is required to take advantage of the efficiency improvements provided by the intercooler. Three gas turbines with three reheat cycles were chosen as this system performs better than the two gas turbine system and very close to the performance of four gas turbines. The three gas turbines consist of two turbines connected directly to the compressor(s) and a power (or free) turbine connected only to the driven electrical generator. The system has three heat exchangers, one before each turbine. The power turbine approach seems to perform slightly better than a system with all three turbines, the compressor(s), and the generator

on the same shaft. The turbines for the steam system can be connected to the same shaft as the power turbine or to a separate shaft driving a second generator. The basic cycle without the recuperator and intercooler (RIC) has been identified as a NACC. When RIC is added it is identified as a NACC&RIC. Since the RIC seemed to make the combined cycle more efficient, a system was considered that did not include the bottoming cycle with the turbine exhaust going directly to the recuperator. This system has been identified as a $NARC_w$ or $NARC_a$. The calculated efficiency of each of the three systems is compared with the Supercritical Carbon Dioxide (SCO_2) system [3] under study by DOE in Fig. 5.3.

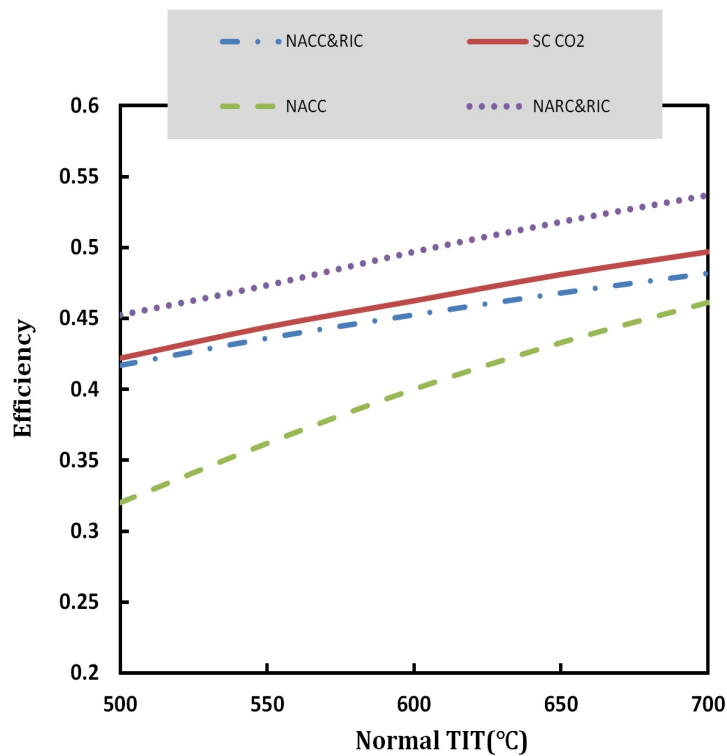


FIGURE 5.3: Cycle Efficiencies for NACC, SCO_2 , NACC&RIC and NARC

The basic NACC system is significantly less efficient than SCO_2 system when both operate at a Turbine Inlet Temperature (TIT) of 500 °C, typical sodium

reactor output temperatures [4], but improves significantly as temperatures approach those expected from molten salt reactors [5]. Adding the recuperator and intercooler brings the performance of the NACC&RIC system up considerably at the lower temperatures. It appears that the $NARC_w$ system outperforms all three on an efficiency basis. Typical compressor pressure ratios for the NACC and NACC&RIC systems are given in Fig. 5.4. Adding the recuperator lowers system operating pressure as expected. This would work as follows. The nuclear reactor system would operate continuously in somewhat of a baseload fashion. When the sun is shining and the wind is blowing, the electricity produced by the nuclear system will be used to produce and store hydrogen by high temperature electrolysis [6]. Any excess electricity produced by the renewables could also be diverted to produce and store hydrogen. When the sun goes down and the wind stops blowing the nuclear system will produce the electricity required to meet the grid's demands. In addition to the rated nuclear plant output, the stored hydrogen can also be burned in a combustion chamber and its exhaust fed to the power turbine to "superheat" the airflow. This process is called Co-Firing. Augmentation of the nuclear system's output in this fashion is the purpose for considering NACC and NARC systems as a type of energy storage mechanism for the grid of the future. Other energy storage mechanisms have been proposed that may be more efficient than producing and storing hydrogen, such as heating firebricks electrically and recovering the energy by flowing the air over the firebricks prior to entering the nozzle for the power turbine [7]. Only the hydrogen production and burning scheme will be considered here. Of course NACC/NARC systems have other advantages than advanced efficiencies and serving as a grid energy storage

mechanism. They will take advantage of the broad manufacturing base of gas turbine components and technology. And they will significantly reduce the water requirements for waste heat removal, reducing such requirements by at least a factor of two, compared to current LWR's. But the focus here is on the energy storage mechanism.

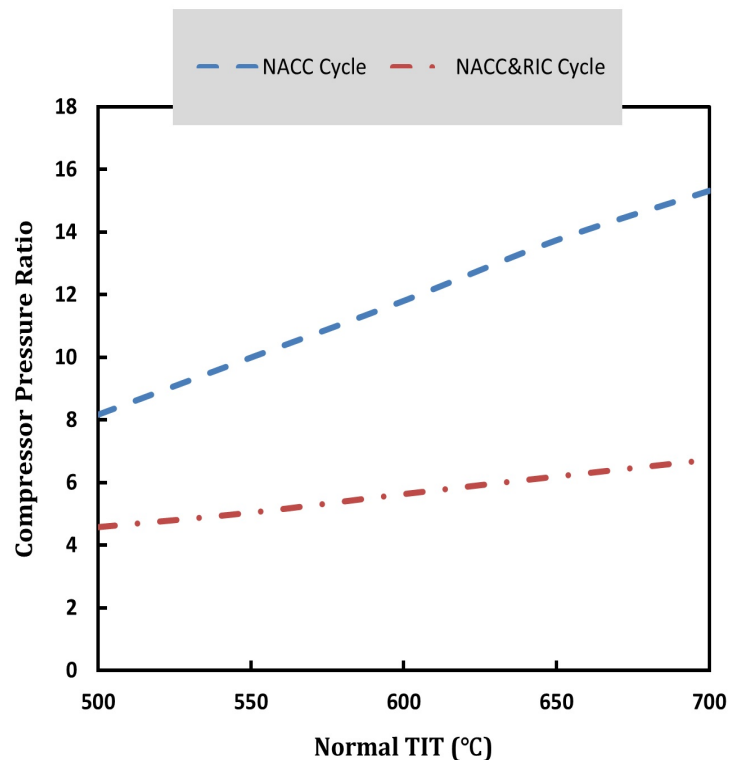


FIGURE 5.4: Compressor Pressure Ratios

5.1.3 Modeling Approach

The goal of this effort has been to develop models that will enable us to identify the characteristics of optimal systems. Once the optimal systems have been identified, then a search can be undertaken for off-the-shelf components that come close to meeting the requirements of an optimal system. If no such components exist, then a development need has been identified, and specific requirements can be

set. There exist a number of cycle analysis codes that can address NACC/NARC systems such as ThermoLib, ThermoFlex, and AspenTech. Many of our results have been checked against ThermoLib, but it was desirable to build a code that would allow not only cycle calculations but also sizing estimates and possibly a bottom up economic analysis. The cycle modeling follows the techniques described in [8–10]. Size estimates for turbomachinery follow the scaling parameters given as in [11]. Heat exchanger sizes are calculated based on preliminary designs. Air compressor and turbine polytropic efficiencies follow the published scaling rules [8]. Steam turbines were simply set at a 90% isentropic efficiency. All heat exchangers were designed to meet a 1% pressure drop and a 95% effectiveness. Recuperators and intercoolers are counterflow, and all other heat exchangers are cross flow. A pinch point temperature difference of 10° was baselined. Predicted efficiencies have been compared against currently published data for Gas Turbine Combined Cycles and agree very closely [12, 13].

5.2 NACC Scenarios Analyzed

The objective of this effort was to analyze the impact of Co-Firing the power turbine of a NACC system with a hydrogen burn to augment its power output. Since the normal turbine inlet temperatures produced by a liquid metal or molten salt heat exchanger are well below typical gas turbine inlet temperatures, two burn temperatures were chosen as being of interest. The first was 927° which corresponds to the peak temperature that uncooled turbine blades are advertised to withstand [8]. The second was 1427°, the temperature advertised as the peak that

GE H series turbines can achieve [14]. Clearly the nuclear heated only systems can operate with uncooled turbine blades. If they can operate with cooled blades without the cooling air losses at reactor outlet temperatures, then it is worth considering Co-Firing at the 1427° limit. At the 1427° limit, it may well be necessary to require ceramic heat exchangers for the HRSG and its superheaters. Estimated HRSG inlet temperatures in this case are about 1154°. It should also be pointed out that the power turbine in all cases will have to be fed by a variable area nozzle to accommodate the higher temperature gas and maintain input pressure and mass flow rate. The operating pressures in the steam bottoming cycles were held constant between the normal operating conditions and the Co-Firing environment. This was done to eliminate one control variable in the analysis. It may be useful to address this restriction in the future. The near optimum pressure for the NACC system was 9 MPa, and the near optimum pressure for the NACC&RIC system was set at 12 MPa. The NACC efficiency improves slightly at lower pressures, and the NACC&RIC improves slightly at higher pressures due to higher temperature air reaching the recuperator. But the improvements in performance are not significant, and these two pressures are in the range of current GTCC systems.

The power level chosen for this study was 50 MW(e), typical of some Small Modular Reactors currently being considered. For both systems (NACC and NACC&RIC) the Brayton air cycle produced about 70% of the power, and the Rankine steam cycle produced 30% of the power at rated power output. A crucial parameter of interest is the ratio of the mass flow rate of steam to the mass flow rate of air. For the NACC system this ratio was about 3% at 500° and 6% at 700°.

For the NACC&RIC system it was approximately 1% lower at all temperatures. Normal turbine inlet temperatures (TIT) are used to characterize the systems analyzed as they can easily be related to the technology involved.

5.3 NACC with only Co-Firing

For both the NACC and NACC&RIC systems there are several design strategies that can be pursued. Consider first the NACC system. For this system there are no downstream temperature limitations. So when the gas exiting the power turbine is routed to the HRSG, the entry temperature for the 927° power turbine inlet temperature is 763°, and the HRSG exit temperature is 277° if the normal turbine inlet temperature is 500°. The pinch point temperature difference is 348°. For this power turbine inlet temperature when the normal turbine inlet temperature is 700° the HRSG inlet temperature is 666 ° and the exit temperature is 405°. The pinch point temperature difference is now 163°. The increase in power as a result of the hydrogen Co-Firing is given in Fig. 5.5 for both the 927° and 1427° cases.

At a normal 500° TIT, the power goes up about 55% when Co-Fired to 927° and more than doubles at 1427°. The hydrogen is burned with an efficiency of between 20% and 32% for both the 927° case and the 1427° case. This low efficiency occurs because the temperature drop between the air and the steam in the evaporator is quite large. The pinch point temperature difference goes from 10° to 153°. This is a major penalty and probably not a reasonable method of operation. The

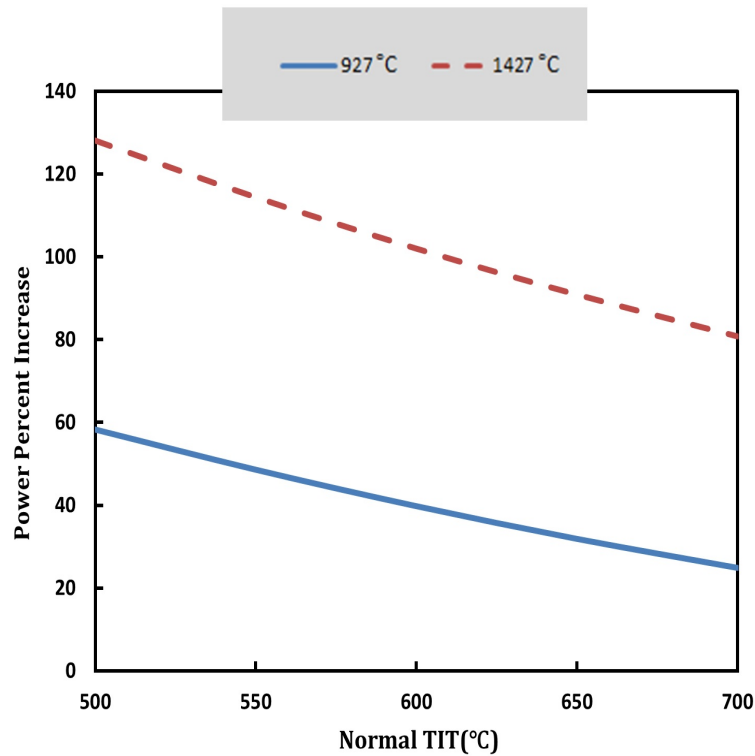


FIGURE 5.5: Power increase due to Co-Firing at normal steam flow rates

efficiency of the hydrogen burn is improved significantly with other designs, as shown.

5.4 NACC with Co-Firing and Increased Steam Flow

The large pinch point temperature differences with simple Co-Firing imply a large increase in irreversibility or exergy. The easiest way to bring the pinch point temperature difference back down to a more efficient case (10°) is to increase the steam flow in the bottoming cycle. This would imply that during normal operation the bottoming cycle would operate at flow rates significantly less than maximum.

The loss in efficiency for operating in this manner has not been calculated. However, since the steam system only produces 30% of the total power during normal operation the loss in efficiency will be mitigated. Fig. 5.6 describes the increase in steam flow required to lower the pinch point temperature difference to its value before Co-Firing.

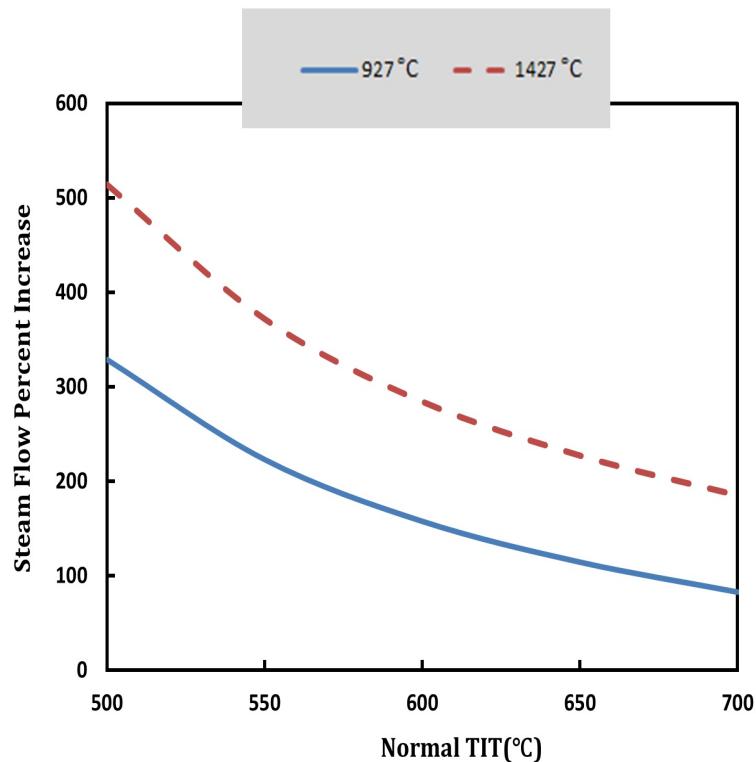


FIGURE 5.6: Increase in steam flow to maintain pinch point for the NACC system

At a 500° nominal TIT the increase in steam flow is 300% for 927° and 500% for 1427°. This means the normal bottoming system would be running at 25% of maximum if a 927° burn is desired and at 17% of maximum if a 1427° burn is desired.

However the increase in power is significant as described in Fig. 5.7. For the normal 500° TIT case the power can be increased by 200% for a burn at 927° and

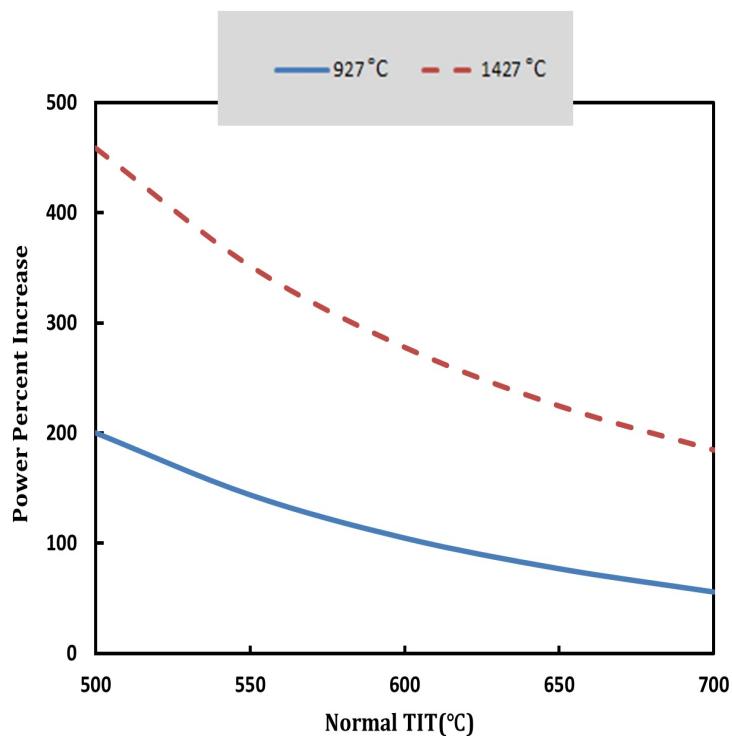


FIGURE 5.7: Power increase for NACC if the pinch point temperature difference is held constant.

450% at 1427°. At a normal 700° TIT the increases are not as great, but still very significant - 200% for Co-Firing at 1427° and 100% for 927°. Fig. 5.8 presents the hydrogen burn efficiency for this case.

5.5 NACCRIC with Co-Firing - Maximum Recuperator Temperature Limit

When the recuperator and intercooler are added the normal operation efficiency increases, but it sets a limit on the peak temperature that the recuperator can add to the flow entering the first heat exchanger. No matter how much heat the recuperator adds during Co-Firing, it will affect the heat transferred in the

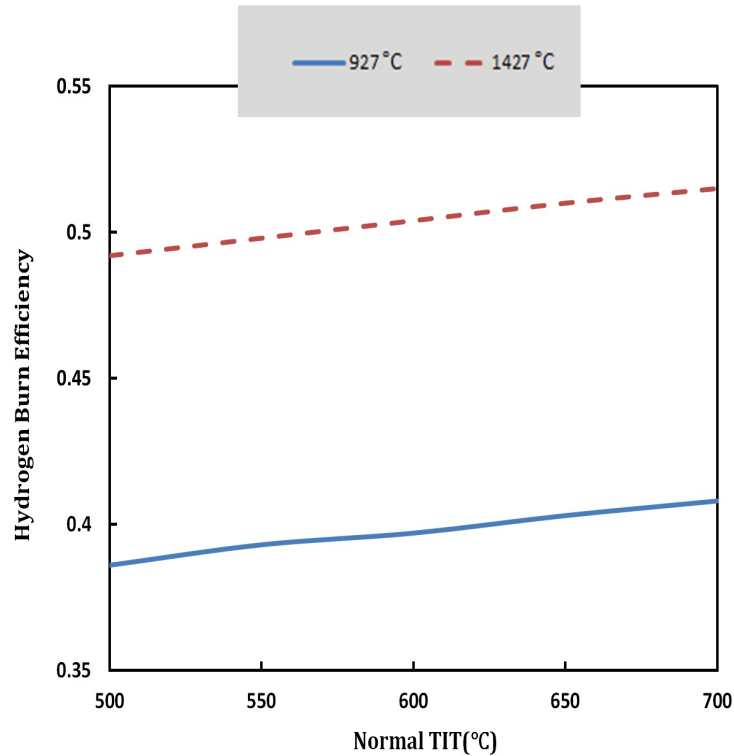


FIGURE 5.8: Hydrogen burn efficiencies when the pinch point temperature difference is constant.

first heat exchanger. The limiting case occurs when the air temperature entering the first heat exchanger reaches the normal TIT. In this case the heat exchanger transfers no heat to the air, and the reactor power must be reduced to compensate for this lack of heat transfer. This doesn't appear to be an impossible condition, but all of the ramifications have not been explored at this time. Therefore the following analysis is based on limiting the hot air out of the recuperator to the normal TIT for the system. This can be accomplished in three ways. First it is possible to limit the burn temperature in the Co-Firing process to less than the maximum. Second it is possible to dump the hot gas going into the recuperator so as to not exceed its output limit. Third it is once again possible to increase the steam flow in the bottoming cycle to pull down the fluid temperature entering the recuperator so that it only transfers enough heat to bring the air flow entering the

first heat exchanger up to its normal TIT. The second option will not be considered as it is obviously a waste of energy.

5.6 Limiting the Co-Firing temperature

The limit on the Co-Firing temperature as a function of the normal system TIT is plotted in Fig. 5.9. The limit is less than 927°, up to about 560°. So at normal system TITs above 560°, the full 927° Co-Firing can be accomplished. The peak Co-Firing temperature for the 700° case is about 1317°, so the 1427° Co-Firing can't be reached even in this case.

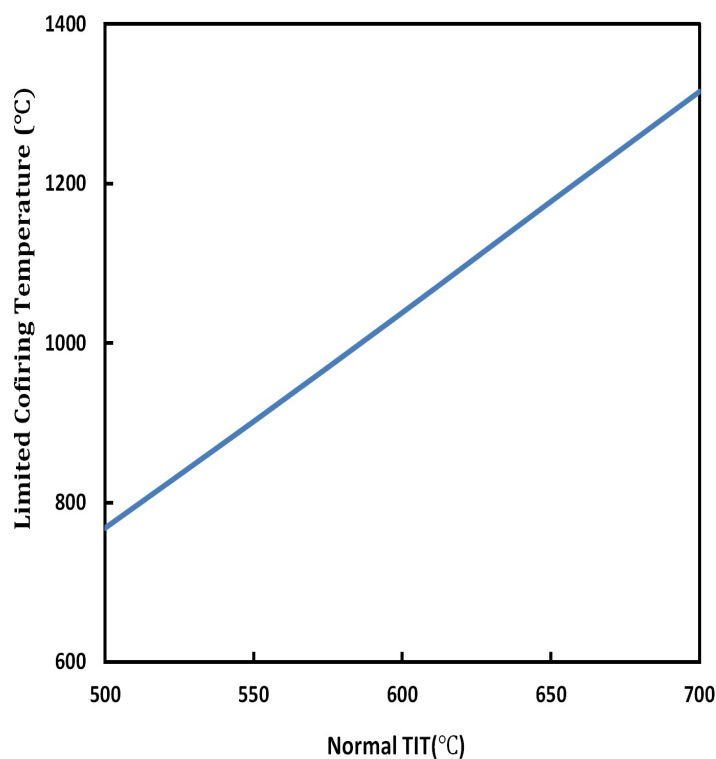


FIGURE 5.9: The maximum Co-Firing temperature allowed to reach the system normal TIT

Fig. 5.10 describes the power increase possible by choosing to limit the maximum Co-Firing temperature as described above. The increase varies from 35% to 70%

as a function of the normal system TIT. Fig. 5.11 presents the required reactor heat output as a function of its rated power during Co-Firing at the maximum allowed temperature.

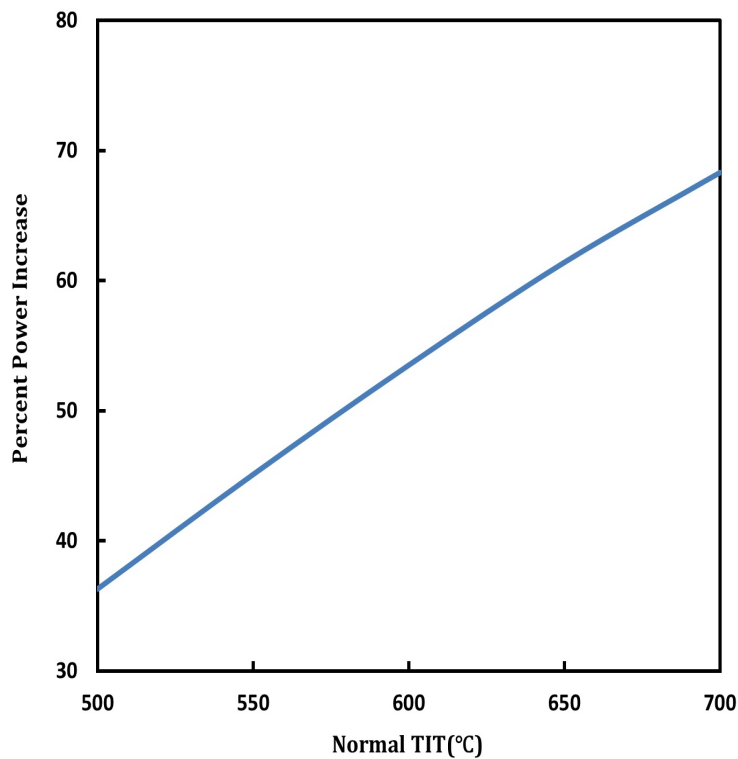


FIGURE 5.10: Power increase allowed by Co-Firing at the maximum allowed temperature

The reactor power must be reduced because the first heat exchanger is no longer transferring heat to the air. Fig. 5.12 presents the hydrogen burn efficiency for this case. Note that the efficiency for this case is significantly greater than those for the basic NACC system and 10 to 15% greater than any achieved by current Gas Turbine Combined Cycle systems.

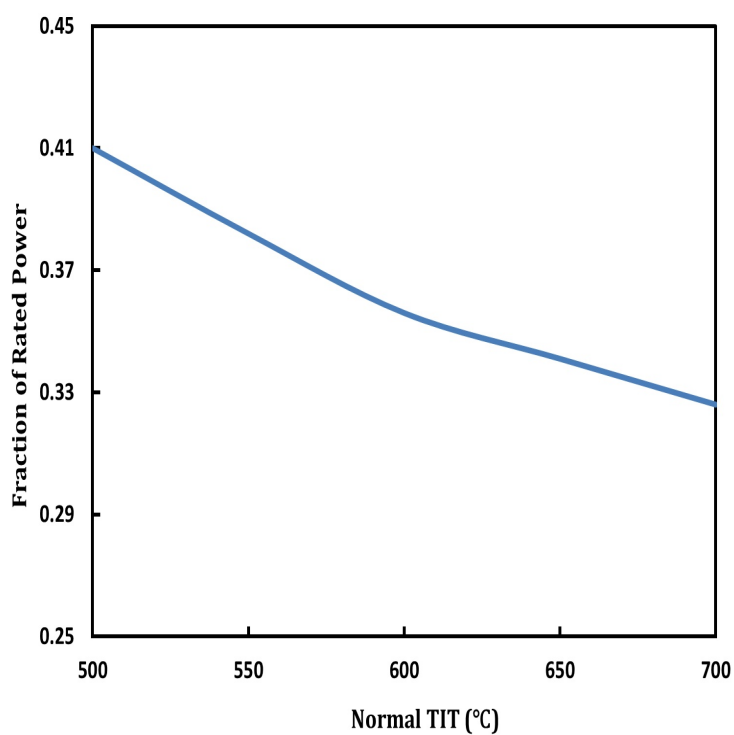


FIGURE 5.11: The required fraction of rated power for the reactor when Co-Firing at maximum temperature

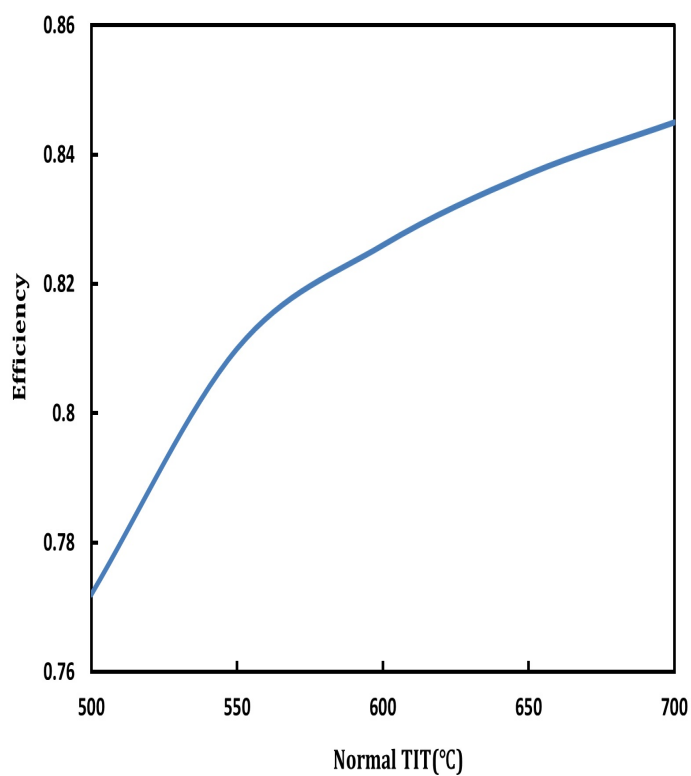


FIGURE 5.12: Hydrogen burn efficiency at the maximum Co-Firing temperature

5.7 NACCRIIC with Co-Firing - Increased Steam

Flow to Meet Recuperator Temperature Limit

The steam flow in the bottoming cycle can be increased to limit the temperature out of the recuperator to the normal operating TIT similar to the way it was for the NACC system. In this case it is not the pinch point temperature difference that matters, but rather the recuperator outlet temperature entering the first heat exchanger. Fig. 5.13 plots the required increase in steam flow to limit the recuperator outlet temperature. Note that for normal system TITs above about 560°, the steam flow does not have to be increased for the 927° Co-Firing. The peak increase is about 150% at a system normal TIT of 500°. When Co-Firing a 700° system at 1427° the peak increase in steam flow is about 15%. The increase in power achieved by increasing the steam flow in the bottoming circuit is described in Fig. 5.14.

At the 500° limit increasing the steam flow by 140% increases the power output by slightly over 100% when Co-Firing at 927°. When Co-Firing at 1427° increasing the steam flow by 400%, increases the power output 340%. At the 700° limit, the steam flow does not need to be increased but a 25% increase in output is achieved by Co-Firing at 927°. Co-Firing at 1427° increases the power output 90% for a 15% increase in steam flow. The reactor power requirements are plotted in Fig. 5.15. For the 927° Co-Firing the power requirements decrease with normal system TIT until an increase in steam flow is no longer required. When the increased steam flow is no longer required, the recuperator outlet temperature to the reactor drops

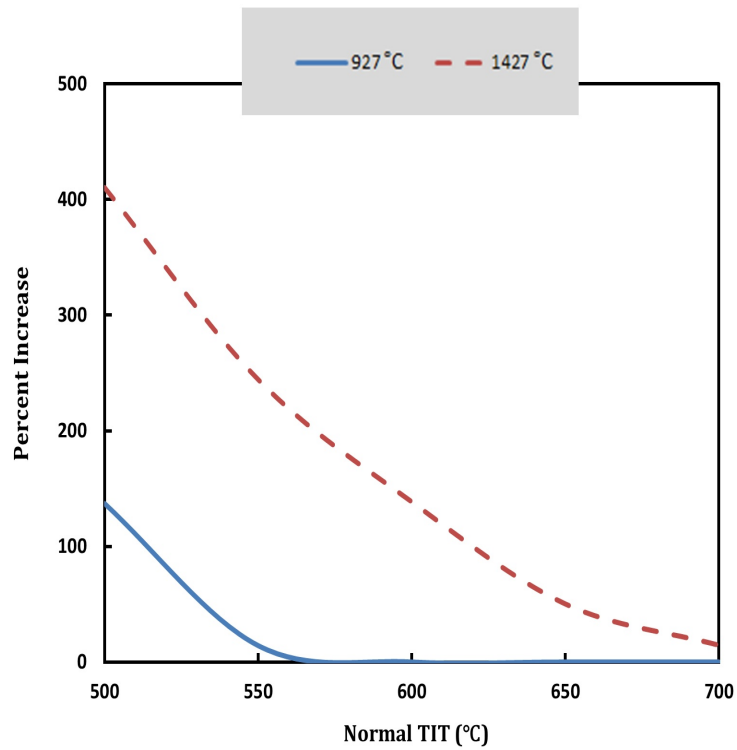


FIGURE 5.13: Increase in steam flow for the recuperator outlet temperature limit

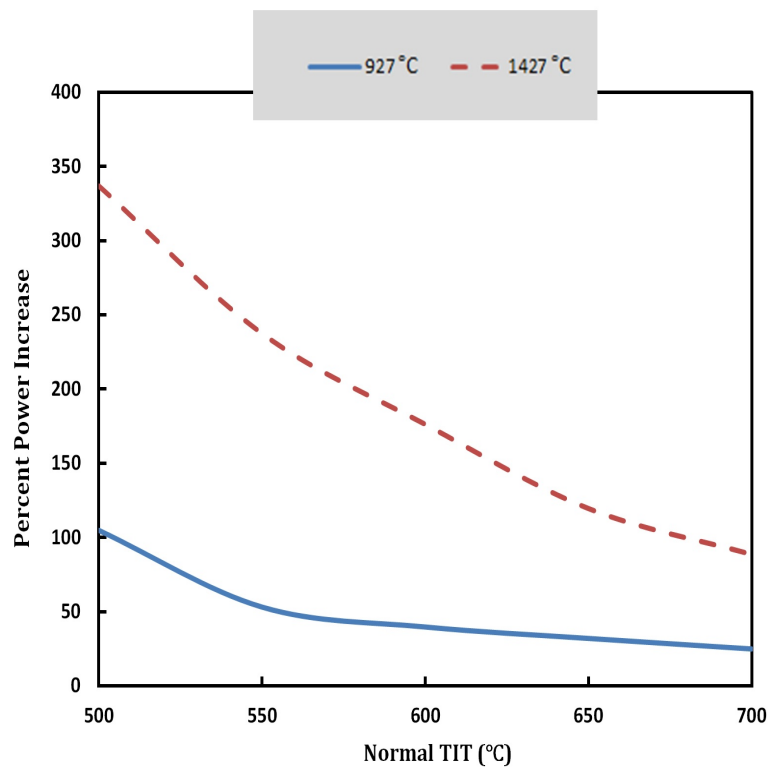


FIGURE 5.14: Percent power increase when the steam flow is increased to reach the maximum recuperator outlet temperature.

and the reactor power must be increased to maintain the nominal system TITs. This causes a rather dramatic increase in reactor power above 550°. When Co-Firing occurs at 1427°, increased steam flow is always required, so the reactor power requirement continuously decreases from about 40% to 30%.

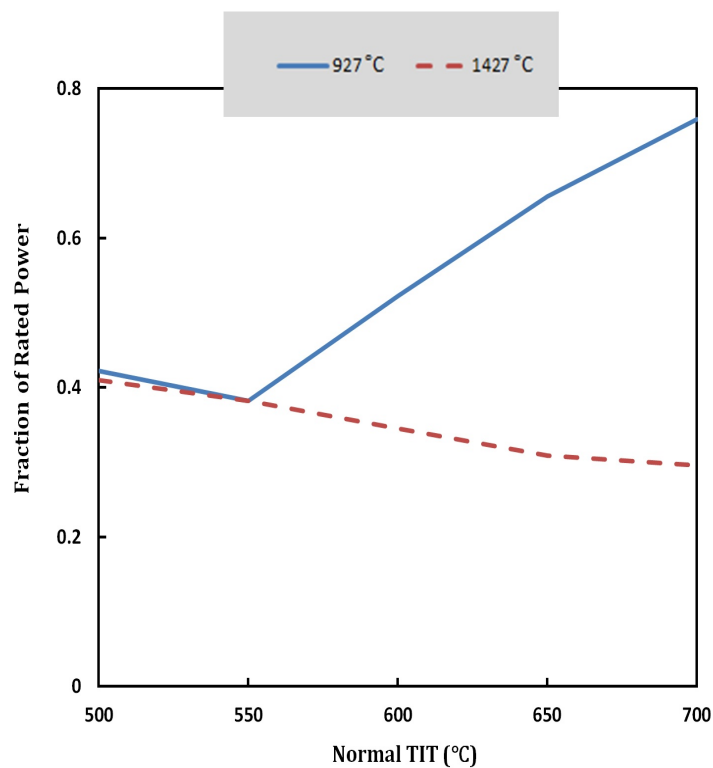


FIGURE 5.15: Required fraction of reactor rated power when Co-Firing with increased steam flow

The efficiency of the hydrogen burn is plotted in Fig. 5.16. For the 927° Co-Firing the efficiency starts at 45% but rapidly rises to over 70% and peaks for the 700° system at almost 90%. This is because the hydrogen is introduced at the normal TIT temperature and must raise the fluid temperature to only 927°. For the 1427° Co-Firing the burn efficiency starts at 47% and eventually increases to over 75% for the 700° system.

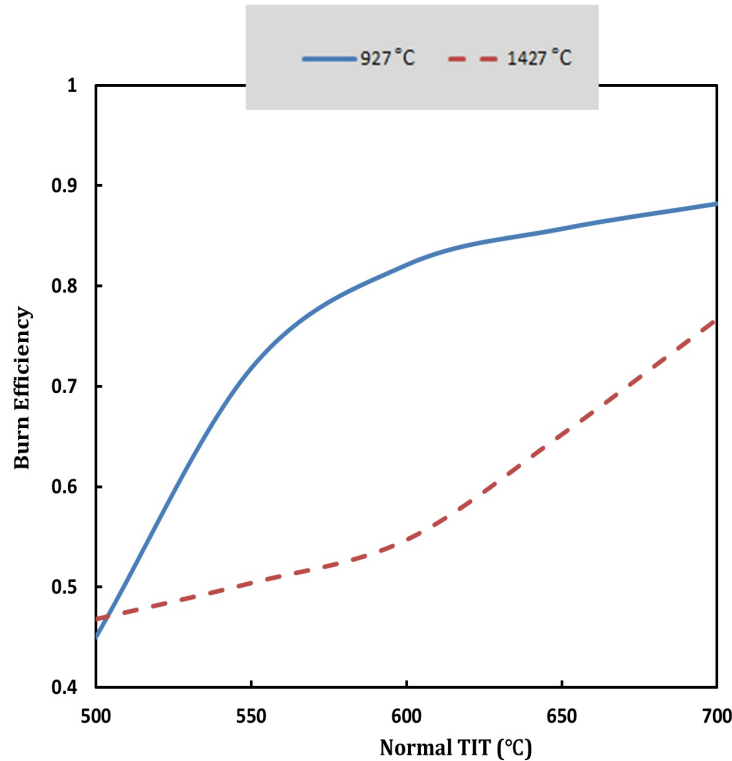


FIGURE 5.16: Hydrogen burn efficiency when steam flow is increased to meet the maximum recuperator outlet temperature.

5.8 NARC Scenarios Analyzed

By dropping the steam bottoming cycle it is possible to build a Nuclear Air Brayton Recuperated (Only) Cycle. With a water cooled intercooler ($NARC_w$) this cycle appears to be the most efficient as plotted in Fig. 5.3. The relative amount of heat that must be dumped to the environment for a NACC&RIC system and a $NARC_w$ system is plotted in Fig. 5.17. The $NARC_w$ system is significantly better than a NACC&RIC system. However it is also possible to build a NARC with an air cooled intercooler ($NARC_a$). These systems will not require any environmental water for a heat dump.

Since the same problem with the exit temperature from the Recuperator not exceeding the system nominal TIT occurs for NARC systems, it is better to set the

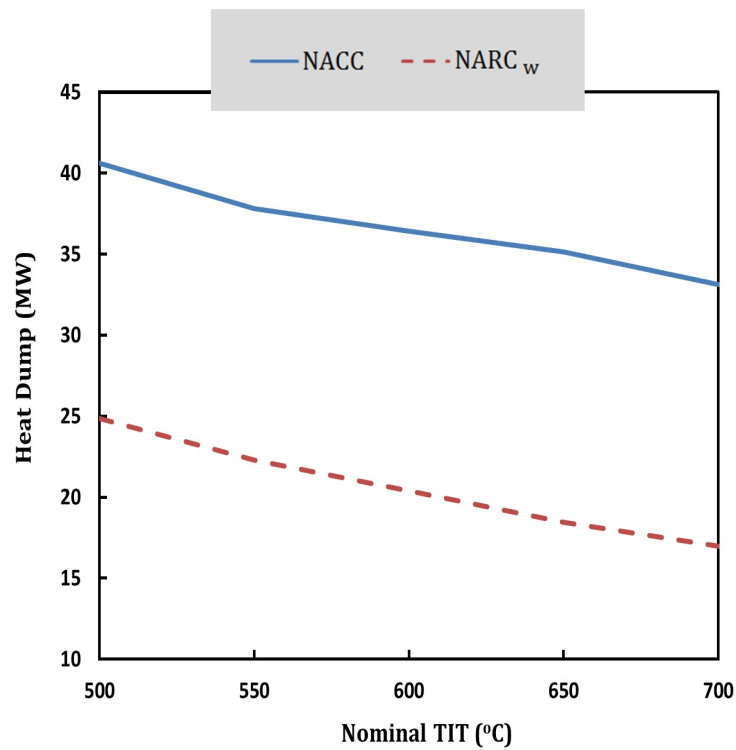


FIGURE 5.17: Comparison of required environmental heat removal by water for NACC&RIC and $NARC_w$ systems

burn temperature for hydrogen augmentation based on this limit. Fig. 5.18 plots the peak burn temperature for this condition. Note that the peak burn temperature in all cases does not significantly exceed the 927° temperature for uncooled turbine blades.

Similar to the case for a NACC system, the hydrogen is burned at a very high efficiency. This data is presented in Fig. 19. In the case of recuperated systems this efficiency is always over 70%. Since instead of producing the hydrogen on site and storing it, natural gas could be burned with a slightly different turbine strategy and achieve a similar efficiency. This means that the most efficient use of natural gas would be to augment a NARC system [15]. Of course this means a larger carbon footprint, but not as large as burning it in a gas turbine of any

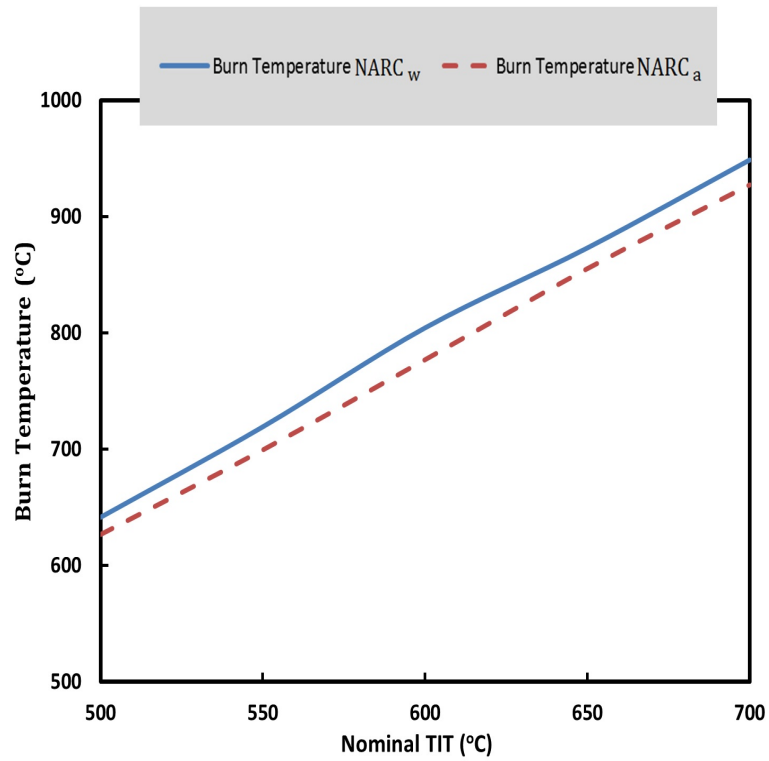


FIGURE 5.18: Recommended peak burn temperatures for NARC systems

variety.

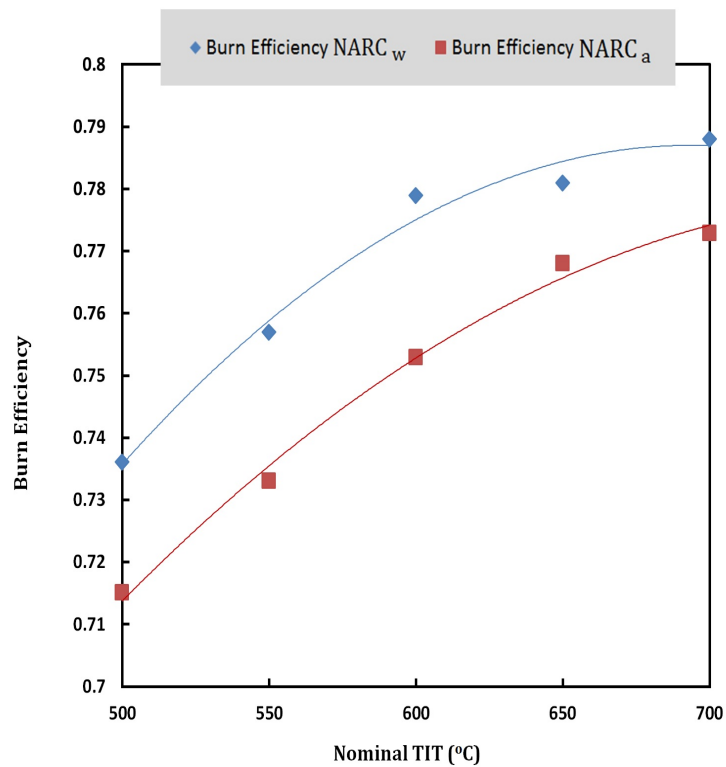


FIGURE 5.19: Hydrogen burn efficiency for NARC systems

The power augmentation due to Co-Firing for NARC systems is not as significant as it is for NACC systems. The power increases are presented in Fig. 5.20: the augmentation varies from about 16% to 26% from low to high nominal TIT. Since the NARC systems do not have the power enhancement capability of the steam bottoming cycle, the gains due to Co-Firing are not as significant. However there is also less concern about efficiencies over the operating range of the steam cycle. The $NARC_a$ is a little less efficient and produces a smaller increase in power during Co-Firing.

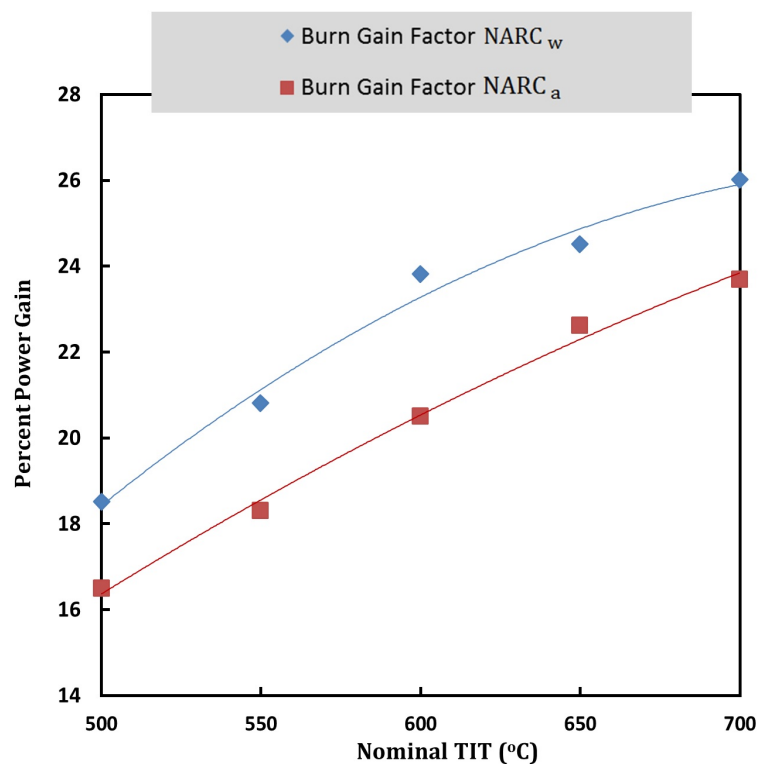


FIGURE 5.20: Percent power augmentation for NARC systems using Co-Firing

Finally it is worth talking about overall system efficiencies during Co-Firing, and the sizes of these Nuclear Air-Brayton systems. The overall efficiency for burning both nuclear and hydrogen fuel for the NACC and both NARC systems is presented

in Fig. 5.21. For the two systems requiring water as a heat dump, the overall efficiency starts at about 50% for 500° and climbs to almost 60% for a 700° system.

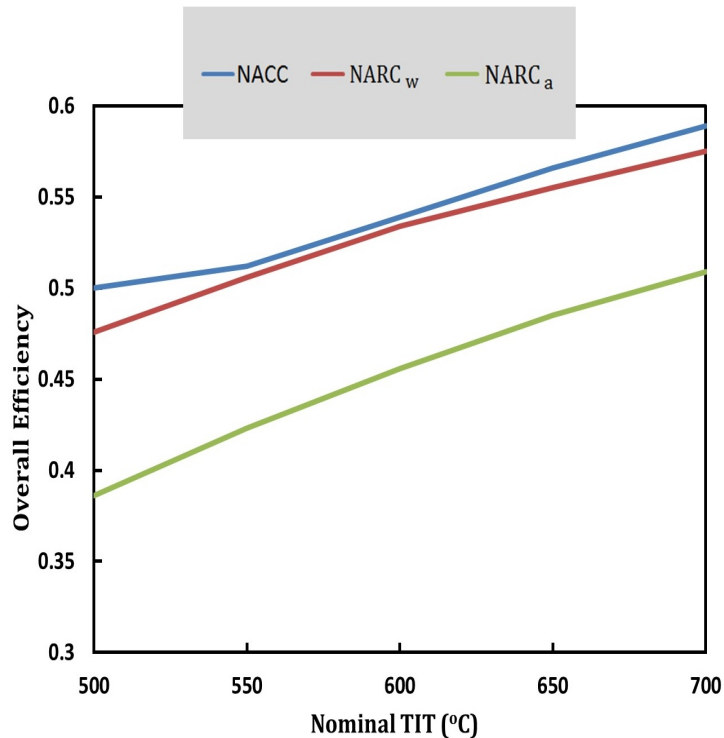


FIGURE 5.21: Overall system efficiencies for the co-fired systems

Estimates of overall system sizes are presented in Fig. 5.22. These are for the nominal 50 MW(e) system. The NACC and $NARC_w$ systems are very comparable in size to the proposed NuScale system, an LWR small modular reactor. $NARC_a$ is significantly larger due to the size required for an air to air intercooler. However it is worth pointing out that this system requires no cooling water source and can be built or installed anywhere in the world.

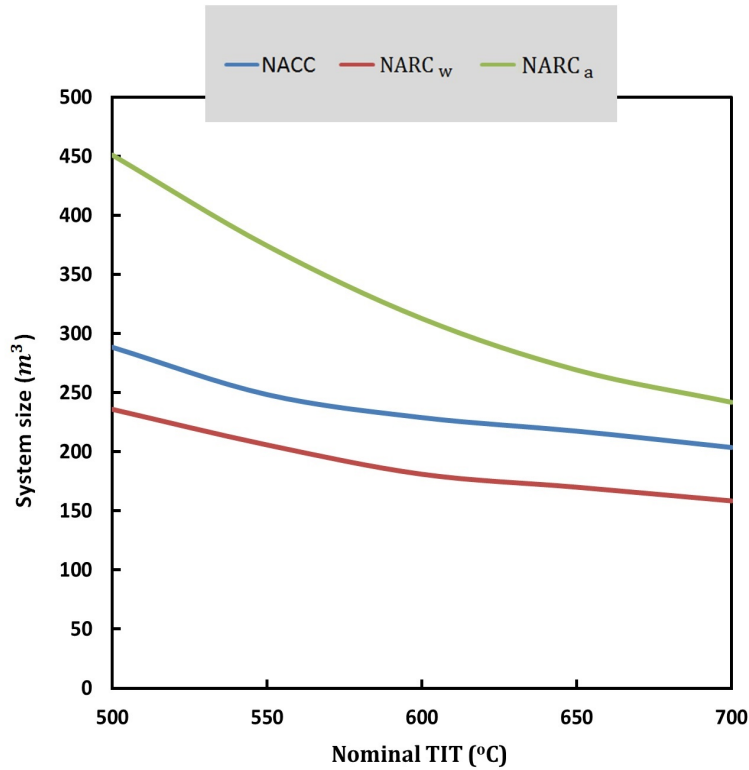


FIGURE 5.22: Estimated system volumes for NACC and NARC systems

5.9 Conclusion

Nuclear power plants can serve the role of energy storage systems for the national electric grids by producing hydrogen when there is an excess of generation due to strong renewable sources and burning the hydrogen to augment their rated capability when renewables are not available. The analysis has been performed for a 50 MW small modular reactor, using sodium/molten salt as a primary coolant. Scale up for a power plant can be accomplished by adding more SMRS or expanding this to a large reactor. Significant power increases can be obtained for Nuclear Air-Brayton systems by Co-Firing with hydrogen before the power turbine. Power increases in the range of 300-400% can be achieved for NACC that systems normally operate at 500° and increases in the range of 100 to 200% for systems normally operating at 700°. The most effective strategy appears to be

increasing the steam flow in the bottoming cycle when Co-Firing. This works for both recuperated and unrecuperated systems. Nuclear Air-Brayton Recuperated (only) systems can achieve higher normal operation efficiencies and comparable overall efficiencies to NACC systems. The power enhancement provided by NARC systems is significantly less, in the range of 20%, but easier to implement. The $NARC_a$ system is significantly larger and has a slightly lower efficiency, but it requires no cooling water to operate. The Air-Brayton power conversion systems provide a very flexible storage capability for a low carbon grid.

5.10 Acknowledgment

Work supported through the INL Laboratory Directed Research Development (LDRD) Program under DOE Idaho Operations Office Contract DE-AC07-05ID14517.

Bibliography

References

- [1] MacPherson, R. E., J. C. Amos, and H. W. Savage. "Development testing of liquid metal and molten salt heat exchangers." *Nuclear Science and Engineering* 8, no. 1 (1960): 14-20.
- [2] Chang, W. P., Y. M. Kwon, H. Y. Jeong, S. D. Suk, and Y. B. Lee. "Inherent safety analysis of the KALIMER under a LOFA with a reduced primary pump halving time." *Nuclear Engineering and Technology* 43, no. 1 (2011): 63-74.
- [3] Dostal, Vaclav, Pavel Hejzlar, and Michael J. Driscoll. "High-performance supercritical carbon dioxide cycle for next-generation nuclear reactors." *Nuclear Technology* 154, no. 3 (2006): 265-282.
- [4] Waltar, Alan Edward, and Albert Barnett Reynolds. "Fast breeder reactors." Alan E. Waltar, Pergamon Press, 1981.
- [5] Forsberg, CW. "Fluoride-salt-cooled High-Temperature Reactor (FHR) Commercial Basis and Commercialization Strategy." MIT-ANPTR-153, Massachusetts Institute of Technology, Cambridge, MA, 2014.

-
- [6] Vitart, X., "Hydrogen Production Through High -Temperature Electrolysis." in Nuclear Production of Hydrogen, ANS Scientific Publications, LaGrange Park IL, (2004).
- [7] Stack, D. C., D. Curtis, R. Ibekwe, and C. Forsberg, "Conceptual Design and Market Assessment of Firebrick Resistance Heated Energy Storage (FIRES) – Avoiding Wind and Solar Electricity Price Collapse to Improve Nuclear, Wind, and Solar Economics." ICAPP 2016, Paper 16622, San Francisco CA, April 17-20, 2016.
- [8] Wilson, David Gordon, and Theodosios Korakianitis. "The design of high-efficiency turbomachinery and gas turbines." MIT press, 2014.
- [9] Kays, William Morrow, and Alexander Louis London. "Compact heat exchangers." (1984).
- [10] El-Wakil, Mohamed Mohamed. "Powerplant technology." Tata McGraw-Hill Education, 1984.
- [11] Walsh, P. P., and P. FLETCHER, "Gas Turbine Performance." Blackwell Science, Oxford UK, (1998).
- [12] Zohuri, Bahman, Patrick J. McDaniel, and Cassiano RR De Oliveira. "Advanced Nuclear Open Air-Brayton Cycles for Highly Efficient Power Conversion." Nuclear Technology 192, no. 1 (2015).
- [13] Zohuri, Bahman, and Nima Fathi. Thermal-hydraulic analysis of nuclear reactors. Springer International Publishing Switzerland., 2015.

- [14] Boyce, Meherwan P. "Gas turbine engineering handbook." Elsevier, 2011.

- [15] Forsberg, Charles, and Daniel Curtis. "Nuclear Air-Brayton Combined Cycle (NACC) With Natural Gas Peak Power." In ASME 2013 Power Conference, pp. V002T08A002-V002T08A002. American Society of Mechanical Engineers, 2013.

Appendix A

List of Achievements of this Research

A.1 Publications

- N. Fathi, S.S. Aleyasin, P. Wayne, P. Vorobieff, “Computational-Experimental Assessment of Double-Inlet Collector in Solar Chimney Power Plant Systems, ASME Fluids Engineering Division Summer Meeting (FEDSM), Aug. 2017, .
- N. Fathi, P. McDaniel, S.S. Aleyasin, M. Robinson, P. Vorobieff, S. Rodriguez, C. de Oliveira,” Novel Integrated Solar-Nuclear Combined Cycle Power Plant”, Journal of Cleaner Production, Elsevier, Accepted, 2017.
- N. Fathi, P. McDaniel, C. Forsberg, C. de Oliveira, “ Power Cycle Assessment of Nuclear Systems, Providing Energy Storage for Low Carbon Grids,” Journal of Nuclear Engineering and Radiation Science, Accepted, 2016.

- N. Fathi, P. McDaniel, C. Forsberg and C. de Oliveira, “Nuclear Systems for a Low Carbon Electrical Grid.” ASME ICONE24, Jun. 2016.
- N. Fathi, S. S. Aleyasin, P. Vorobieff, “Numerical-Analytical Assessment on Manzanares Prototype” Journal of Applied Thermal Engineering (2017).
- Putkaradze, Vakhtang, Peter Vorobieff, Andrea Mammoli, and Nima Fathi. ”Inflatable free-standing flexible solar towers,” Solar Energy 98 (2013): 85-98.

A.2 Patents

- ”Annular Flow Convection Chimney (AFCC), Multi Inlet Solar Thermal Array Collector-Tower”, Nima Fathi, Peter Voroerr, Seyed Sobhan Aleyasin, Andrea Mammoli, application filed with STC at UNM, STC Ref. No. 2016-031-01)
- “ Inflatable, Free-Standing Solar Updraft Tower with Optimal Geometry and Active Control” , Peter Vorobieff, Vakhtang Putkaradze, Nima Fathi, Seyed Sobhan Aleyasin, Andrea Mammoli, Michael Chi, Francois Gay-Balmaz, application filed with STC at UNM, Track Code: 2015-021.

A.3 Presentations

- N. Fathi, P. Wayne, I. Monje, P. Vorobieff, “Experimental validation of a solar-chimney power plant model”, American Physical Society Division of Fluid Dynamics, Portland, Oregon, Nov. 2016.

-
- N. Fathi, P. McDaniel, C. Forsberg, C. de Oliveira, “Nuclear Systems for a Low Carbon Electrical Grid.” ASME ICONE24, Jun. 2016.
 - P. Vorobieff, A. Mammoli, N. Fathi, V. Putkaradze , “Free-standing inflatable solar chimney: experiment and theory,” American Physical Society Division of Fluid Dynamics, San Francisco, CA, 2014.
 - N.Fathi, P.Vorobieff, Seyed Sobhan Aleyasin, “VV Exercise for a Solar Tower Power Plant,” ASME Verification and Validation Symposium, Las Vegas, NV, 2014.
 - P. Vorobieff, V. Putkaradze, A. Mammol, N. Fathi, “Optimal design of an inflatable, free-standing solar updraft tower,” Wester Section of American Mathematical Society (AMS), Boulder, CO, 2013.

Appendix B

Experimental Analysis of Inflatable Tower

The aim of this investigation is to verify and validate the modeling of fluid mechanics and heat transfer processes in a solar chimney power plant. The modeling uses a finite volume method applied to simulate the fluid flow and solve Navier-Stokes equations for the two-dimensional models of the plant. The representative size of the plant can be very large, and turbulence must be accounted for. Several turbulence models were applied in the model. The upstream velocity and power generated by the power plant system was calculated from the CFD results and compared with experimental results and available theory. Code sensitivity to different parameters of the flow was investigated. Power prediction from the model appears to be keenly sensitive to the pressure boundary conditions, suggesting

that some choices of the boundaries of the computational domain may lead to unreliable results.

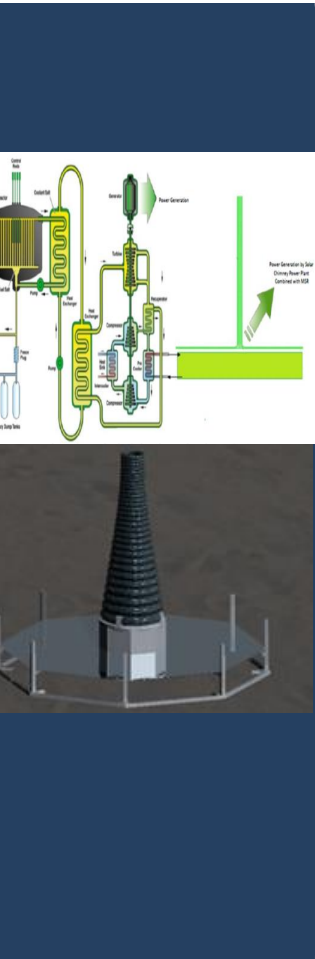
<https://cstools.asme.org/csconnect/FileUpload.cfm?View=yes&ID=44167>

ASME V&V 2014-7111



V&V Exercise for a Solar Tower Power Plant

Nima Fathi, Peter Vorobieff and Seyed Sobhan Aleyasin





Outline

- Motivation
 - Background
 - Numerical Analysis-I
 - Experimental Set-up
 - Numerical Analysis-II
 - Innovations
 - Conclusion
-

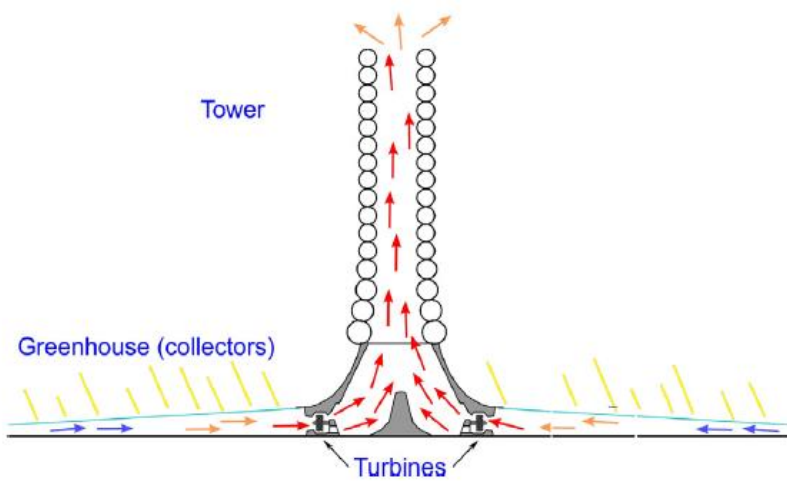


Motivation

- How can we generate electricity from the natural convection effect?
 - Alternate sustainable energy pathway from solar radiation to electrical available for night operation.
 - Are we able to combine our cycle?
-



Solar Tower Power Plant





Background

- Spanish colonel proposed this idea(1903).
 - The most famous prototype built in Manzanares at Spain in 1982 and rebuilt in 1989.
 - China recently started to invest on this industry.
-



Numerical Analysis-I

Turbulent
Flow

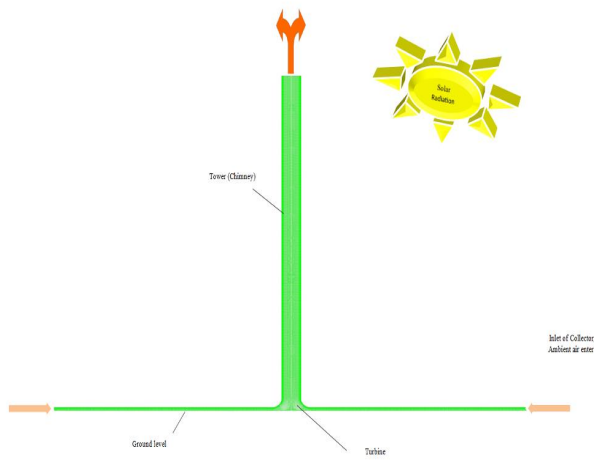
Air

Natural
Convection



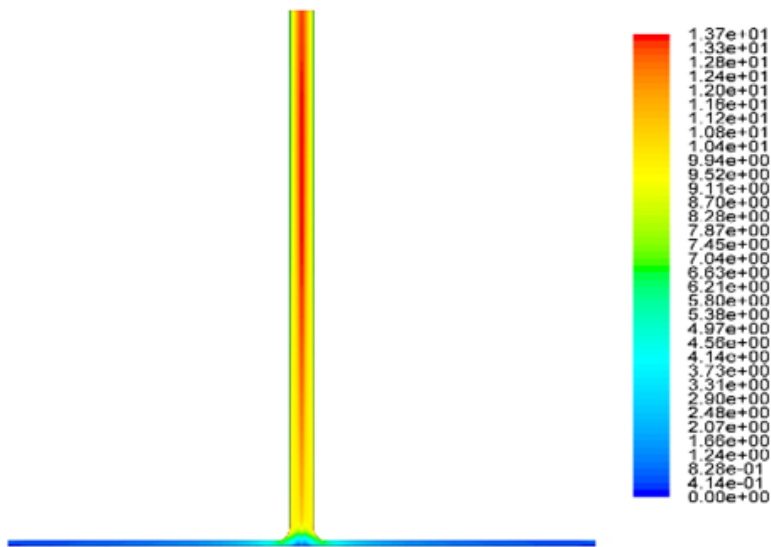
Numerical Analysis-I

Manzanares Simulation





Numerical Analysis-I





Numerical Analysis-I

Verification

- Mesh Independency
 - Iterative Convergence
 - Consistency: 0.001 mass flow rate
 - Boundary Condition Sensitivity
 - Density Sensitivity Analysis
 - Second Order of Discretization
-



Numerical Analysis-I

Calibration of pressure boundary
condition

Calibration of collector boundary
condition



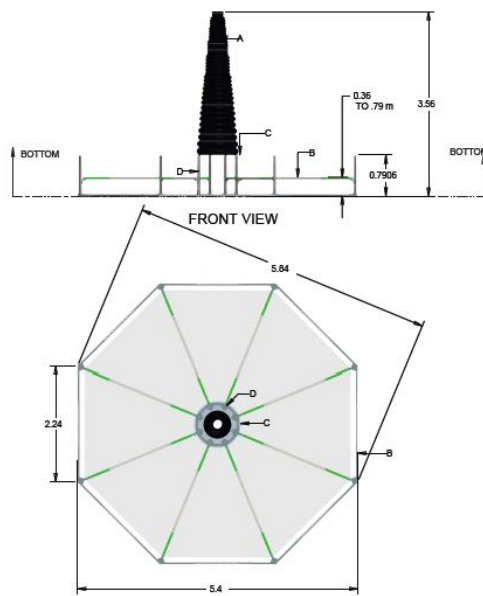
Numerical Analysis-I

Validation

- Updraft Vel. of experimental set up: 10-12 m/s
 - Updraft Vel. of numerical analysis: 11.56 m/s
-



Experimental Setup





Experimental Setup





Experimental Setup





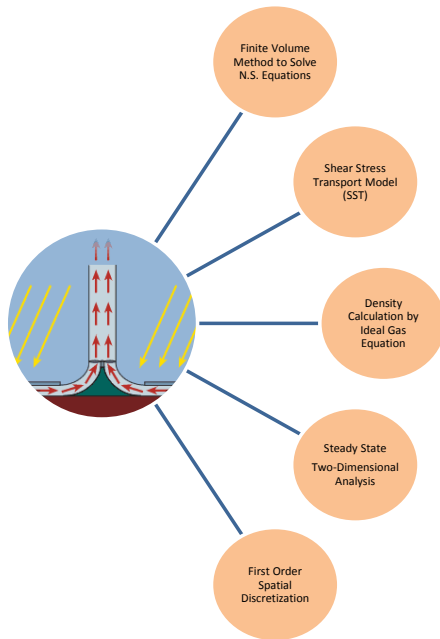
Experimental Setup





Numerical Analysis-II

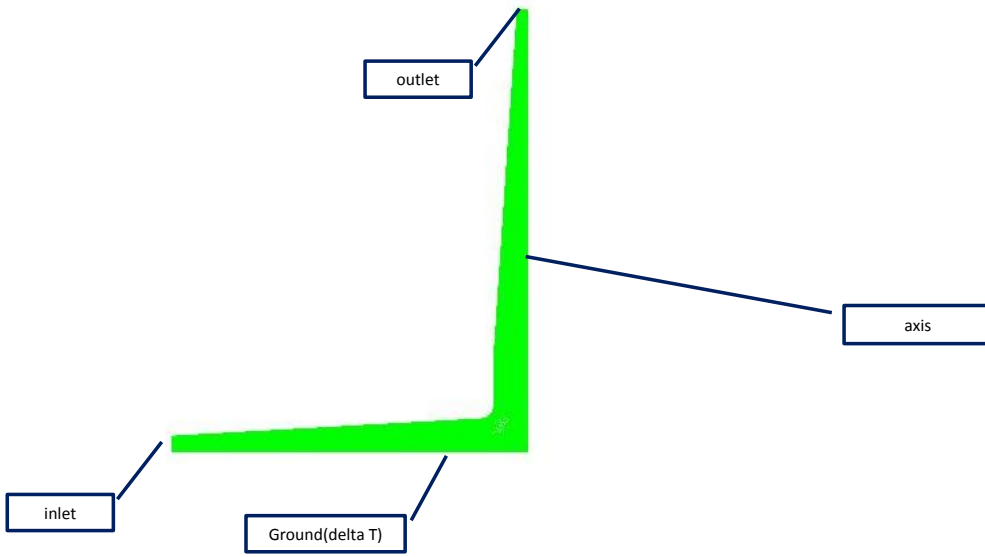
CFD Analysis of Solar Chimney Power Plant Prototype





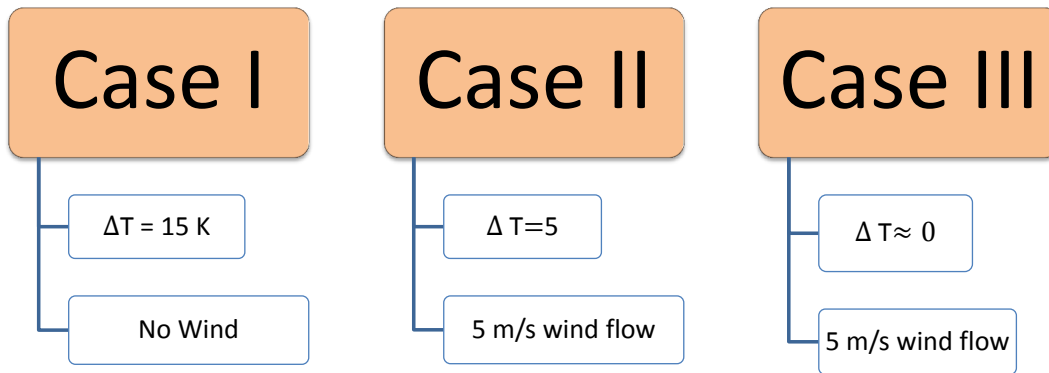
CFD Analysis of Solar Chimney Power Plant Prototype

- Detail of Boundary Conditions, 53k nodes.





CFD Analysis of Solar Chimney Power Plant Prototype

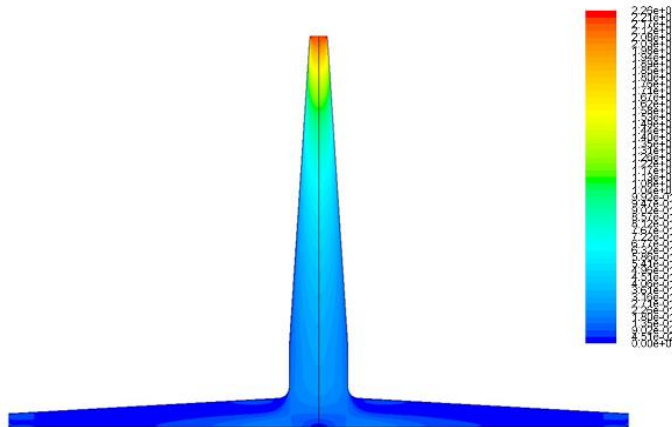




CFD Analysis of Solar Chimney Power Plant Prototype

- Case I

Velocity contour plot, Unit is m/s, mass flow rate= 0.0521 kg/sec, Buoyancy effect is dominant.

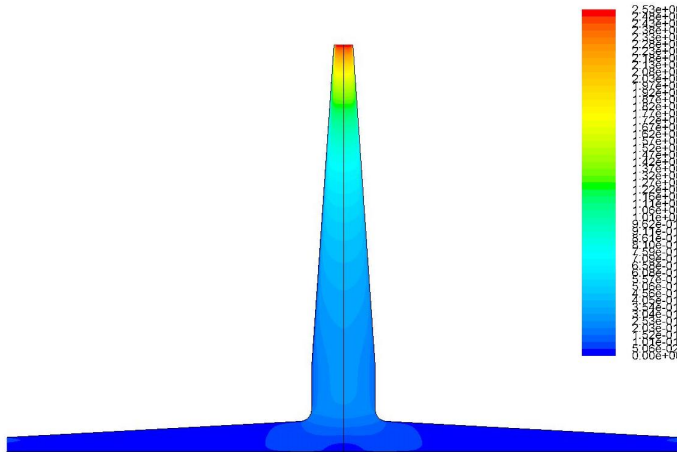




CFD Analysis of Solar Chimney Power Plant Prototype

- Case II

Velocity contour plot, Unit is m/s, mass flow rate= 0.0559 kg/sec, Dynamic pressure is dominant.

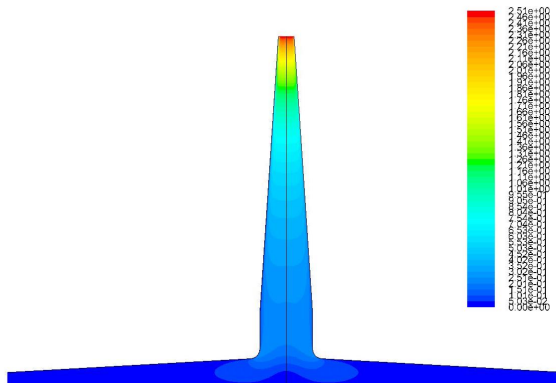




CFD Analysis of Solar Chimney Power Plant Prototype

- Case III

Velocity contour plot, Unit is m/s, mass flow rate= 0.0557 kg/sec.

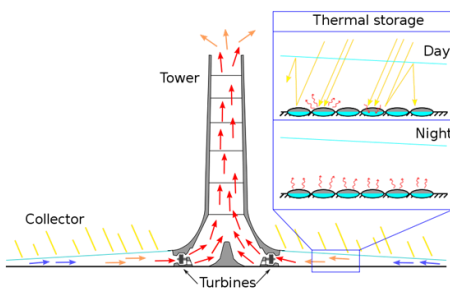




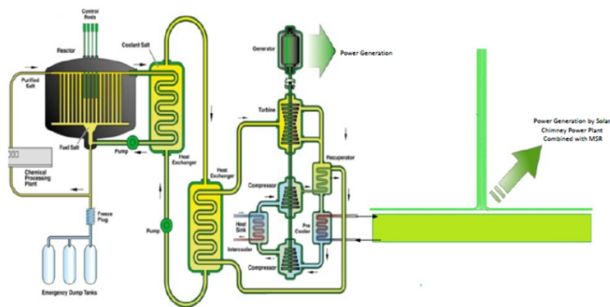
Validation

- 4-5 m/s wind, probe shows: 2.5 m/s
 - 5 m/s wind, at the same position : 2.3 m/s
-

Innovations



Schematic of Basic Solar Tower (chimney). They are only 1 to 5% efficient. With various modifications, they can be upgraded to about 35% efficiency.



Molten Salt Reactor with Advanced Solar Tower. The cooling tower is replaced with an advanced solar tower. The idea can be used in any nuclear reactor as well as coal plant.



Innovations

- What differentiates our approach (two patents).
 - *Optimize solar chimney with new enhancements for higher energy efficiency:*
 - Optimal design of sloping collectors and divergent towers.
 - Convergent-divergent shape to increase energy production by about 15%.
 - Performance gains from a flow-directing hub on the ground.
 - Higher harvestable kinetic energy at the turbine.
 - Double tray collector.
 - *Adapt the advanced solar chimney onto a power plant for more efficient energy :*
 - The above modifications can be incorporated into an optimized solar chimney, which is then interfaced onto a power plant, such as nuclear and coal.
 - Instead of releasing the waste heat through a cooling tower, the heat is transformed from buoyant to kinetic energy that drives the turbines, thereby significantly increasing the overall power plant efficiency.
-



Conclusion

- For BC, it is better to use temperature difference for the ground.
 - Code calibration plays an important role for SCPP.
 - It is better to validate the calibrated code with another experimental model too.
 - Wind situation should be considered in CFD to be closer to the reality.
-



References

- “Use of waste heat to enhance solar chimney power plant(SCPP) performance (Combined Solar Cycles)”, Nima Fathi, Peter Vorobieff, Seyed Sobhan Aleyasin, Patrick McDaniel, Salvador Rodriguez, non-disclosure application filed with USPTO, Application No. 14/695046.
 - Vorobieff, Peter, Andrea Mammoli, Nima Fathi, and Vakhtang Putkaradze. "Free-standing inflatable solar chimney: experiment and theory." *Bulletin of the American Physical Society* 59 (2014).
 - Putkaradze, Vakhtang, Peter Vorobieff, Andrea Mammoli, and Nima Fathi. "Inflatable free-standing flexible solar towers." *Solar Energy* 98 (2013): 85-98.
-